

Luminescent Nanomaterials

Guest Editors: Le Quoc Minh, Wieslaw Strek,
Tran Kim Anh, and Kui Yu





Luminescent Nanomaterials

Journal of Nanomaterials

Luminescent Nanomaterials

Guest Editors: Le Quoc Minh, Wieslaw Strek,
Tran Kim Anh, and Kui Yu



Copyright © 2007 Hindawi Publishing Corporation. All rights reserved.

This is a special issue published in volume 2007 of “Journal of Nanomaterials.” All articles are open access articles distributed under the Creative Commons Attribution License, which permits unrestricted use, distribution, and reproduction in any medium, provided the original work is properly cited.

Editor-in-Chief

Michael Z. Hu, Oak Ridge National Laboratory, USA

Advisory Board

James Adair, USA
C. Brinker, USA
Taeghwan Hyeon, South Korea

Nathan Lewis, USA
Alon McCormick, USA
Gary Messing, USA

Z. L. Wang, USA
Alan Weimer, USA
Jackie Ying, USA

Associate Editors

John Bartlett, Australia
Michael Harris, USA
Do Kyung Kim, South Korea

S. J. Liao, China
Jun Liu, USA
S. Mathur, Germany

Michael S. Wong, USA
M. Yoshimura, Japan

Editorial Board

Donald A. Bansleben, USA
C. Brosseau, France
Siu Wai Chan, USA
G. Chen, USA
Sang-Hee Cho, South Korea
C. Cui, China
Ali Eftekhari, Iran
Claude Estournes, France
Alan Fuchs, USA
Lian Gao, China
Hongchen Gu, China
Justin Holmes, Ireland

David Hui, USA
Rakesh K. Joshi, USA
Li Jun, Singapore
Alan Lau, Hong Kong
B. I. Lee, USA
J. -Y. Liu, USA
Songwei Lu, USA
Ed Ma, USA
P. Panine, France
Donglu Shi, USA
Bohua Sun, South Africa
Xiaogong Wang, China

E. G. Wang, China
Y. Wang, USA
C. P. Wong, USA
Ping Xiao, UK
Zhili Xiao, USA
N. Xu, China
Doron Yadlovker, Israel
Peidong Yang, USA
Zhenzhong Yang, China
Kui Yu, Canada

Contents

Luminescent Nanomaterials, Le Quoc Minh, Wieslaw Streck, Tran Kim Anh, and Kui Yu
Volume 2007, Article ID 48312, 1 page

Luminescence, Energy Transfer, and Upconversion Mechanisms of Y_2O_3 Nanomaterials Doped with Eu^{3+} , Tb^{3+} , Tm^{3+} , Er^{3+} , and Yb^{3+} Ions, TranKim Anh, Paul Benalloul, Charles Barthou, Lam thiKieu Giang, Nguyen Vu, and LeQuoc Minh
Volume 2007, Article ID 48247, 10 pages

Rare-Earth Doped Nanocrystalline Phosphors for Field Emission Displays, P. Psuja, D. Hreniak, and W. Streck
Volume 2007, Article ID 81350, 7 pages

Multifunctional Composites Obtained by Incorporating Nanocrystals into Decorated PVK Polymers, Haizhu Sun, Junhu Zhang, Ye Tian, Yang Ning, Hao Zhang, Jie Ju, Delong Li, Shidong Xiang, and Bai Yang
Volume 2007, Article ID 38589, 7 pages

Rare Earth-Activated Silica-Based Nanocomposites, C. Armellini, A. Chiappini, A. Chiasera, M. Ferrari, Y. Jestin, M. Mortier, E. Moser, R. Retoux, and G. C. Righini
Volume 2007, Article ID 84745, 6 pages

Sol-Gel Processing of Nanostructured Inorganic Scintillating Materials, J. M. Nedelec
Volume 2007, Article ID 36392, 8 pages

Photoluminescence of Silicon Nanocrystals in Silicon Oxide, L. Ferraioli, M. Wang, G. Pucker, D. Navarro-Urrios, N. Daldosso, C. Kompocholis, and L. Pavesi
Volume 2007, Article ID 43491, 5 pages

Morphology and Luminescence of Nanocrystalline Nb_2O_5 Doped with Eu^{3+} , Daniele Falcomer, Adolfo Speghini, Giulio Ibba, Stefano Enzo, Carla Cannas, Anna Musinu, and Marco Bettinelli
Volume 2007, Article ID 94975, 5 pages

Upconversion Properties of Nanocrystalline $ZrO_2:Yb^{13+}$, Er^{3+} Phosphors, Iko Hyppänen, Jorma Hölsä, Jouko Kankare, Mika Lastusaari, and Laura Pihlgren
Volume 2007, Article ID 16391, 8 pages

Femtosecond Transient Absorption Studies in Cadmium Selenide Nanocrystal Thin Films Prepared by Chemical Bath Deposition Method, M. C. Rath, J. A. Mondal, D. K. Palit, T. Mukherjee, and H. N. Ghosh
Volume 2007, Article ID 36271, 7 pages

Editorial

Luminescent Nanomaterials

Le Quoc Minh,¹ Wieslaw Streck,² Tran Kim Anh,¹ and Kui Yu³

¹ *Institute of Materials Science, Vietnam Academy of Science and Technology, 18 Hoang Quoc Viet Road, Hanoi, Vietnam*

² *Institute of Low Temperature and Structure Research, Polish Academy of Science, Okólna 2, 50-422 Wrocław, Poland*

³ *Steacie Institute for Molecular Sciences, National Research Council Canada, Ottawa, ON, Canada K1A 0R6*

Received 31 December 2007; Accepted 31 December 2007

Copyright © 2007 Le Quoc Minh et al. This is an open access article distributed under the Creative Commons Attribution License, which permits unrestricted use, distribution, and reproduction in any medium, provided the original work is properly cited.

Luminescent Nanomaterials, a newly emerging field at the frontier of science, provide challenges to both fundamental research and breakthrough development of technologies in various areas such as electronics, photonics, nanotechnology, display, lasing, detection, optical amplification, fluorescent sensing to biomedical engineering, and environmental control. Luminescent nanomaterials come in many forms such as nanoclusters, quantum dots, tubes, wires, cages, balls, and nanostructured units. They can be made up of rare earth elements, semiconductors, metals, oxides, and inorganic and organic polymers; however, the investigation on the synthesis-structure-property relationship is still in infant stages. In general, luminescent nanomaterials have unique properties which greatly differ from those of microscale and bulk materials.

The aim of this special issue on “Luminescent Nanomaterials” is to bring to readers up-to-date advances in the fundamental understanding of the luminescent mechanism related to nanosizes and nanostructures, up-conversion effect, energy transfer for enhanced emission, transient spectroscopy on a femtosecond time scale of silver plasmon. Furthermore, this special issue aims at stimulating apply-oriented research in the technologies above mentioned. Therefore, this special issue, covering a broad range of topics on luminescent nanomaterials, should be of interest to its readership.

Finally, we would like to acknowledge those who assisted the editing of this issue, including our authors, reviewers, the staff of Hindawi Publisher, and Dr. Michael Z. Hu Editor-in-Chief of Journal of Nanomaterials. Professor Minh, Head of guest editors, wants to thank each guest editor for the achievement of this special issue on “Luminescent Nanomaterials”.

*Le Quoc Minh
Wieslaw Streck
Tran Kim Anh
Kui Yu*

Research Article

Luminescence, Energy Transfer, and Upconversion Mechanisms of Y_2O_3 Nanomaterials Doped with Eu^{3+} , Tb^{3+} , Tm^{3+} , Er^{3+} , and Yb^{3+} Ions

TranKim Anh,¹ Paul Benalloul,² Charles Barthou,² Lam thiKieu Giang,¹ Nguyen Vu,¹ and LeQuoc Minh^{1,3}

¹Institute of Materials Science, Vietnamese Academy of Science and Technology, 18 Hoang Quoc Viet Road, Cau Giay, Hanoi, Vietnam

²Institute des Nanosciences de Paris (INSP), UMR-CNRS 7588, Universites Pierre et Marie Curie et Denis Diderot, 140 Rue de Lourmel, Paris 75015, France

³College of Technology, Vietnam National University, 144 Xuan Thuy Street, Cau Giay District, Hanoi, Vietnam

Received 21 May 2007; Revised 16 December 2007; Accepted 31 December 2007

Recommended by Wieslaw Streck

Luminescence, energy transfer, and upconversion mechanisms of nanophosphors ($Y_2O_3:Eu^{3+}$, Tb^{3+} , $Y_2O_3:Tm^{3+}$, $Y_2O_3:Er^{3+}$, Yb^{3+}) both in particle and colloidal forms were studied. The structure, phase, and morphology of the nanopowders and nanocolloidal media were determined by high-resolution TEM and X-ray diffraction. It was shown that the obtained nanoparticles have a round-spherical shape with average size in the range of 4 to 20 nm. Energy transfer was observed for $Y_2O_3:Eu^{3+}$, Tb^{3+} colloidal and powders, upconversion transitions were observed for both $Y_2O_3:Er^{3+}$ and $Y_2O_3:Er^{3+}$, Yb^{3+} nanophosphors. The dependence of photoluminescence (PL) spectra and decay times on doping concentration has been investigated. The infrared to visible conversion of emission in $Y_2O_3:Er^{3+}$, Yb^{3+} system was analyzed and discussed aiming to be applied in the photonic technology.

Copyright © 2007 TranKim Anh et al. This is an open access article distributed under the Creative Commons Attribution License, which permits unrestricted use, distribution, and reproduction in any medium, provided the original work is properly cited.

1. INTRODUCTION

Luminescent nanomaterials in the form of nanoparticles, nanorods, nanowires, nanotubes, as well as colloidal or bulk nanocrystals are of interest not only for basic research, but also for interesting application [1–3]. High surface to volume ratio, local phenomena such as absorption or change in the surface electronic state may contribute significantly to special properties. An understanding of luminescent properties, energy transfer (ET), and upconversion could determine how to tailor nanophores for a given application. Nanomaterials have potential application as efficient display phosphors, such as in new flat panel displays with low-energy excitation source [2, 3]. $Y_2O_3:Eu^{3+}$ phosphor, one of the most promising oxides-based red phosphors, was studied for a long time because of its efficient luminescence under ultraviolet (UV) and cathode-ray excitation. $Y_2O_3:Eu^{3+}$ with micrometer size grains was used as the red component in three chromatic lamps and projection color television [4–6]. Numerous studies were focused on synthesis and optical properties of nanosized $Y_2O_3:Eu^{3+}$ phosphors [7–10]. Size-dependence efficiency in $Y_2O_3:Tb^{3+}$ [11] and effect of grain

size on wavelength of $Y_2O_3:Eu^{3+}$ [12] were investigated. Different methods were used to prepare $Y_2O_3:RE^{3+}$ nanocrystals [13–19] such as chemical vapor synthesis [15], combustion [16, 17], sol-gel [18], and aerosol pyrolysis [19]. Relationship between optical properties and crystalline of nanometer $Y_2O_3:Eu^{3+}$ phosphor has been investigated [20]. The new method of polyol-mediated synthesis of nanoscale materials was presented [21, 22] and the luminescence properties of nanocrystalline $Y_2O_3:Eu^{3+}$ were investigated [23]. Anh et al. studied the ET between Tb^{3+} and Eu^{3+} in Y_2O_3 microcrystals [4]. The role of the active center concentrations in the ET of lanthanide ions was investigated not only for $Y_2O_3:Tb^{3+}$, Eu^{3+} , but also for organic compound glutamic acid as well as LnP_5O_{14} laser crystals [24]. ET and relaxation processes in $Y_2O_3:Eu^{3+}$ were studied [25]. Preparation and optical spectra of trivalent rare earth ions doped cubic Y_2O_3 nanocrystal have received our considerable attention over 10 years [10, 16, 26–33]. Not only the $Eu^{3+}-Tb^{3+}$ couple, but also the $Er^{3+}-Yb^{3+}$ one are attractive for application in visible emission by ET and upconversion processes. Among emission properties of Y_2O_3 doped with rare earth ions, upconversion is the most attractive phenomenon not only from

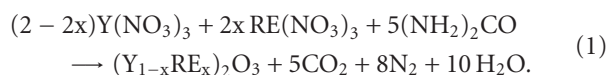
photophysical mechanism, but also for application. The enhancement of the red emission via upconversion in bulk and nanocrystalline cubic $Y_2O_3:Er^{3+}$ has been studied [34]. Red, green, and blue upconversion luminescences of trivalent rare earth ion doped Y_2O_3 nanocrystals were investigated [35]. Effect of Yb^{3+} codoping on the upconversion luminescence properties of $Y_2O_3:Yb^{3+}, Er^{3+}$ nanocrystallines and nanostructures have been studied [36–38]. The absorption and emission spectroscopy of $Er^{3+}-Yb^{3+}$ doped aluminum oxide waveguides were reported [39].

The oxide lattice has proved to be an excellent host material for some of the most powerful laser built. Among them, Y_2O_3 is characterized by low-phonon frequencies which make inefficient nonradiative relaxation of the excited states. The Y_2O_3 host was chosen due to its high refractory properties with a melting point of about $2450^\circ C$, a very high thermal conductivity of $33 W m^{-1} K^{-1}$, and a density of $5.03 g cm^3$. Y_2O_3 is a suitable material for photonic waveguide due to its high-energy band gap of 5.8 eV, a high refractive index about 2, and a wide transmission region from 280 nm to 8 micrometer. Eu^{3+} exhibits an atomic-like transition in red region at 612 nm. Er^{3+} emissions lie in infrared around 1530 nm as well as upconversion in visible ranges of green and red. The blue emission of Tm^{3+} ions is one of the three important basic colors of display. However, up to now, few articles were devoted to Y_2O_3 doped with Tm^{3+} and codoped with Tb^{3+}, Eu^{3+} or Yb^{3+}, Er^{3+} in both the nanopowder or nanocolloidal forms.

In this work, we report on new synthesis of Y_2O_3 nanophosphor in the two forms of powders and colloidal doped with $Tb^{3+}, Eu^{3+}, Tm^{3+}, Er^{3+}$, and Yb^{3+} . The concentration dependence and the influence of size on the luminescent properties will be discussed. The investigation of ET between Tb^{3+} and Eu^{3+} , and the mechanism of upconversion in $Y_2O_3:Er^{3+}, Yb^{3+}$ nanosize are of the main points.

2. EXPERIMENT

The powder nanophosphors $Y_2O_3:Eu^{3+}$ (1–10 mol%), $Y_2O_3:Er^{3+}$ (1–15 mol%) and $Y_2O_3:Er^{3+}$ (1 mol%), Yb^{3+} (5%), and $Y_2O_3:Tm^{3+}$ (1–4 mol%) were prepared by combustion reaction. Europium oxide (99.995%, CERAC), Yttrium oxide (99.999%, ALFA), and nitric acid and urea (99%, SIGMA-ALDRICH) were used as starting raw materials to prepare $Y_2O_3:Eu^{3+}$. $Y(NO_3)_3$ and $RE(NO_3)_3$ stock solutions were prepared by dissolving Y_2O_3, Er_2O_3, Yb_2O_3 , and Eu_2O_3 in nitric acid and diluting with deionized water. The synthesis reaction is [28]



Nanocolloidal samples of $Y_2O_3, Y_2O_3:Eu^{3+}, Tb^{3+}, Y_2O_3:Tm^{3+}$ with different Eu^{3+} concentrations of 1, 3, 5, 7, and 10 mol%, Tb^{3+} concentration of 1.25 mol%, and Tm^{3+} concentrations of 1–4 mol% were prepared by a direct precipitation route from high-boiling polyol solution [22]. The starting materials were $YCl_3, EuCl_3, TbCl_3, TmCl_3, NaOH$, and diethylene glycol (DEG) with high purity grade.

The samples were checked by the X-ray diffractometer (D5000, Siemens). The morphology and particle sizes of $Y_2O_3:RE^{3+}$ were observed by transmission electron microscopy (TEM, H7600, Hitachi), high-resolution transmission electron microscopy HRTEM Philips CM200, 160 KV, and FE-SEM (S4800, Hitachi). Photoluminescent measurements were performed using a Jobin Yvon HR 460 monochromator and a multichannel CCD detector from instruments SA model Spectraview-2D for the visible and near infrared range and a Triax 320 with a PDA multichannel 256 pixels detector for the IR range. The decay time was analyzed by a PM Hamamatsu R928 and Nicolet 490 scope with a time constant of the order of 7 nanoseconds. Kimmon He-Cd laser (325 nm excitation), Nitrogen laser (337.1 nm), and Diode laser or Ti-Sapphire laser were used as the excitation sources.

3. RESULTS AND DISCUSSION

3.1. Morphology and structure of nanopowders and nanocolloidal media

Figure 1 shows TEM and HRTEM images of Y_2O_3 nanocolloidal and electron diffraction of Y_2O_3 nanoparticles. One can notice that our samples are spherical shaped, small sized (5 nm), and with narrow distribution.

The synthesis of useful amounts of sub 5 nm size lanthanide-doped oxides remains a challenge in optical material research. A few weeks ago, stable colloidal was prepared and has been reported in [22]. For the first time, nanocolloidal codoped Tb^{3+} and Eu^{3+} and oxide particle suspension were prepared in our laboratory. The transparent suspensions of particles dispersed in organic solvent were obtained with high stability for a year. The absorption spectra of the colloids have been characterized with a strong and broad band for $Y_2O_3, Y_2O_3:Eu^{3+}, Y_2O_3:Tb^{3+}, Y_2O_3:Tm^{3+}, Y_2O_3:Eu^{3+}, Tb^{3+}$ nanoparticles in the long range from 230 nm to 380 nm with the maxima around 240–250 nm.

X-ray diffraction of $Y_2O_3:RE^{3+}$ samples annealed at different temperatures was studied. The pure polycrystalline Y_2O_3 was used as standard sample for the correction of the instrumental line broadening. The profiles of diffracting peaks were fitted to the ps-voigt1 function. The grain sizes and size distribution have been determined by the WIN-CRYSIZE program packet [40]. The column length distribution can be obtained from double differentiation of the Fourier transform of the line profile [41]. According to this method, the reflection intensity of the given set of lattice planes is expressed in terms of a sum of the intensities from all columns of lattice cells perpendicular to the planes [42, 43].

Figure 2 exhibits X-ray diffraction (XRD) patterns of $Y_2O_3:Eu^{3+}$ (5%) annealed at 500, 550, 600, 700, and $900^\circ C$. The powder annealed at $500^\circ C$ is amorphous. The Y_2O_3 cubic phase appears when annealed above $550^\circ C$.

The main diffraction peaks, in agreement with the JCPDS 41-1105 reference, correspond to the [222], [400], [440], and [622] planes. However, the widths of the diffraction lines are

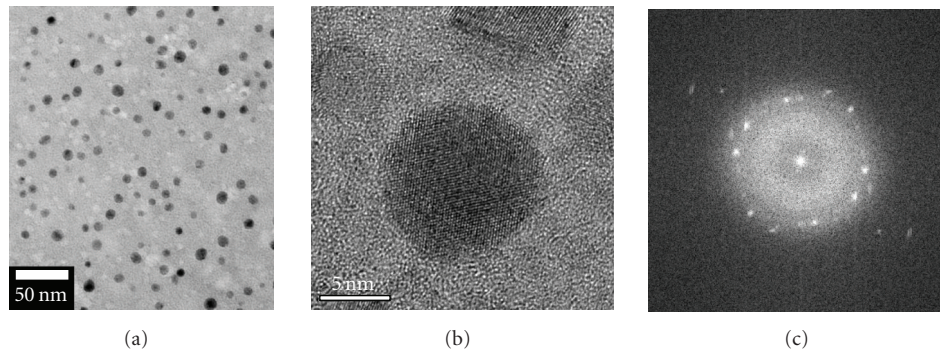


FIGURE 1: (a) TEM, (b) HRTEM images of Y_2O_3 nanocolloidal, and (c) the corresponding electron diffraction pattern of Y_2O_3 nanoparticles.

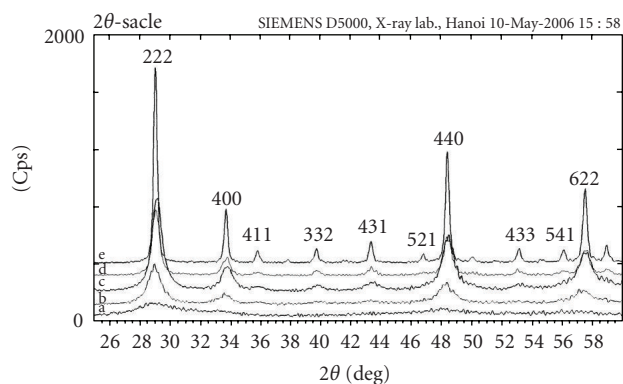


FIGURE 2: (a) XRD diffraction pattern of $Y_2O_3:Eu^{3+}$ (5 mol%) powders annealed at 500°C, (b) 550°C, (c) 600°C, (d) 700°C, and (e) 900°C.

broadened because of the small size of the crystallites. Then they get narrower and narrower at higher temperatures. This process reflects the fact that the crystalline size is increasing with temperature of annealing process. The peak profiles of [222] reflection (in Figure 2, at $2\theta = 29.150$) were used for starting data of Warren-Averbach method [41]. This method was used to study nanocrystalline gold [42]. It was noted that the results of the average column length usually differ from crystallite sizes evaluated from Scherer equation [43]. The main reason is due to the Warren-Averbach method which provides a volumetric average of the crystallite size. We can see that the size distributions for small grains <10 nm have asymmetrical shape with small FWHM (of the size distribution), while for bigger grains they become more symmetrical and their FWHM are larger. The size distribution of $Y_2O_3:Eu^{3+}$ (5%) versus annealing temperature and time calculated by Warren-Averbach method is presented in Table 1 and Figure 3.

The XRD of $Y_2O_3:Er^{3+}$ 10 mol% nanomaterials (annealed at 600°C for 30 minutes) also shows a cubic symmetry like the Y_2O_3 reference powder. The FWHM of the diffraction lines for nanomaterials is larger than that of the Y_2O_3 crystals. The sizes are about 7 nm and 23.4 nm, respectively, the FWHM of the size distribution for the nanopowder is 11 nm and 20.1 nm for the sample annealed at 600°C for 30

TABLE 1: Size and FWHM of $Y_2O_3:Eu^{3+}$ particles versus annealing temperature and time.

T (°C)	Time (min)	d (nm)	FWHM (nm)
550	60	4.4	7.3
600	30	5.6	6.9
700	30	15.2	9.3
900	30	46.1	20.6
900	60	72.2	22.6

minutes and at 800°C for 30 minutes, respectively. These data were also calculated by using the Warren-Averbach method. For the $Y_2O_3:Tm^{3+}$ nanophores, the mean sizes of the particle are 7.2, 7.4, and 7.7 nm, respectively, with Tm^{3+} concentrations of 0.1, 1, and 4 mol%.

3.2. Luminescent spectra

Size-dependent efficiency was reported in Tb-doped Y_2O_3 nanocrystalline phosphor [11]. In $Y_2O_3:Tb^{3+}$ nanocrystalline, the efficiency varied as the square of the particle size ranged from 100 to 40 Å. It could be nonradiative contributions decrease with the decrease in particle size. On the other hand, effects of grain size from 43 nm to 71 nm on wavelength of $Y_2O_3:Eu^{3+}$ emission spectra are investigated in detail [12]. The blue shift effect of emission was observed very small in $Y_2O_3:Eu^{3+}$ nanophosphor. In contrast, we could not find any blue shift change in the luminescent spectra of $Y_2O_3:Eu^{3+}$ prepared by combustion reaction.

The photoluminescent (PL) spectra of $Y_2O_3:Tb^{3+}$ nanocolloidal correspond to the $^5D_4-^7F_J$ transitions according to the energy diagram and fluorescence processes of Tb^{3+} [5] (Figure 4(a)).

The PL spectra of $Y_2O_3:Eu^{3+}$ nanocolloidal with different concentrations (from 1 to 10 mol%) under 337.1 nm N_2 laser excitation show narrow emission peaks corresponding to the $^5D_0-^7F_J$ ($J = 0, 1, 2, 3, 4$) transitions of Eu^{3+} , with the most intense peak at 611 nm for the case of $J = 2$. Figure 4(b) presents the luminescent spectra of Y_2O_3 -doped 1, 3, 5, 7, and 10% Eu^{3+} nanocolloidal under 337.1 nm N_2 laser excitation. The PL spectra of $Y_2O_3:Eu^{3+}$ nanocolloidal also indicate

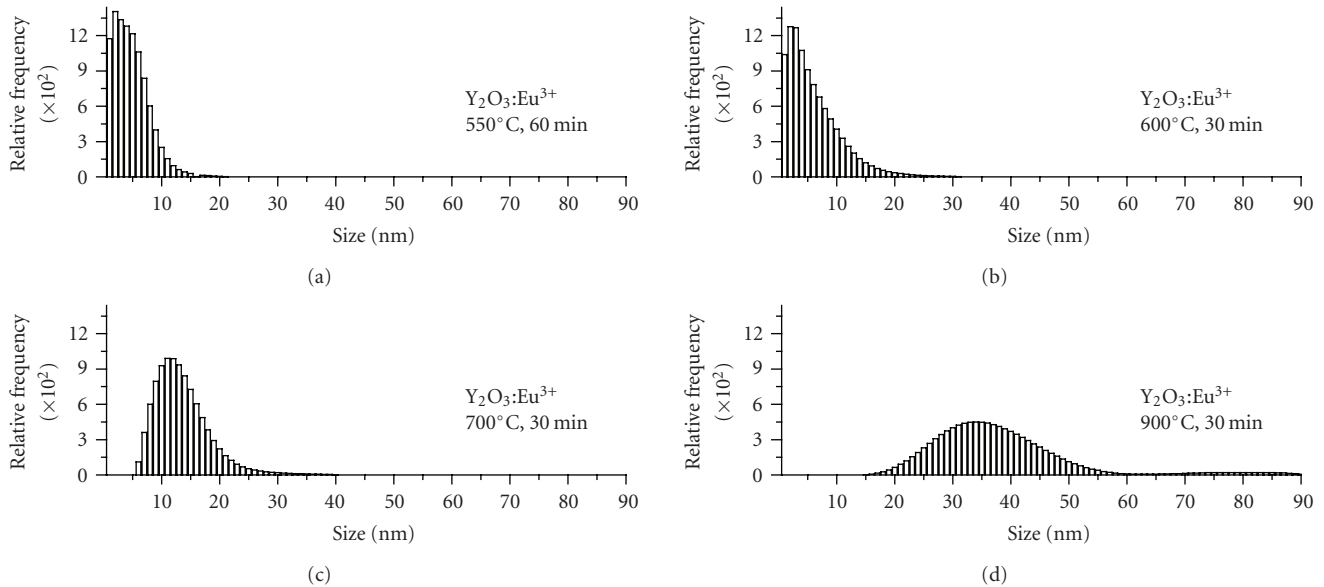


FIGURE 3: Size distribution calculated by W-A method of $\text{Y}_2\text{O}_3:\text{Eu}^{3+}$ (5%) powder annealed in 30 minutes at the temperatures of 550°C, 600°C, 700°C, and 900°C.

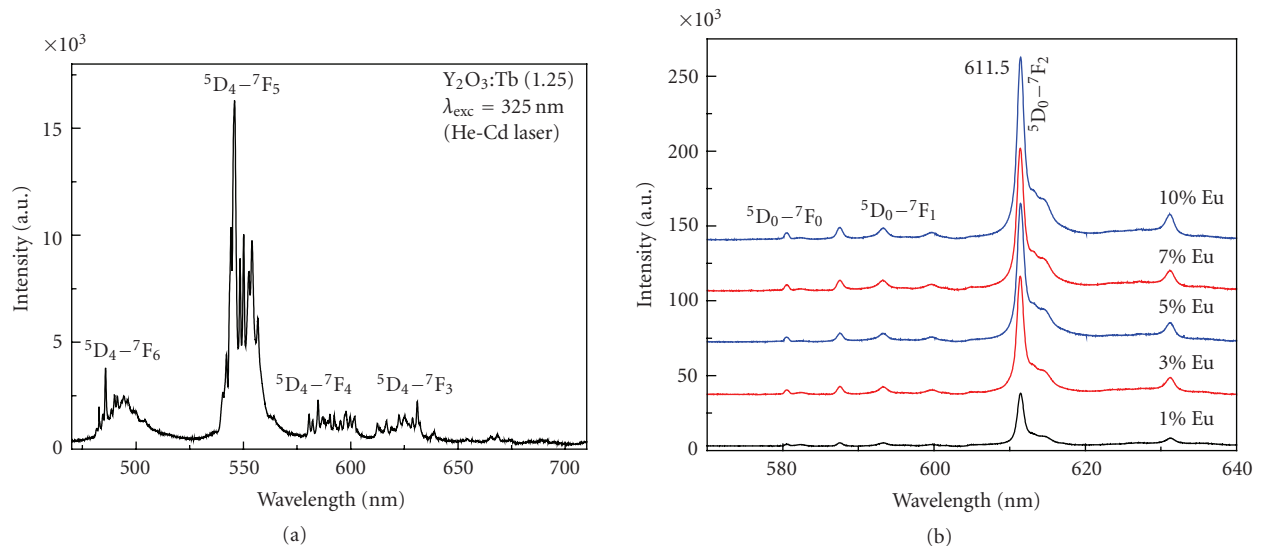


FIGURE 4: (a) Luminescent spectra of $\text{Y}_2\text{O}_3:\text{Tb}^{3+}$ nanoparticles excited at 325 nm, (b) luminescent spectra of Y_2O_3 doped 1% Eu, 3% Eu, 5% Eu, 7% Eu, and 10% Eu nanoparticles (from colloidal) excited by N_2 laser at 337.1 nm.

that not any quenching of the PL intensity for Eu^{3+} concentration up to 10 mol%. Y_2O_3 presents a cubic structure with lattice constant $a = 1.0604 \text{ \AA}$. The primitive unit cell contains 80 atoms (48 O and 32 Y), Y atoms occupy two sites with the C_2 and $S_6(C_{3i})$ symmetry site. Our samples of $\text{Y}_2\text{O}_3:\text{Eu}^{3+}$ nanopowder and nanocolloidal present a clearly dominant typical C_2 symmetry site.

For the $\text{Y}_2\text{O}_3:\text{Tm}^{3+}$ phosphor, luminescent intensity is stronger and synthesis temperature is lower in the case of nanocolloidal than in the powder's one. From excited luminescence spectra one can notice that optimal intensity was observed when excited by 362 nm. The luminescent spectra

of $\text{Y}_2\text{O}_3:\text{Tm}^{3+}$ nanopowder under 362 nm excited were presented in Figure 5.

The spectra of nanocolloidal and nanopowder under 337.1 nm excited are presented in the inset of Figure 5. The position is not different, but the spectral resolution in the nanocolloidal seems to be better in the powder.

The nanocolloids have a narrow size distribution and these spherical particles in the size range 5–10 nm are easy to mix with water or polymer solution. That can explain why the quenching concentration of Eu^{3+} , Tm^{3+} , and Er^{3+} has been raised remarkably. This nanocolloidal media is useful for preparing optical thin films.

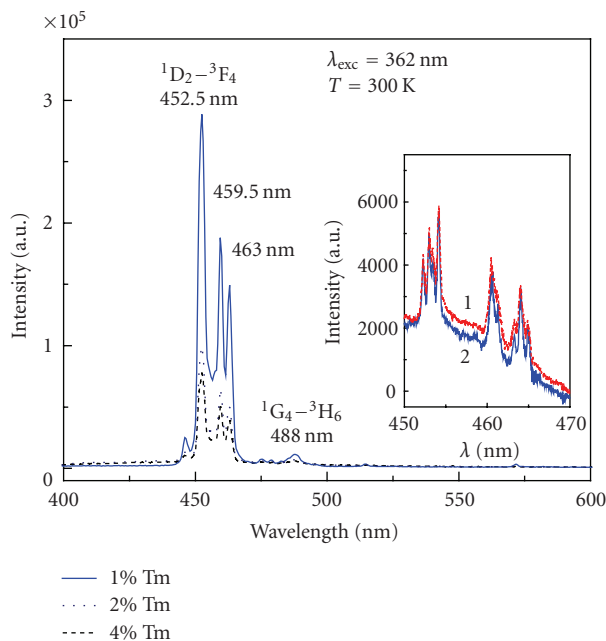


FIGURE 5: Luminescent spectra in dependence on Tm^{3+} concentration in $\text{Y}_2\text{O}_3:\text{Tm}^{3+}$ (1, 2, 4 mol%) nanopowder under 362 nm excitation. Inset: luminescent spectra of $\text{Y}_2\text{O}_3:\text{Tm}^{3+}$ nanocolloidal (1) and nanopowder (2) under 337.1 nm excitation.

3.3. Energy transfer and upconversion mechanisms

The role of concentration, temperature, solvents as well as upconversion, and ET mechanism were investigated in detail for Y_2O_3 nanophores containing Eu^{3+} , Tb^{3+} , Er^{3+} , and Yb^{3+} rare earth ions [34]. ET between Tb^{3+} and Eu^{3+} in nanopowder has been elucidated from the luminescent spectra of $(\text{Y}_{0.95}\text{Eu}_x\text{Tb}_y)_2\text{O}_3$ (with $x/y = 8/2, 9/1, 7/3$) by Anh et al. in our previous paper [28]. In $\text{Y}_2\text{O}_3:\text{Tb}^{3+}$, Eu^{3+} sample, the spectra exhibits the well-known ${}^5\text{D}_0-{}^7\text{F}_j$ line emissions ($J = 0, 1, 2, \dots$) of the Eu^{3+} ion with the strongest line for $J = 2$ at 612 nm in the red region. The peak at 546 nm assigned to the ${}^5\text{D}_4-{}^7\text{F}_5$ transition of Tb^{3+} ions is also observed. But the intensity of this peak is much lower than the peak corresponding to the ${}^5\text{D}_0-{}^7\text{F}_2$ transition of Eu^{3+} . The peak at 546 nm was also lower for the Eu^{3+} and Tb^{3+} codoped sample than the Tb^{3+} doped one. One can notice that the emission spectra of Tb^{3+} in Y_2O_3 nanocrystal are slightly quenched by Eu^{3+} ions due to energy transfer from Tb^{3+} to Eu^{3+} . The luminescent spectra of $\text{Y}_2\text{O}_3:\text{Tb}^{3+}$ (1.25%), Eu^{3+} (5%), and $\text{Y}_2\text{O}_3:\text{Tb}^{3+}$ (1.25%) nanocolloids are shown in Figure 6. The intensity of the Eu^{3+} emission based on energy transfer from Tb^{3+} was analyzed in previous papers [28, 32].

Under 980 nm irradiation, upconversion spectra in the visible range from 500 nm–700 nm of $\text{Y}_2\text{O}_3:\text{Er}^{3+}$ (dash dot line) and $\text{Y}_2\text{O}_3:\text{Er}^{3+}, \text{Yb}^{3+}$ (solid line) are presented in Figure 7(a). The $\text{Er}^{3+}-\text{Er}^{3+}$ upconversion mechanism is explained in accordance with the energy schema (Figure 7(b), right). There is a great interest in the use of upconversion materials for efficient conversion of infrared radiation to visible light. This phenomenon has applications in several

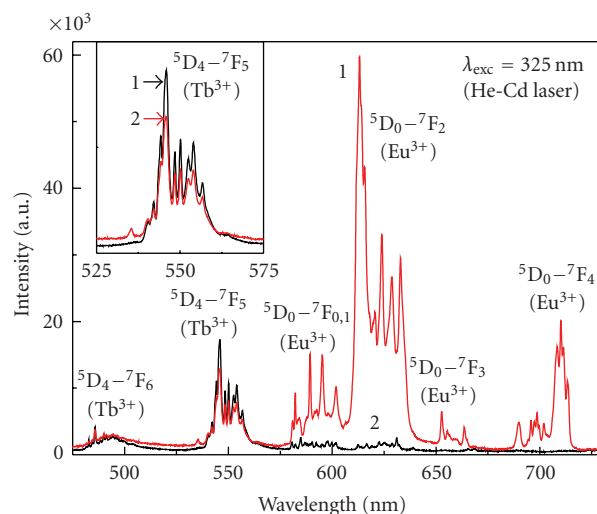


FIGURE 6: Luminescent spectra of $\text{Y}_2\text{O}_3:1.25\%\text{Tb}^{3+}$ (1) and $\text{Y}_2\text{O}_3:1.25\%\text{Tb}^{3+}, 5\%\text{Eu}^{3+}$ (2) nanocolloidal excited by He-Cd laser at 325 nm, inset to compare intensity of Tb^{3+} in $\text{Y}_2\text{O}_3:1.25\%\text{Tb}^{3+}$ and $\text{Y}_2\text{O}_3:1.25\%\text{Tb}^{3+}, 5\%\text{Eu}^{3+}$.

areas, such as upconversion lasing, and two photons fluorescence imaging, cathodoluminescence, and other applications. The Er^{3+} ion finds uses in laser materials and optical amplifiers under ground- and excited-state transitions near 800 and 980 nm, where high-power diodes are available [5]. In $\text{Y}_2\text{O}_3:\text{Er}^{3+}$ nanophosphor, the green and red fluorescence lines are observed in our samples after 800 nm excitation, owing to the transitions $({}^2\text{H}_{11/2}, {}^4\text{S}_{3/2}) \rightarrow {}^4\text{I}_{15/2}$ (515–575 nm) and ${}^4\text{F}_{9/2} \rightarrow {}^4\text{I}_{15/2}$ (640–690 nm) [26, 34]. Under 980 nm irradiation, the Er^{3+} ion is excited to the ${}^4\text{F}_{7/2}$ state via two successive energy transfers. An NIR photon from the pump beam will excite an Er^{3+} ion from the ${}^4\text{I}_{15/2}$ ground state to the ${}^4\text{I}_{11/2}$ state. Another Er^{3+} ion also in the ${}^4\text{I}_{11/2}$ state and in close proximity will transfer its energy to the initial ion, thereby exciting it to the ${}^4\text{F}_{7/2}$ state. The lower emitting levels are then populated via multiphonon relaxation and green and red emissions are then observed.

Interactions between two Er^{3+} ions cannot be ignored. Following the addition of Yb^{3+} ions, this process is greatly diminished due to the large absorption cross-section of the Yb^{3+} ions. The Er^{3+} absorption cross-section at this 980 nm wavelength is not very high. By the addition of Yb^{3+} , pumping promotes an electron from the ${}^2\text{F}_{7/2}$ ground state to the ${}^2\text{F}_{7/2}$ manifold of Yb^{3+} ; the excited Yb^{3+} ion then transfers its energy to the Er^{3+} ${}^4\text{I}_{11/2}$ level (Figure 7(b)).

Since the population of the ${}^4\text{I}_{13/2}$ level was increased, the lifetime was also increased. Two deleterious processes can also occur: via back energy transfer from Er^{3+} to Yb^{3+} ions, or double energy transfer, where a second excited Yb^{3+} ion transfers its energy to the Er^{3+} ion and promotes one electron from the ${}^4\text{I}_{11/2}$ to the ${}^4\text{F}_{7/2}$. When the Yb^{3+} concentration is enhanced, the Er^{3+} ions start to “see” Yb^{3+} ions and deleterious $\text{Er}^{3+} \leftrightarrow \text{Er}^{3+}$ energy exchanges are progressively replaced by the beneficial $\text{Yb}^{3+} \leftrightarrow \text{Er}^{3+}$ transfers.

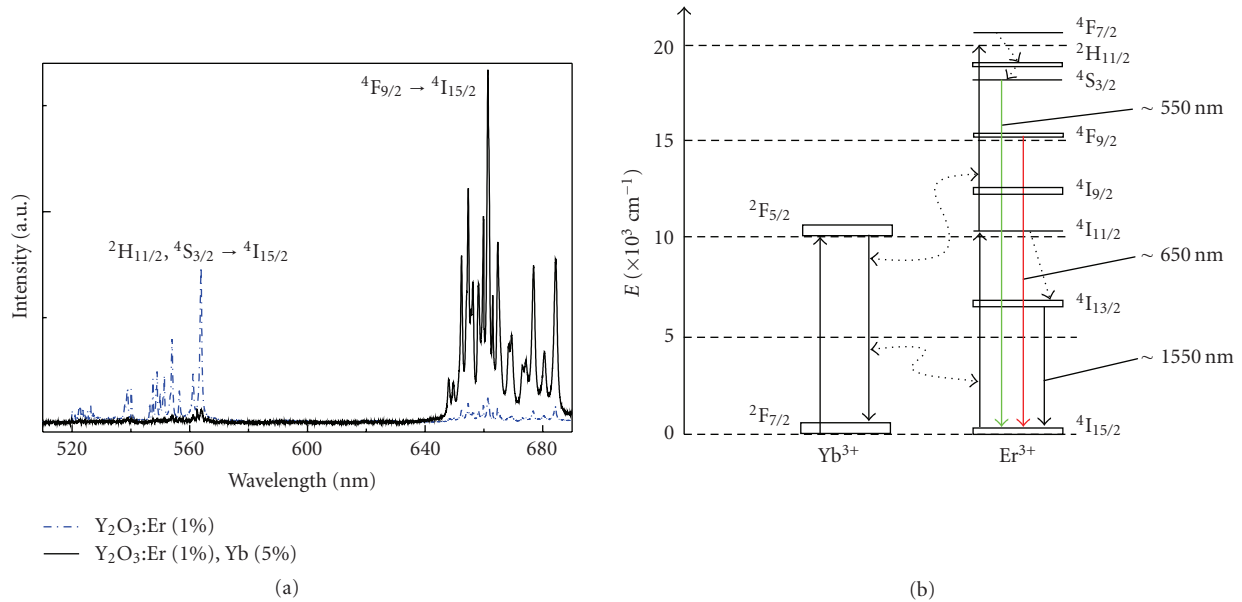


FIGURE 7: (a) Upconversion spectra in the visible range from 500 nm to 700 nm of $\text{Y}_2\text{O}_3:\text{Er}^{3+}$ (dash dotted line) $\text{Y}_2\text{O}_3:\text{Er}^{3+}, \text{Yb}^{3+}$ (solid line) following 980 nm irradiation, (b) energy schema presented the upconversion fluorescence interacted between Er-activator and Yb-sensitizer.

Comparing codoped $\text{Y}_2\text{O}_3:\text{Er}^{3+}, \text{Yb}^{3+}$ nanophosphors with Er^{3+} concentration varying from 0.1 to 5 mol% and 5 mol% Yb^{3+} , the optimal content for the luminescent intensity at 1538 nm ($^4\text{I}_{13/2}-^4\text{I}_{15/2}$ transition) is 1 mol% Er^{3+} . The upconversion in the red region 640–675 nm presents also a maximum for 1 mol% Er^{3+} . The effect of Er^{3+} concentration on upconversion luminescence of $\text{Y}_2\text{O}_3:\text{Er}^{3+}, \text{Yb}^{3+}$ is complicated depending on the power of the excitation laser. Red upconversion luminescence is caused by a two-photon process, when excitation power is high enough, as to the samples with lower concentration of Er^{3+} the intensity of green light is weaker than that of red light because more ions will non-radiatively decay from higher levels to $^2\text{H}_{11/2}$ and $^4\text{S}_{3/2}$ levels [30].

An advantage offered by our nanophosphors over the two-photon excitable organic dye is that the upconversion process in the $\text{Y}_2\text{O}_3:\text{Er}^{3+}, \text{Yb}^{3+}$ nanophosphor occurs by sequential multistep absorption through real states and is thus considerably stronger. One can use a low-power continuous wave diode laser in the near infrared region to excite the upconverted emission. By contrast, the two-photon absorption in organic dyes that is directed (simultaneous) requires a high-peak power pulse laser source for two-photon absorption through a virtual state. Figure 8 shows the luminescent intensities of the band at 564 nm and 1538 nm versus the excitation power at 803.7 nm of a diode laser.

3.4. Study energy transfer based on the decay times of fluorescence

The decay curves of Eu^{3+} and Tb^{3+} of $\text{Y}_2\text{O}_3:\text{Eu}^{3+}, \text{Tb}^{3+}$ nanopowders for $\text{Eu}^{3+}/\text{Tb}^{3+} = 9/1, 8/2,$ and $7/3$, respectively, (for 5 mol% rare earth ions) are presented in Figure 9(a) (Eu^{3+} emission at 612 nm) and Figure 9(b) (Tb^{3+} emission

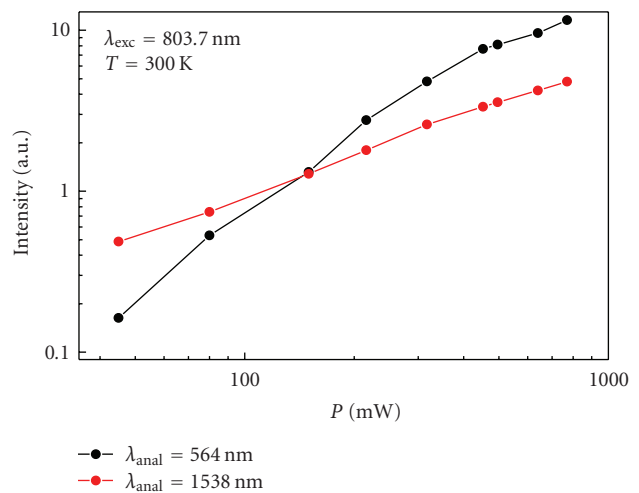


FIGURE 8: Luminescent intensities of the band at 564 nm and 1538 nm versus the excitation power at 803.7 nm.

at 546 nm). The decay curves being nonexponential, we have considered the normalized area S_N under the decay curve. The lifetimes of Eu^{3+} are 940, 360, and 650 microseconds for the case $\text{Eu}^{3+}/\text{Tb}^{3+} = 9/1, 8/2,$ and $7/3$, respectively. The lifetimes of Tb^{3+} decreased from 400 microseconds to 175 microseconds for the case $\text{Eu}^{3+}/\text{Tb}^{3+} = 9/1, 8/2,$ respectively, by ET process.

The results have indicated that the ratio between $\text{Eu}^{3+}/\text{Tb}^{3+}$ plays an important role in the ET process. The most effective ET is clearly for the sample with $\text{Eu}^{3+}/\text{Tb}^{3+}$ ratio of 8/2. The ET between Tb^{3+} and Eu^{3+} has been also investigated in Y_2O_3 crystals [4] and in $\text{Tb}_{1-x}\text{Eu}_x\text{P}_5\text{O}_{14}$ crystals [44]. Site-selective spectra and time-resolved spectra

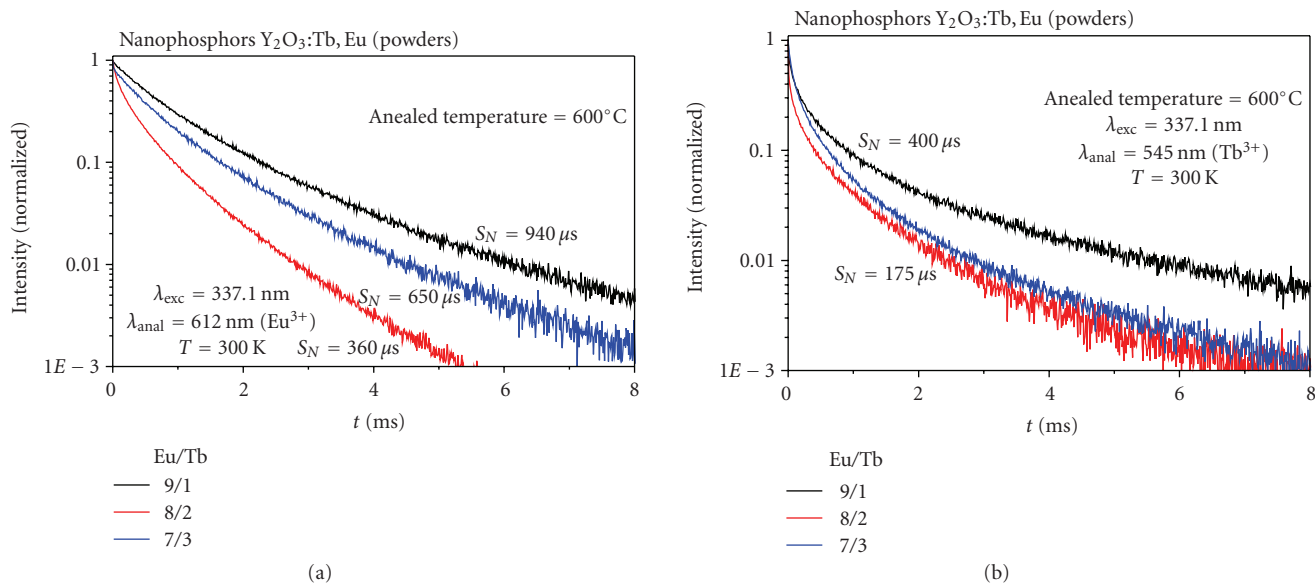


FIGURE 9: Decay curves at wavelength of 611 nm for Eu^{3+} (a) and of 545 nm for Tb^{3+} (b) in $\text{Y}_2\text{O}_3:\text{Eu}^{3+}, \text{Tb}^{3+}$ (5%) nanophosphor, annealed at 600°C , in 30 minutes.

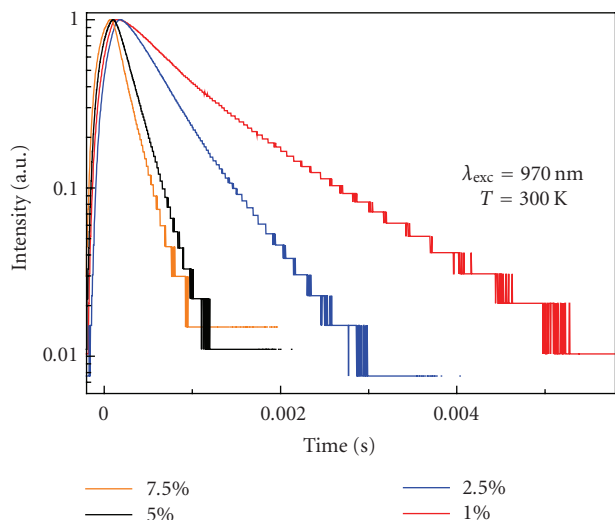


FIGURE 10: Decay curves for the band at 1535 nm of $\text{Y}_2\text{O}_3:\text{Er}^{3+}$ nanophosphor versus Er^{3+} -concentration, under excitation at 970 nm.

of $\text{Y}_2\text{O}_3:\text{Eu}^{3+}$ nanocrystal were investigated [45]. Recently, Hongei Song studies the dependence of photoluminescent properties of cubic $\text{Y}_2\text{O}_3:\text{Tb}^{3+}$ nanocrystal on particles size and temperature [46]. Up to now, our group is the only group which has studied energy transfer between $\text{Tb}^{3+}-\text{Eu}^{3+}$ in nanophosphors (powder and colloidal) of Y_2O_3 codoped with $\text{Tb}^{3+}-\text{Eu}^{3+}$.

In studying the decay behavior of the infrared emission of the ${}^4\text{I}_{13/2}-{}^4\text{I}_{15/2}$, transitions of Er^{3+} at 1535 nm depending on the Er-concentration from 1, 2.5, 5, 7.5, 10, up to 15 mol% have been measured for $\text{Y}_2\text{O}_3:\text{Er}^{3+}$ phosphor and presented in Figure 10. Under 970 nm excitation, the decay

times are not purely exponential. There are two kinds of lifetimes: the short lifetimes are 250, 150, 35, and 15 microseconds in the case of 1%, 2.5%, 7.5%, and 15% Er; the second long lifetime decreases from 1300, 620, and 110 microseconds to 80 microseconds, respectively. The lifetime of the emission IR increases as the concentration decreases. As for luminescence, it would be interesting to obtain a series of samples prepared under the same conditions and having undergone more significant temperatures of annealing, one could then determine the temperature from which one observes effects extinction. Lastly, let us note that the results of the spectra and the decays are coherent between them.

3.5. Application potential

Flat panel displays (FPDs) are thinner, lighter, and consume less than the conventional cathode-ray tube (CRT) displays. The field emission displays (FEDs) are the most promising FPDs technology. Rare earth-yttrium oxide is one of the important materials for application not only for FEDs, but also for waveguide and laser host. Enhancement of cathodoluminescent and photoluminescent properties of $\text{Y}_2\text{O}_3:\text{Eu}^{3+}$ luminescent films by vacuum cooling were observed [47], structural and optical properties of rare-earth-doped Y_2O_3 waveguides grown by pulsed-laser deposition were studied [48]. Growth of rare earth (RE-) doped concentration gradient crystal fibers and analysis of dynamical processes of laser resonant transitions in RE-doped Y_2O_3 (RE = $\text{Yb}^{3+}, \text{Er}^{3+}, \text{Ho}^{3+}$) were also studied [49]. Nanostructured $\text{ZnO}/\text{Y}_2\text{O}_3:\text{Eu}^{3+}$ for use as in luminescent polymer electrolyte composites was presented [50]. Thin films were prepared [51, 52] in order to apply for FPDs. The upconverting nanophores for bioimaging were presented in detail by Prasad [53]. The lifetimes of the nanophosphors

contained rare-earth ions in the range of millisecond and microsecond are compared to organic dye fluorescence with a lifetime typically in nanosecond. Specially, in our institute infrared cards were successfully proposed by mixing $\text{Y}_2\text{O}_3:\text{Er}^{3+}$, Yb^{3+} , or $\text{Y}_2\text{O}_3:\text{Er}^{3+}$ with polymethylmethacrylate (PMMA) with active imaging area of $20 \times 20 \text{ mm}^2$. These cards allow to detect a diode laser emitting at 980 nm with power of 7 mW/cm^2 . The red (655 nm–675 nm) or the green (520 nm–570 nm) emissions could be observed in depending on the concentration of Er-Yb couple. They are stable under 980 nm irradiation in the tropical conditions with humidity near to 90%. The optical coding systems based on the nanophosphors with ET luminescent and upconversion effect contained $\text{Eu}^{3+}\text{-Tb}^{3+}$ (excited by UV light at 370, 365, 337.1, and 325 nm) and $\text{Er}^{3+}\text{-Yb}^{3+}$ activators (excited by diode laser at 800 nm, 980 nm) have been successfully developed for examination of commercial products, banknote [28, 54, 55], nanobarcodes [53], or planar waveguide [56].

4. CONCLUSIONS

In this paper, we have presented two simple and efficient methods to prepare highly luminescent Y_2O_3 nanophosphor doped with Eu^{3+} , Tb^{3+} , Tm^{3+} , Er^{3+} , and Yb^{3+} . The average size and its distribution of the nanophosphor can be tailored sharply in nanoscale.

The optical properties and photophysical process, especially ET in Y_2O_3 host matrix, have been investigated and elucidated for improving the luminescence and upconversion processes.

Y_2O_3 nanophosphor in colloidal media with averaged size of 5 nm, narrow distribution, and spherical shape was successfully prepared. The colloidal are transparent and well stable at the concentration of 10%. The luminescence was strong and energy transfer was observed in $\text{Y}_2\text{O}_3:\text{Tb}^{3+}$, Eu^{3+} . The upconversion emission from $\text{Y}_2\text{O}_3:\text{Er}^{3+}$, Yb^{3+} nanophosphor is remarkable for developing an infrared display card. $\text{Y}_2\text{O}_3:\text{Tm}^{3+}$ together with both $\text{Y}_2\text{O}_3:\text{Tb}^{3+}$, Eu^{3+} and $\text{Y}_2\text{O}_3:\text{Er}^{3+}$, Yb^{3+} is good candidate for interesting application such as infrared cards and coding cards or biosensors. The transparent colloidal could be a promising approach for fabricating an optoelectronic thin film with higher optical quality.

ACKNOWLEDGMENTS

The authors would like to thank Professor Nguyen Van Hieu for his help, National Project for Advanced Materials Science and Technology, no. KC.02.14, National Nanoprogram 810304, the Basis research state projects of CB20 and Program for application of nanophosphors of Vietnamese Academy of Science and Technology 2007-2008 KHCN (financially supported this work). A part of the authors work was done in the National Key Laboratory of Electronic Materials and Devices, Institute of Materials Science, and Vietnamese Academy of Science and Technology.

REFERENCES

- [1] C. Feldmann, T. Jüstel, C. R. Ronda, and P. J. Schmidt, "Inorganic luminescent materials: 100 years of research and application," *Advanced Functional Materials*, vol. 13, no. 7, pp. 511–516, 2003.
- [2] A. S. Edelstein and R. C. Cammarata, Eds., *Nanomaterials: Synthesis, Properties and Applications*, Taylor & Francis, London, UK, 1998.
- [3] B. R. Ratna, A. D. Dinsmore, et al., "Nanophosphors: synthesis, properties and application," in *Proceedings of the 5th International Conference on the Science and Technology of Display Phosphors (ICSTDP '99)*, p. 295, San Diego, Calif, USA, November 1999.
- [4] T. K. Anh, T. Ngoc, P. T. Nga, V. T. Bich, P. Long, and W. Strek, "Energy transfer between Tb^{3+} and Eu^{3+} in Y_2O_3 crystals," *Journal of Luminescence*, vol. 39, no. 4, pp. 215–221, 1988.
- [5] S. Shionoya and W. M. Yen, *Phosphor Handbook*, CRC Press, Boca Raton, Fla, USA, 1999.
- [6] G. Blasse and B. C. Grabmaier, *Luminescent Materials*, Springer, Berlin, Germany, 1994.
- [7] H. Eilers and B. M. Tissue, "Laser Spectroscopy of Nanocrystals Eu_2O_3 and $\text{Eu}^{3+}:\text{Y}_2\text{O}_3$," *Chemical Physics Letters*, vol. 251, no. 1-2, pp. 74–78, 1996.
- [8] M. Kottaisamy, D. Jeyakumar, R. Jagannathan, and M. M. Rao, "Yttrium oxide: Eu^{3+} red phosphor by self-propagating high temperature synthesis," *Materials Research Bulletin*, vol. 31, no. 8, pp. 1013–1020, 1996.
- [9] B. Bihari, H. Eilers, and B. M. Tissue, "Spectra and dynamics of monoclinic Eu_2O_3 and $\text{Eu}^{3+}:\text{Y}_2\text{O}_3$ nanocrystals," *Journal of Luminescence*, vol. 75, no. 1, pp. 1–10, 1997.
- [10] T. Ye, Z. Guiwen, Z. Weiping, and X. Shangda, "Combustion synthesis and photoluminescence of nanocrystalline $\text{Y}_2\text{O}_3:\text{Eu}$ phosphors," *Materials Research Bulletin*, vol. 32, no. 5, pp. 501–506, 1997.
- [11] E. T. Goldburt, B. Kulkarni, R. N. Bhargava, J. Taylor, and M. Libera, "Size dependent efficiency in Tb doped Y_2O_3 nanocrystalline phosphor," *Journal of Luminescence*, vol. 72–74, pp. 190–192, 1997.
- [12] Q. Li, L. Gao, and D. Yan, "Effects of grain size on wavelength of $\text{Y}_2\text{O}_3:\text{Eu}^{3+}$ emission spectra," *Nanostructured Materials*, vol. 8, no. 7, pp. 825–831, 1997.
- [13] J. A. Cooper, H. G. Paris, S. R. Stock, C. J. Summers, and D. N. Hill, "Investigation of the effect of process variables on properties of europium-doped yttrium-oxide phosphor," *Journal of the Society for Information Display*, vol. 6, no. 3, pp. 163–166, 1998.
- [14] D. K. Williams, B. Bihari, B. M. Tissue, and J. M. McHale, "Preparation and fluorescence spectroscopy of bulk monoclinic $\text{Eu}^{3+}:\text{Y}_2\text{O}_3$ and comparison to $\text{Eu}^{3+}:\text{Y}_2\text{O}_3$ nanocrystals," *Journal of Physical Chemistry B*, vol. 102, no. 6, pp. 916–920, 1998.
- [15] A. Konrad, T. Fries, A. Gahn, et al., "Chemical vapor synthesis and luminescence properties of nanocrystalline cubic $\text{Y}_2\text{O}_3:\text{Eu}$," *Journal of Applied Physics*, vol. 86, no. 6, pp. 3129–3133, 1999.
- [16] T. K. Anh, N. Vu, P. T. M. Chau, L. Q. Minh, N. T. Oanh, and C. Barthou, "Preparation and optical properties of $\text{Y}_2\text{O}_3:\text{Eu}$ nanophosphors," in *Proceedings of the 3rd International Workshop on the Materials Science*, F. F. Bekker, N. D. Chien, J. J. M. Franse, T. D. Hien, N. T. Hien, and N. P. Thuy, Eds., Trends in Materials and Technology, pp. 320–323, Hanoi, Vietnam, November 1999.

- [17] J. A. Capobianco, F. Vetrone, T. D'Alesio, G. Tessari, A. Speghini, and M. Bettinelli, "Optical spectroscopy of nanocrystalline cubic $Y_2O_3:Er^{3+}$ obtained via combustion synthesis," *Physical Chemistry Chemical Physics*, vol. 2, pp. 3203–3207, 2000.
- [18] J. Zhang, Z. Zhang, Z. Tang, Y. Lin, and Z. Zheng, "Luminescent properties of $Y_2O_3:Eu$ synthesized by sol-gel processing," *Journal of Materials Processing Technology*, vol. 121, no. 2-3, pp. 265–268, 2002.
- [19] G. Y. Hong, B. S. Jeon, Y. K. Yoo, and J. S. Yoo, "Photoluminescence characteristics of spherical $Y_2O_3:Eu$ phosphors by aerosol pyrolysis," *Journal of the Electrochemical Society*, vol. 148, no. 11, pp. H161–H166, 2001.
- [20] T. Igarashi, M. Ihara, T. Kusunoki, K. Ohno, T. Isobe, and M. Senna, "Relationship between optical properties and crystallinity of nanometer $Y_2O_3:Eu$ phosphor," *Applied Physics Letters*, vol. 76, no. 12, pp. 1549–1551, 2000.
- [21] C. Feldmann, "Polyol-mediated synthesis of nanoscale functional materials," *Advanced Functional Materials*, vol. 13, no. 2, pp. 101–107, 2003.
- [22] R. Bazzi, M. A. Flores-Gonzalez, C. Louis, et al., "Synthesis and luminescent properties of sub-5-nm lanthanide oxides nanoparticles," *Journal of Luminescence*, vol. 102-103, pp. 445–450, 2003.
- [23] G. Wakefield, E. Holland, P. J. Dobson, and J. L. Hutchison, "Luminescence properties of nanocrystalline $Y_2O_3:Eu$," *Advanced Materials*, vol. 13, no. 20, pp. 1557–1560, 2001.
- [24] T. K. Anh, "The role of active centre concentration in the phenomena of energy transfer in lanthanide compounds," Doctoral thesis, Wroclaw-Warsaw, Poland, 1987.
- [25] D. R. Tallant, C. H. Seager, and R. L. Simpson, "Energy transfer and relaxation in europium-activated Y_2O_3 after excitation by ultraviolet photons," *Journal of Applied Physics*, vol. 91, no. 7, pp. 4053–4064, 2002.
- [26] N. Vu, T. K. Anh, L. Q. Minh, and C. Barthou, "Optical properties of Er^{3+} doped Y_2O_3 nanophosphors," *Communication in Physics*, vol. 12, pp. 119–123, 2002.
- [27] T.-L. Phan, M. H. Phan, N. Vu, T. K. Anh, and S.-C. Yu, "Luminescent properties of Eu-doped Y_2O_3 nanophosphors," *Physica Status Solidi (a)*, vol. 201, no. 9, pp. 2170–2174, 2004.
- [28] T. K. Anh, L. Q. Minh, N. Vu, et al., "Nanomaterials containing rare-earth ions Tb, Eu, Er and Yb: preparation, optical properties and application potential," *Journal of Luminescence*, vol. 102-103, pp. 391–394, 2003.
- [29] N. Vu, T. K. Anh, C. Barthou, and L. Q. Minh, "Preparation, optical properties and up conversion effect of the nanophosphors doped with Er and Yb rare earth ions," in *Proceedings of the 9th Asia Pacific Physics Conference (APPC '04)*, pp. 579–580, Hanoi, Vietnam, October 2004.
- [30] N. Vu, *Preparation, optical properties of nanophosphors $Y_2O_3:Eu, Tb, Er$ and Yb* , Ph.D. thesis, Institute of Materials Science, Hanoi, Vietnam, 2007.
- [31] N. Nguyen, M. H. Nam, T. K. Anh, L. Q. Minh, and E. Tanguy, "Optical properties of Eu^{3+} doped Y_2O_3 nanophosphors," *Advances in Natural Sciences*, vol. 6, pp. 119–123, 2006.
- [32] T. K. Anh, L. T. K. Giang, N. Vu, et al., "Luminescence and energy transfer of Y_2O_3 nanocolloidal containing rare earth ions," *Journal on Science and Technology for Development*, vol. 24, pp. 85–93, 2007.
- [33] N. Vu, T. K. Anh, G.-C. Yi, and W. Strek, "Photoluminescence and cathodoluminescence properties of $Y_2O_3:Eu$ nanophosphors prepared by combustion synthesis," *Journal of Luminescence*, vol. 122-123, pp. 776–779, 2007.
- [34] J. A. Capobianco, F. Vetrone, J. C. Boyer, A. Speghini, and M. Bettinelli, "Enhancement of red emission ($^4F_{9/2} \rightarrow ^4I_{15/2}$) via upconversion in bulk and nanocrystalline cubic $Y_2O_3:Er^{3+}$," *Journal of Physical Chemistry B*, vol. 106, no. 6, pp. 1181–1187, 2002.
- [35] D. Matsuura, "Red, green, and blue upconversion luminescence of trivalent-rare-earth ion-doped Y_2O_3 nanocrystals," *Applied Physics Letters*, vol. 81, no. 24, pp. 4526–4528, 2002.
- [36] A. M. Pires, O. A. Serra, and M. R. Davolos, "Morphological and luminescent studies on nanosized Er, Yb-yttrium oxide up-converter prepared from different precursors," *Journal of Luminescence*, vol. 113, no. 3-4, pp. 174–182, 2005.
- [37] F. Vetrone, J. C. Boyer, J. A. Capobianco, A. Speghini, and M. Bettinelli, "Effect of Yb^{3+} codoping on the up conversion emission in nanocrystalline $Y_2O_3:Er^{3+}$," *Journal of Physical Chemistry B*, vol. 107, no. 5, pp. 1107–1112, 2003.
- [38] G. De, W. Qi, J. Zhang, et al., "Upconversion luminescence properties of $Y_2O_3:Yb^{3+}, Er^{3+}$ nanostructures," *Journal of Luminescence*, vol. 119-120, pp. 258–263, 2006.
- [39] C. Strohhofer and A. Polman, "Absorption and emission spectroscopy in Er^{3+} - Yb^{3+} doped aluminum oxide waveguides," *Optical Materials*, vol. 21, no. 4, pp. 705–712, 2003.
- [40] SIEMENS, *Profile User's Guide*, 1994, Diffrac-AT, Version 3.2.
- [41] SIEMENS Win-Crysize, 1998.
- [42] T. Inami, M. Kobiyama, S. Okuda, H. Maeta, and H. Ohtsuka, "Grain size measurement of nanocrystalline gold by X-ray diffraction method," *Nanostructured Materials*, vol. 12, no. 5–8, pp. 657–660, 1999.
- [43] L. T. C. Tuong and P. V. Phuc, "Determination of nanocrystal-sizes and their distribution by X-ray diffraction method for $Y_2O_3:Eu$ nanophosphors," in *Proceedings of the International Workshop on Optics and Spectroscopy*, pp. 501–504, Hanoi, Vietnam, March-April 2000.
- [44] T. K. Anh and W. Strek, "Dynamics of energy transfer in $Tb_{1-x}Eu_xP_5O_{14}$ crystals," *Journal of Luminescence*, vol. 42, no. 4, pp. 205–210, 1988.
- [45] H. Song and J. Wang, "Dependence of photoluminescent properties of cubic $Y_2O_3:Tb^{3+}$ nanocrystals on particle size and temperature," *Journal of Luminescence*, vol. 118, no. 2, pp. 220–226, 2006.
- [46] Z. Wei-Wei, X. Mei, Z. Wei-Ping, et al., "Site-selective spectra and time-resolved spectra of nanocrystalline $Y_2O_3:Eu$," *Chemical Physics Letters*, vol. 376, no. 3-4, pp. 318–323, 2003.
- [47] D. Kumar, J. Sankar, K. G. Cho, V. Craciun, and R. K. Singh, "Enhancement of cathodoluminescent and photoluminescent properties of $Eu:Y_2O_3$ luminescent films by vacuum cooling," *Applied Physics Letters*, vol. 77, no. 16, pp. 2518–2520, 2000.
- [48] O. Pons-Y-Moll, J. Perriere, E. Millon, et al., "Structural and optical properties of rare-earth-doped Y_2O_3 waveguides grown by pulsed-laser deposition," *Journal of Applied Physics*, vol. 92, no. 9, pp. 4885–4890, 2002.
- [49] L. Laversenne, C. Goutaudier, Y. Guyot, M. Th. Cohen-Adad, and G. Boulon, "Growth of rare earth (RE) doped concentration gradient crystal fibers and analysis of dynamical processes of laser resonant transitions in RE-doped Y_2O_3 (RE= $Yb^{3+}, Er^{3+}, Ho^{3+}$)," *Journal of Alloys and Compounds*, vol. 341, no. 1-2, pp. 214–219, 2002.
- [50] M. Abdullah, C. Panatarani, T.-O Kim, and K. Okuyama, "Nanostructured $ZnO/Y_2O_3:Eu$ for use as in luminescent polymer electrolyte composites," *Journal of Alloys and Compounds*, vol. 377, no. 1-2, pp. 298–305, 2004.

- [51] N. Joffin, J. Dexpert-Ghys, M. Verelst, G. Baret, and A. Garcia, "The influence of microstructure on luminescent properties of $Y_2O_3:Eu$ prepared by spray pyrolysis," *Journal of Luminescence*, vol. 113, no. 3-4, pp. 249–257, 2005.
- [52] S.-S. Yi, J. S. Bae, B. K. Moon, J. H. Jeong, J.-C. Park, and I. W. Kim, "Enhanced luminescence of pulsed-laser-deposited $Y_2O_3:Eu^{3+}$ thin-film phosphors by Li doping," *Applied Physics Letters*, vol. 81, no. 18, pp. 3344–3346, 2002.
- [53] P. N. Prasad, *Nanophotonic*, Wiley-Interscience, New York, NY, USA, 2004.
- [54] T. K. Anh, N. Vu, T. T. Huong, and L. Q. Minh, "Nanomaterials containing rare earth ions for infrared card and planar waveguide applications," in *The 2nd International Workshop on Nanophysics and Nanotechnology (IWONN '04)*, pp. 161–164, Hanoi, Vietnam, October 2004.
- [55] T. K. Anh, L. T. K. Giang, L. D. Tuyen, et al., "Oxide nanoparticles and colloidal, preparation, optical properties and application potential," in *Proceedings of the 1st International Workshop on Functional Materials and the 3rd International Workshop on Nanophysics and Nanotechnology*, pp. 424–427, Halong, Vietnam, December 2006.
- [56] T. T. Huong, T. K. Anh, M. H. Nam, C. Barthou, W. Streck, and L. Q. Minh, "Preparation and infrared emission of silica-zirconia-alumina doped with erbium for planar waveguide," *Journal of Luminescence*, vol. 122-123, pp. 911–913, 2007.

Research Article

Rare-Earth Doped Nanocrystalline Phosphors for Field Emission Displays

P. Psuja, D. Hreniak, and W. Strek

Institute of Low Temperature and Structure Research, Polish Academy of Sciences, Okólna 2, Wrocław 50-422, Poland

Received 25 April 2007; Accepted 14 December 2007

Recommended by Tran Kim Anh

The cathodoluminescence properties of rare-earth (RE = Ce, Eu, Tb) doped nanocrystalline phosphors (Y_2O_3 , $Y_3Al_5O_{12}$) were investigated. Their structure and morphology were determined and correlated with optical properties. The effect of grain sizes on emission yield of RE doped nanophosphors has been investigated. A possibility of application of RE doped nanophosphors for efficient field emission display (FED) devices has been discussed.

Copyright © 2007 P. Psuja et al. This is an open access article distributed under the Creative Commons Attribution License, which permits unrestricted use, distribution, and reproduction in any medium, provided the original work is properly cited.

1. INTRODUCTION

Phosphors are efficient luminescent materials and irreplaceable components of light-emitting devices like cathode ray tubes (CRTs), plasma display panels (PDPs), and field emission displays (FEDs). The last ones have gained a great interest [1] and have been recognized as one of the most promising technologies in the flat panel displays (FPDs) market [2–6] due to their most important features like great brightness, wide horizontal and vertical view angles, good contrast ratio, high efficiency with a low power consumption, short response time, and wide work temperature range. The PDPs in contrast to the liquid crystal displays (LCDs) [7] are characterized by low contrast ratio, low view angle, and narrow operating temperature range, but they have low efficiency and high power consumption resulting in overwarming during work [6, 8, 9]. Such behaviors do not appear in FEDs at all. Additionally, FEDs have high brightness (3000 cd/m^2) and very high efficiency ($2 \text{ W/10.4}''$). The only problem that appears in FEDs is that the operating time is shorter than in the case of other described technologies. This problem is connected with progressive degradation of vacuum level in the display space [10–13]. There are three main sources of gasses in FEDs. The first one is the gas emitted during device encapsulation process [11]. The second source of gasses is the employment of inappropriate materials (e.g., porous glasses) in the device construction [10, 13]. The third and most important source of gasses is improper type of phosphors [6, 10, 12, 13]. Examples of that class of phosphors

are semiconductors and insulators containing sulfur in the host material composition [10, 14–20], for example, ZnS , $ZnSO_4$, and $Y(\text{La,Gd})_2O_2S$. The example of the abovementioned influence of SO_2 and other gasses on FED operation has been presented in detail and discussed in work [12]. For the same reasons CdS , PbS , and $Zn(\text{Cd})S$ phosphors or even $CdSe/ZnS$ quantum dots composites need to be eliminated [6, 21]. Besides, they consist of harmful cadmium and lead which classified those materials as dangerous and disqualified from commercial application.

Other problem is a decrease of cathodoluminescence efficiency by negative loading of grain surface in phosphor layer. That is why the electrical conductivity of phosphors should be high enough to avoid charge accumulation [18, 22, 23].

The above considerations lead to a conclusion that new class of phosphors needs to be applied in field emission displays. One of the most promising solutions is rare-earth (RE) doped garnets, oxides, silicates, and some perovskites [14, 18–20, 24–26]. Unfortunately, most of them are insulators. This disadvantage could be neutralized by modulation of phosphor grain size. At present, a large majority of efforts concentrate on application of nano- and eventually submicron-size particle phosphors [27–36]. Some experimental [36, 37] and theoretical considerations [38] promote as the most efficient phosphors with submicron grain size of spherical shape [39]. However, nanoparticle phosphors could be appropriate for low voltage FED application [38]. Besides, they have a lot of other advantages and create new possibilities [16, 17, 39, 40]. In some cases, the preparation

of nanocrystalline phosphors requires much less temperature and time in comparison with conventional micro- or submicro-size grains [16, 39, 40]. Application of small grains close to spherical shape influences the efficiency of the phosphor layer and the quality of the displayed picture [39]. The employment of such materials allowed for optimal packaging of grains, avoids cutting of the picture spot and decreases scattering of emitted light in the layer [39]. Moreover, application of nanocrystalline luminescent powders allowed the fabrication of very thin light emitting film and fundamentally decreased the total resistance of phosphor layer. The thickness of the layer is connected with lower amount of gasses bound between the phosphor grains [40]. The effluent of those gasses during device operation can affect degradation of vacuum level and seriously shorten the display operating time [12, 13].

Another potential benefit connected with application of nanocrystals is a possibility of increasing conductivity of phosphors by mixing them with transparent, conductive nanocrystalline powders [41–43].

Recently, another approach towards increasing phosphor conductivity is an application of more conductive host materials like RE doped stannous oxide nanopowders [44–46]. The electrical, structural, and optical properties of SnO_2 [47–49] have focused attention on similar phosphors.

According to the above assumptions, the RE doped nanocrystalline oxides or garnets (Y_2O_3 , SnO_2 , and $\text{Y}_3\text{Al}_5\text{O}_{12}$) [50] seem to be very promising candidates for FED phosphor application. The question is about their efficiency in comparison with conventional, commercially available, micrograin size phosphors. A very important question is also the CIE (*Commission Internationale d'Eclairage*) coordinates of the phosphors. The coordinates should be suitable for application in field emission displays.

To answer these questions, we have performed the systemic studies of the nanocrystalline RE doped oxides. In particular, we have been focusing on the grain size effect on efficiency of low-voltage cathodoluminescence. We expect that the results and discussion presented in this work will contribute to the application of RE doped nanocrystalline phosphors in FED devices.

2. EXPERIMENTAL

The following nanocrystalline RE doped oxides were chosen for our studies: $\text{Eu}^{3+}:\text{Y}_2\text{O}_3$, $\text{Tb}^{3+}:\text{Y}_2\text{O}_3$, $\text{Tb}^{3+}:\text{Y}_3\text{Al}_5\text{O}_{12}$ (Tb:YAG), $\text{Ce}^{3+}:\text{YAG}$, and $\text{Tb}^{3+}:\text{YAG}/\text{Eu}^{3+}:\text{YAG}$. The phosphors have been synthesized by modified Pechini method [40, 51, 52]. The powders were sintered at different temperatures to obtain a different grain size. The structures of fabricated materials were confirmed by X-ray diffraction (XRD) by means of a stoe powder sensitive detector, filtered $\text{CuK}\alpha_1$ radiation. The average powder grain sizes were estimated from broadening of diffraction peaks, by using Scherrer equation [40, 51]. In this work, we presented the results calculated only for europium and terbium doped yttria samples (see Figure 1). The powders were then deposited by electrophoresis [53–55] on ITO glass slides [56]. As a surfactant, magnesium nitride has been used. In the last part of the procedure, the substrates were

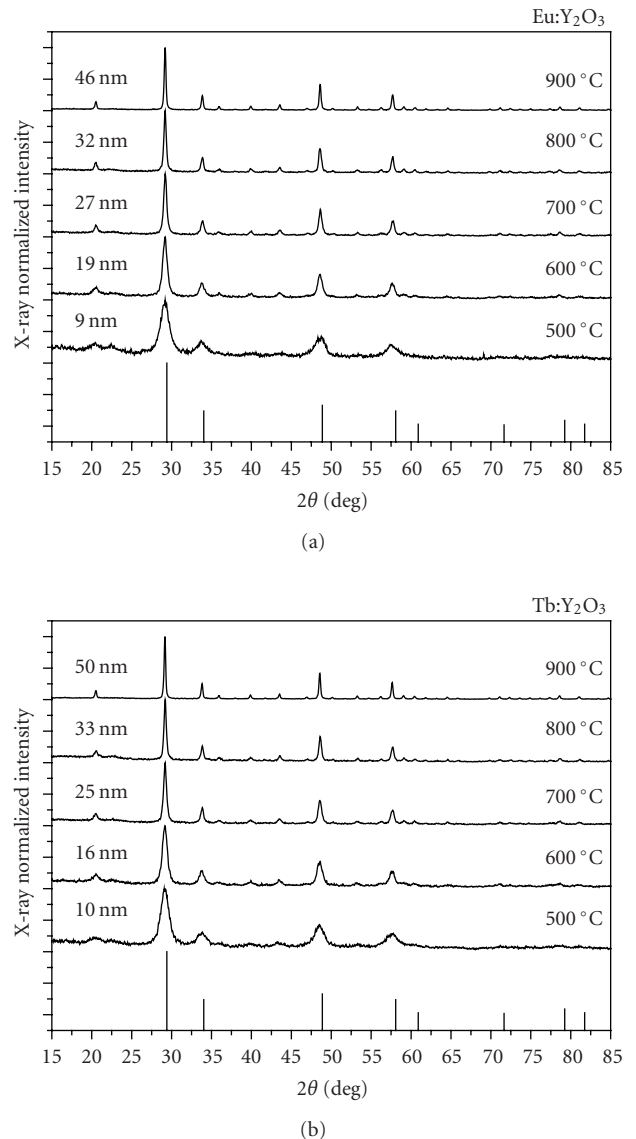


FIGURE 1: The XRD patterns of (a) $\text{Eu}:\text{Y}_2\text{O}_3$ and (b) $\text{Tb}:\text{Y}_2\text{O}_3$ nanocrystallites sintered in different temperatures.

hold in temperature of about 450°C to consolidate the layer by transforming MgOH^+ into MgO . In the future attempts, it is worth to replace $\text{Mg}(\text{NO}_3)_2$ by indium nitride or appropriate indium and tin salts.

The CL measurements [40] of the phosphor layers have been done in the setup earlier described by us [57]. The conditions of measurement device will simulate real carbon nanotubes field emission display (CNT-FED) environment. The cold cathode was made of double walled carbon nanotubes (DWNT) deposited on ITO glass slide. The emissive properties of the cathodes made in that manner were presented elsewhere [40, 57–59]. The distance between phosphor's covered anode plate and cathode plate was $250\ \mu\text{m}$ [56, 57]. The experimental conditions and procedure were similar to those described in [40, 50]. The current density of $0.9\ \text{mA}/\text{cm}^2$ for $3.2\ \text{V}/\mu\text{m}$ was registered for a diode configuration. The

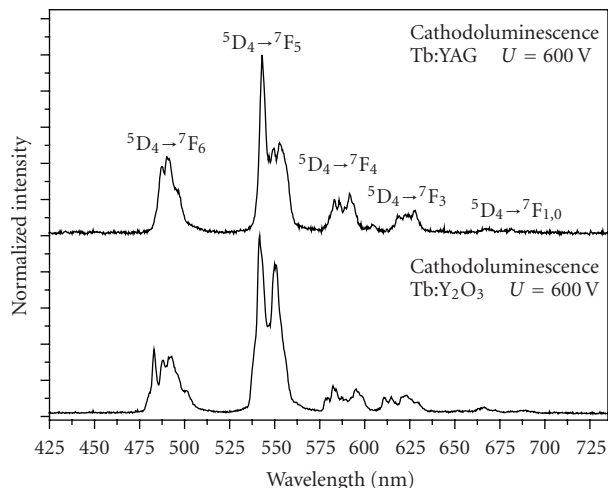


FIGURE 2: A comparison of low-voltage CL spectra registered for Tb:YAG and Tb:Y₂O₃ nanocrystallites.

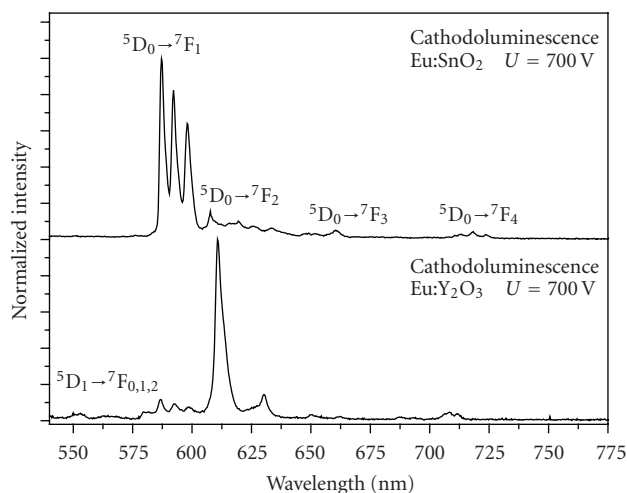


FIGURE 3: A comparison of low-voltage CL spectra registered for Eu:SnO₂ and Eu:Y₂O₃ nanocrystallites.

vacuum level in the device was determined to be 1×10^{-6} Torr. The low-voltage CL spectra (see Figures 2–5) were registered using CCD handy fiber spectrophotometer Avantes 350 with a 1000 nm spectral range and a 0.35 nm resolution.

In the second phase of the experiment, the nanopowders (Eu³⁺:Y₂O₃, Tb³⁺:Y₂O₃) were sintered at different temperatures (500°C, 600°C, 700°C, 800°C, 900°C). Then, they were mechanically mixed with a ZnS:Ag micrograin size phosphor (Phosphor Technology) and with micrograins size Cr:Al₂O₃. The micrograin size phosphors were chosen as the reference light emitting materials to study the effect of size of nanograins on output light intensity. The mass ratio of ZnS:Ag to Eu:Y₂O₃ was taken as 2:1, and in the case of Cr:Al₂O₃ to Tb:Y₂O₃, it is 4:1. The aim of this experiment was to examine the influence of grain sizes of nanopowders on intensity of luminescence by reference to the peaks connected with radiative transitions in ZnS:Ag (450 nm) and Cr:Al₂O₃

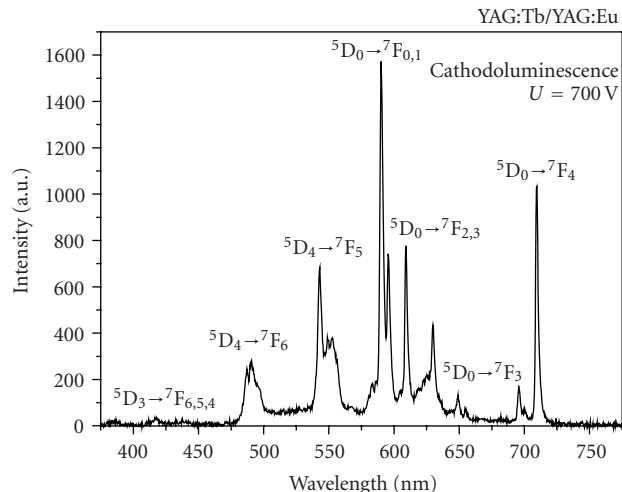


FIGURE 4: The low-voltage CL spectra of Eu:YAG/Tb:YAG blend proposed as white light emitting phosphor.

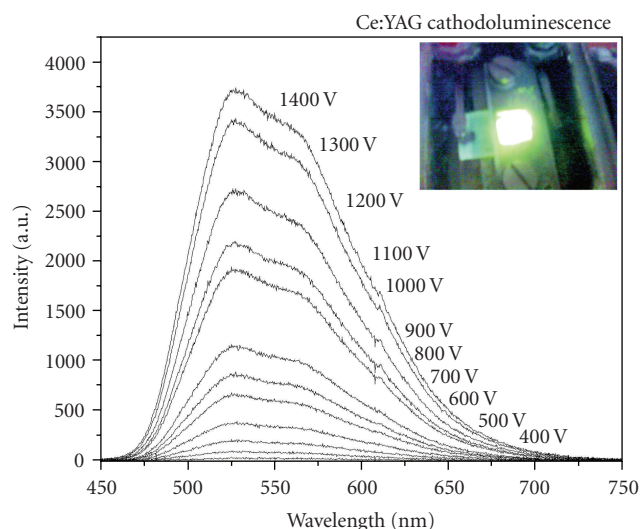


FIGURE 5: The dependence of CL spectra of Ce:YAG nanocrystals on applied voltage.

(694,1 nm). This method allowed measuring the photo- and cathodoluminescence properties. The grains size effect on photoluminescence was examined for ZnS:Ag/Eu:Y₂O₃ samples. To compare the intensity of powders with different size of nanograins, the samples with the microcrystalline powder of Eu:Y₂O₃ (Phosphor Technology) as a reference have been prepared. The medium grain size in this sample has been specified by the supplier to be 3.5 μm. The samples were excited using $\lambda_{exc} = 266$ nm of Nd:YAG laser system. The high voltage cathodoluminescence (accelerating voltage $U = 90$ kV) has been measured in specially adopted BS 500 TESLA TEM microscope chamber on Cr:Al₂O₃/Tb:Y₂O₃ electrophoretically deposited layers. The results of both experiments are depicted in Figures 6 and 7.

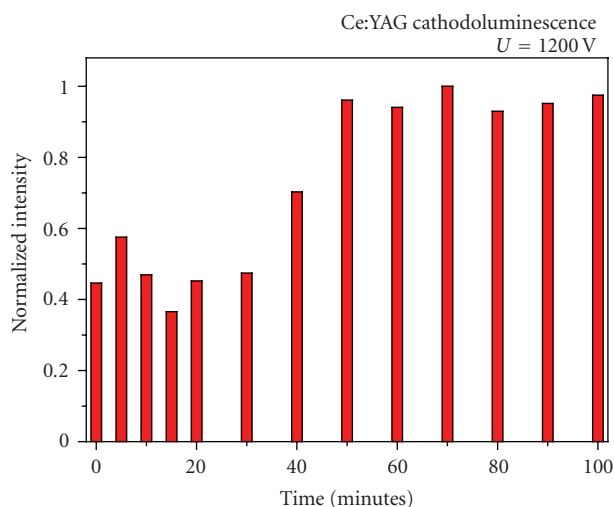


FIGURE 6: The CL time stability measured for Ce:YAG nanocrystals.

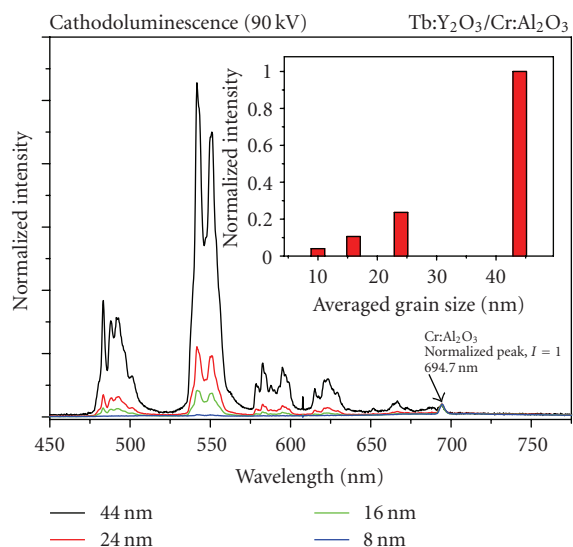


FIGURE 7: A comparison of cathodoluminescence (90 kV) of $\text{Tb:Y}_2\text{O}_3/\text{Cr:Al}_2\text{O}_3$ blend with different sizes of $\text{Tb:Y}_2\text{O}_3$ nanocrystallites.

3. RESULTS AND DISCUSSION

3.1. Structure

The XRD patterns of $\text{Tb:Y}_2\text{O}_3$ and $\text{Eu:Y}_2\text{O}_3$ nanocrystalline powders shown in Figures 1 and 2 were measured for the samples sintered at different temperatures. Following the Scherrer formula, we have determined the average grain sizes varying since 9 nm for 500°C to 46 nm for 900°C in the case of $\text{Eu:Y}_2\text{O}_3$ (see Figure 1(a)), and since 10 nm to 50 nm in the case of $\text{Tb:Y}_2\text{O}_3$ (see Figure 1(b)).

3.2. Cathodoluminescence

All the samples under investigation have demonstrated the low-voltage cathodoluminescent properties. The intensity of

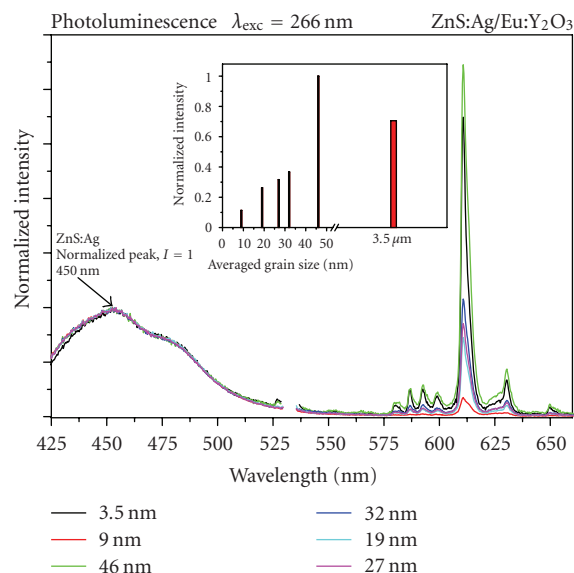


FIGURE 8: A comparison of photoluminescence ($\lambda_{\text{exc}} = 266$ nm) of $\text{Eu:Y}_2\text{O}_3/\text{ZnS:Ag}$ blend with different sizes of $\text{Eu:Y}_2\text{O}_3$ nanocrystallites. A comparison of $\text{Eu:Y}_2\text{O}_3$ intensity has been presented in the middle of the figure.

emitted light has increased with increasing applied voltage (see Figure 5). The mixed Tb:YAG (green) and Eu:YAG (red) powders have emitted the yellowish-white light (see Figure 4). The spectra of nanophosphors were grouped and depicted regarding colors to compare the spectra (see Figures 2 and 3).

3.3. Time stability

The time stability measurements on nanophosphors subjected to cathodoluminescence process have been carried out for the Ce:YAG nanophosphor. It was observed that after first switch on light, the cathodoluminescence intensity stabilizes after 50 minutes; the time stability of emitted light measured in the next 50-minute period was satisfying (see Figure 6). Following our earlier studies, we could suggest that this delay is connected with time needed for cold cathode activation. Some residual contaminations should be removed from CNT-ITO cathode surface.

3.4. CIE chromatic coordinates

The CIE chromatic coordinates were analyzed on example of red light emitting phosphors. It is commonly known that the coordinates and luminescent spectra depend strongly upon doped ion and host [18]. Both Ce^{3+} and Eu^{3+} could be very good examples as an experimental confirmation of this thesis. What is shown in this work analysis is focused on Eu^{3+} ion. The features of Pr^{3+} doped CaTiO_3 has been also presented and compared to Eu:SnO_2 , $\text{Eu:Y}_2\text{O}_3$, $\text{Eu:Y}_2\text{O}_2\text{S}$ (see Figure 9). The emitted color transforms from deep bloody red for Pr:CaTiO_3 by fire red for $\text{Eu:Y}_2\text{O}_2\text{S}$ and $\text{Eu:Y}_2\text{O}_3$ to orange-red for Eu:SnO_2 . However, all examined phosphors are able to use as red phosphors in FEDs and as component

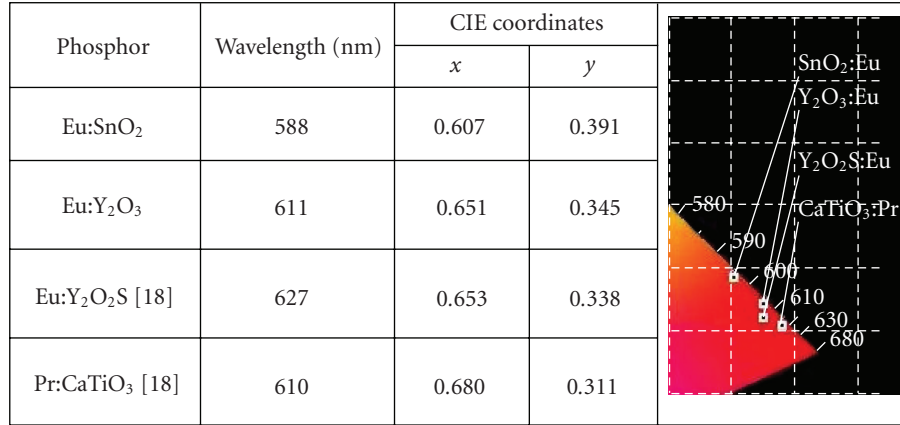


FIGURE 9: The comparison of CIE coordinate of different red phosphors.

of white light emitting phosphor for light source. Moreover, the Eu:SnO₂/Pr:CaTiO₃ and Eu:Y₂O₃/SnO₂ may be mechanically mixed with different mass ratios in order to tune the CIE coordinates of phosphor.

3.5. Size effects

The dependences of Cr:Al₂O₃/Tb:Y₂O₃ cathodoluminescence and ZnS:Ag/Eu:Y₂O₃ photoluminescence on the grain size are shown in Figures 7 and 8. The spectra were compared and normalized to the peak connected with the Cr:Al₂O₃ phosphorescence for cathodoluminescence measurements and to the peak connected with the ZnS:Ag luminescence in the case of photoluminescence. It is seen that in the nanophosphors, the light intensity increases with increasing average grain size. Moreover, a comparison of the photoluminescence spectra of micro- and nanograin sizes of ZnS:Ag/Eu:Y₂O₃ blend has demonstrated that the intensity of 3.5 μ m grain size powder of Eu:Y₂O₃ (Phosphor Technology) was about 70% of intensity of 46 nm grain size of europium doped yttria nanocrystallites synthesized by modified Pechini method [25, 27, 40, 51, 52]. An enhancement of the emission with grain size which is related to sintering temperature could be rationalized by a concept of the effective refractive index. It is well known that the radiative processes in nanocrystals of oxides doped with rare-earth ions strongly depend on the size, shape, and refractive indices of their surroundings [60–62]. The influence of the grain sizes on the luminescence lifetimes of Nd³⁺ doped YAG particles was earlier observed by Christensen et al. [60]. The emission intensity I is directly related with the Einstein coefficient for spontaneous emission A according to $I = h\nu AN$, where N is the population of centers emitting the energy $h\nu$. The Einstein coefficient A is simply related to the effective refractive index n_{eff} by the relation $A \propto \chi S$, where $\chi = (n_{\text{eff}}(n_{\text{eff}}^2 + 2)^2)/9$ and S is the dipole strength. Following the model of Meltzer [61], we may assume that the effective refractive index $n_{\text{eff}}(X) = x n_{\text{grain}} + (1 - x) n_{\text{surr}}$ is related to the filling factor x which shows the fraction of the sample

volume occupied by nanocrystals (n_{grain} is the refractive index of the material of the grain, n_{surr} is the refractive index of the medium surrounding the nanograins). Since for the same mass of powders with the same concentration of luminescent ions the filling factor is less for nanosize grains compared to microsize grains, the effective refractive index will be bigger for nanophosphors.

4. CONCLUSIONS

The results of present work clearly indicate that the nanocrystalline RE doped phosphors may effectively replace the microsize phosphors in FED devices. It is obvious that the layer made of nanocrystallites can be much thinner compared to the layer made of microsize phosphor grains. That has an impact both on total resistivity of the layer and amount of residual gasses bounded between the grains. Both these factors influence the efficiency of the light source, long time stability of the intensity of emitted light, and device lifetime. The light intensity of examined phosphors was stable during measurements. The emitted light intensity had increased with increasing applied voltage. A comparison of photo- and cathodoluminescent intensities of the layers and powders allows concluding that in the nanorange, the emitted light efficiency increases with increasing grain size. The second observation was that Eu:Y₂O₃ nanopowder (900°C, 46 nm) was more efficient than commercially available micrograin size phosphor (3.5 μ m). The CIE chromatic coordinates did not change with phosphor grain sizes.

ACKNOWLEDGMENTS

The authors would like to thank Mrs. M. Sledz for XRD measurements and Dr. M. Zawadzki for high-voltage CL measurements. Special thanks for Phosphor Technology Ltd. Company for providing the authors with micrograin size phosphors. The works were supported by Polish Ministry of Sciences and Highest Education (Project no. N507 076 32/2186).

REFERENCES

- [1] A. Ghis, R. Meyer, P. Rambaud, F. Levy, and T. Leroux, "Sealed vacuum devices: fluorescent microtip displays," *IEEE Transactions on Electron Devices*, vol. 38, no. 10, pp. 2320–2322, 1991.
- [2] K. Derbyshire, "Beyond AMLCDs: field emission displays," *Solid State Technology*, vol. 37, no. 11, pp. 55–65, 1994.
- [3] G. Thomas, "New displays move into the market," *Physics World*, vol. 10, no. 6, pp. 31–32, 1997.
- [4] I. Shah, "Field-emission displays," *Physics World*, vol. 10, pp. 45–48, 1997.
- [5] B. R. Chalamala, Y. Wei, and B. E. Gnade, "FED up with fat tubes," *IEEE Spectrum*, vol. 35, no. 4, pp. 42–51, 1998.
- [6] R. Waser, *Nanoelectronics and Information Technology*, chapter 39, WILEY-VCH, Weinheim, Germany, 2003.
- [7] D. Hsieh and B. Young, "Manufacturing small- and medium-sized displays," *SID Information Display*, vol. 20, no. 7, pp. 26–31, 2004.
- [8] J. Deschamps and H. Doyeux, "Plasma displays," *Physics World*, vol. 10, pp. 39–43, 1997.
- [9] L. F. Weber, "Do LCD TVs really last longer than PDP TVs," *SID Information Display*, vol. 20, no. 8, pp. 12–17, 2004.
- [10] P. H. Holloway, J. Sebastian, T. Trotter, H. Swart, and R. O. Petersen, "Production and control of vacuum in field emission flat panel displays," *Solid State Technology*, vol. 38, no. 8, pp. 47–54, 1995.
- [11] J.-I. Han, M.-G. Kwak, Y.-K. Park, et al., "Experimental and theoretical considerations on evacuation of vacuum package for field emission display," *Journal of Vacuum Science & Technology B*, vol. 16, no. 3, pp. 1236–1238, 1998.
- [12] S. Itoh, T. Niiyama, and M. Yokoyama, "Influences of gases on the field emission," *Journal of Vacuum Science & Technology B*, vol. 11, no. 3, pp. 647–650, 1993.
- [13] S. Tominetti and M. Amiotti, "Getters for flat-panel displays," *Proceedings of the IEEE*, vol. 90, no. 4, pp. 540–558, 2002.
- [14] L. E. Shea, "Low-voltage cathodoluminescent phosphors," *Electrochemical Society Interface*, vol. 7, no. 2, pp. 24–27, 1998.
- [15] N. N. Chubun, A. G. Chakhovskoi, and C. E. Hunt, "Efficiency of cathodoluminescent phosphors for a field-emission light source application," *Journal of Vacuum Science & Technology B*, vol. 21, no. 4, pp. 1618–1621, 2003.
- [16] A. D. Dinsmore, D. S. Hsu, H. F. Gray, S. B. Qadri, Y. Tian, and B. R. Ratna, "Mn-doped ZnS nanoparticles as efficient low-voltage cathodoluminescent phosphors," *Applied Physics Letters*, vol. 75, no. 6, pp. 802–804, 1999.
- [17] R. N. Bhargava, D. Gallager, X. Hong, and A. Nurmikko, "Optical properties of manganese-doped nanocrystals of ZnS," *Physical Review Letters*, vol. 72, no. 3, pp. 416–419, 1994.
- [18] S. Shionoya and W. M. Yen, *Phosphors Handbook*, CRC Press, New York, NY, USA, 1998.
- [19] A. M. Srivastava and C. R. Ronda, "Phosphors," *Electrochemical Society Interface*, vol. 12, no. 2, pp. 48–51, 2003.
- [20] A. Vecht, D. W. Smith, S. S. Chadha, C. S. Gibbons, J. Koh, and D. Morton, "New electron excited light emitting materials," *Journal of Vacuum Science & Technology B*, vol. 12, no. 2, pp. 781–784, 1994.
- [21] J. Rodriguez-Viejo, K. F. Jensen, H. Mattoussi, J. Michel, B. O. Dabbousi, and M. G. Bawendi, "Cathodoluminescence and photoluminescence of highly luminescent CdSe/ZnS quantum dot composites," *Applied Physics Letters*, vol. 70, no. 16, pp. 2132–2134, 1997.
- [22] I. Brodie and C. A. Spindt, "Vacuum microelectronics," in *Advances in Electronics and Electron Physics*, P. Hawkes, Ed., vol. 83, pp. 2–106, Academic Press, New York, NY, USA, 1992.
- [23] A. G. Chakhovskoi, W. D. Kesling, J. T. Trujillo, and C. E. Hunt, "Phosphor selection constraints in application of gated field-emission microcathodes to flat panel displays," *Journal of Vacuum Science & Technology B*, vol. 12, no. 2, pp. 785–789, 1994.
- [24] C. E. Hunt and A. G. Chakhovskoi, "Phosphor challenge for field-emission flat-panel displays," *Journal of Vacuum Science & Technology B*, vol. 15, no. 2, pp. 516–519, 1997.
- [25] J. McKittrick, L. E. Shea, C. F. Bacalski, and E. J. Bosze, "The influence of processing parameters on luminescent oxides produced by combustion synthesis," *Displays*, vol. 19, no. 4, pp. 169–172, 1999.
- [26] X. Liu, C. Lin, and J. Lin, "White light emission from Eu^{3+} in CaIn_2O_4 host lattices," *Applied Physics Letters*, vol. 90, no. 8, Article ID 081904, 4 pages, 2007.
- [27] X. Liu and J. Lin, "Nanocrystalline $\text{LaGaO}_3 : \text{Tm}^{3+}$ as an efficient blue phosphor for field emission display with high color purity," *Applied Physics Letters*, vol. 90, Article ID 184108, 3 pages, 2007.
- [28] G. Wakefield, D. M. Williams, C. G. Harris, and P. J. Dobson, "Nanocrystalline phosphors for low voltage excitation applications," *Journal of the Society for Information Display*, vol. 31, no. 1, pp. 691–693, 2000.
- [29] F. Vetrone, J.-C. Boyer, and J. A. Capobianco, "Yttrium oxide nanocrystals: luminescent properties and applications," in *Encyclopedia of Nanoscience and Nanotechnology*, H. S. Nalwa, Ed., vol. 10, pp. 725–765, American Scientific, Stevenson Ranch, Calif, USA, 2004.
- [30] Y. L. Soo, S. W. Huang, Z. H. Ming, et al., "X-ray excited luminescence and local structures in Tb-doped Y_2O_3 nanocrystals," *Journal of Applied Physics*, vol. 83, no. 10, pp. 5404–5409, 1998.
- [31] D. Hreniak, W. Strek, P. Mazur, R. Pazik, and M. Zabkowska-Waclawek, "Luminescence properties of $\text{Tb}^{3+} : \text{Y}_3\text{Al}_5\text{O}_{12}$ nanocrystallites prepared by the sol-gel method," *Optical Materials*, vol. 26, no. 2, pp. 117–121, 2004.
- [32] W. Strek, D. Hreniak, G. Boulon, Y. Guyot, and R. Pązik, "Optical behavior of Eu^{3+} -doped BaTiO_3 nano-crystallites prepared by sol-gel method," *Optical Materials*, vol. 24, no. 1, pp. 15–22, 2003.
- [33] M. Zawadzki, D. Hreniak, J. Wrzyszczyk, et al., "Photoluminescence and cathodoluminescence of Tb-doped $\text{Al}_2\text{O}_3 - \text{ZrO}_2$ nanostructures obtained by sol-gel method," *Chemical Physics*, vol. 291, no. 3, pp. 275–285, 2003.
- [34] L. Kępiński, D. Hreniak, and W. Strek, "Microstructure and luminescence properties of nanocrystalline cerium silicates," *Journal of Alloys and Compounds*, vol. 341, no. 1-2, pp. 203–207, 2002.
- [35] W. Strek, E. Zych, and D. Hreniak, "Size effects on optical properties of $\text{Lu}_2\text{O}_3 : \text{Eu}^{3+}$ nanocrystallites," *Journal of Alloys and Compounds*, vol. 344, no. 1–2, pp. 332–336, 2002.
- [36] C. Xu, B. A. Watkins, R. E. Sievers, et al., "Submicron-sized spherical yttrium oxide based phosphors prepared by supercritical CO_2 -assisted aerosolization and pyrolysis," *Applied Physics Letters*, vol. 71, no. 12, pp. 1643–1645, 1997.
- [37] E. T. Goldburt and R. N. Bhargava, "Doped nanocrystalline phosphors for low voltage displays," in *Proceedings of the 9th International Vacuum Microelectronics Conference (IVMC '96)*, p. 637, St. Petersburg, Russia, July 1996.
- [38] J. S. Yoo and J. D. Lee, "The effects of particle size and surface recombination rate on the brightness of low-voltage phosphor," *Journal of Applied Physics*, vol. 81, no. 6, pp. 2810–2813, 1997.

- [39] E. Zych, J. Trojan-Piegza, L. Kępiński, D. Herniak, and W. Strek, "Synthesis of nanocrystalline powder phosphors and their possible applications," *Acta Universitatis Wratislaviensis*, pp. 277–291, 2004 (Polish).
- [40] P. Psuja, D. Hreniak, and W. Strek, "Rare-earth doped nanocrystalline phosphors for field emission display application," in *Proceedings of IEEE International Students and Young Scientists Workshop on Photonics and Microsystems*, pp. 50–54, Wrocław, Poland, June–July 2006.
- [41] H. D. Jang, C. M. Seong, H. K. Chang, and H. C. Kim, "Synthesis and characterization of indium-tin oxide (ITO) nanoparticles," *Current Applied Physics*, vol. 6, no. 6, pp. 1044–1047, 2006.
- [42] K. Y. Kim and S. B. Park, "Preparation and property control of nano-sized indium tin oxide particle," *Materials Chemistry and Physics*, vol. 86, no. 1, pp. 210–221, 2004.
- [43] J.-S. Lee and S.-C. Choi, "Solvent effect on synthesis of indium tin oxide nano-powders by a solvothermal process," *Journal of the European Ceramic Society*, vol. 25, no. 14, pp. 3307–3314, 2005.
- [44] F. Gu, S. F. Wang, M. K. Lü, et al., "Luminescent characteristics of Eu^{3+} in SnO_2 nanoparticles," *Optical Materials*, vol. 25, no. 1, pp. 59–64, 2004.
- [45] X. Fu, H. Zhang, S. Niu, and Q. Xin, "Synthesis and luminescent properties of $\text{SnO}_2 : \text{Eu}$ nanopowder via polyacrylamide gel method," *Journal of Solid State Chemistry*, vol. 178, no. 3, pp. 603–607, 2005.
- [46] H. Elhouichet, L. Othman, A. Moadhen, M. Oueslati, and J. A. Roger, "Enhanced photoluminescence of Tb^{3+} and Eu^{3+} induced by energy transfer from SnO_2 and Si nanocrystallites," *Materials Science and Engineering B*, vol. 105, no. 1–3, pp. 8–11, 2003.
- [47] M. Meyer, G. Onida, A. Ponchel, and L. Reining, "Electronic structure of stannous oxide," *Computational Materials Science*, vol. 10, no. 1–4, pp. 319–324, 1998.
- [48] N. Nadaud, N. Lequeux, M. Nanot, J. Jové, and T. Roisnel, "Structural studies of tin-doped indium oxide (ITO) and $\text{In}_4\text{Sn}_3\text{O}_{12}$," *Journal of Solid State Chemistry*, vol. 135, no. 1, pp. 140–148, 1998.
- [49] T. Omata, H. Fujiwara, S. Otsuka-Yao-Matsuo, and N. Ono, "Electron trapping center and SnO_2 -doping mechanism of indium tin oxide," *Applied Physics A*, vol. 71, no. 6, pp. 609–614, 2000.
- [50] P. Psuja, D. Hreniak, and W. Strek, "Low-voltage cathodoluminescent properties of $\text{Y}_3\text{Al}_5\text{O}_{12} : \text{Tb}^{3+}$ nanopowders," *Journal of Alloys and Compounds*, vol. 451, no. 1–2, pp. 571–574, 2008.
- [51] M. P. Pechini, "Method of preparing lead and alkaline earth titanates and niobates and coating method using the same to form a capacitor," US Patent no. 3330697, 1967.
- [52] D. Hreniak, W. Strek, and P. Mazur, "Preparation, spectroscopy and morphology of Nd:YAG nanostructures," *Materials Science*, vol. 20, no. 2, pp. 39–45, 2002.
- [53] B.-S. Jeon, J. S. Yoo, and J. D. Lee, "Electrophoretic deposition of ZnO:Zn phosphor for field emission display applications," *Journal of the Electrochemical Society*, vol. 143, no. 12, pp. 3923–3927, 1996.
- [54] S. W. Kang, J. S. Yoo, and J. D. Lee, "Photolithographic patterning of phosphor screens by electrophoretic deposition for field emission display application," *Journal of Vacuum Science & Technology B*, vol. 16, no. 5, pp. 2891–2893, 1998.
- [55] S. W. Kang, B. S. Jeon, J. S. Yoo, and J. D. Lee, "Optical characteristics of the phosphor screen in field-emission environments," *Journal of Vacuum Science & Technology B*, vol. 15, no. 2, pp. 520–523, 1997.
- [56] P. Psuja, W. Strek, and D. Hreniak, "Fabrication of a low-voltage light emitting device based on carbon nanotubes and rare-earth doped nanocrystals," in *Proceedings of the International Students and Young Scientists Workshop on Photonics and Microsystems*, pp. 65–67, Dresden, Germany, July 2005.
- [57] P. Psuja and W. Strek, "Cathodoluminescence measuring position with field emission cathode," in *Proceedings of the 4th Scientific Students Conference*, vol. 3, pp. 73–78, Wrocław, Poland, May 2006.
- [58] B. Cichy, P. Psuja, A. Górecka-Drzazga, J. A. Dziuban, and W. Strek, "A new concept of "Tuned" light sources for microfluidic application," in *Proceedings of the 19th International Vacuum Microelectronics Conference and the 50th International Field Emission Symposium (IVNC '06)*, pp. 419–420, Guilin, China, July 2006.
- [59] A. Górecka-Drzazga, B. Cichy, P. Psuja, S. Bargiel, J. A. Dziuban, and W. Strek, "Field emission light source for microfluidic devices," in *Proceedings of the 20th European Conference on Solid-State Transducers (Euroensors '06)*, pp. 42–43, Göteborg, Sweden, September 2006.
- [60] H. P. Christensen, D. R. Gabbe, and H. P. Jenssen, "Fluorescence lifetimes for neodymium-doped yttrium aluminum garnet and yttrium oxide powders," *Physical Review B*, vol. 25, no. 3, pp. 1467–1473, 1982.
- [61] R. S. Meltzer, S. P. Feofilov, B. Tissue, and H. B. Yuan, "Dependence of fluorescence lifetimes of $\text{Y}_2\text{O}_3 : \text{Eu}^{3+}$ nanoparticles on the surrounding medium," *Physical Review B*, vol. 60, no. 20, pp. R14012–R14015, 1999.
- [62] R. I. Zakharchenya, A. A. Kaplyanskii, A. B. Kulinkin, R. S. Meltzer, and S. P. Feofilov, "Radiative transitions and spectral-hole burning in $\text{MgO} : \text{Cr}^{3+}$ nanocrystals," *Physics of the Solid State*, vol. 45, no. 11, pp. 2209–2212, 2003.

Research Article

Multifunctional Composites Obtained by Incorporating Nanocrystals into Decorated PVK Polymers

Haizhu Sun,^{1,2} Junhu Zhang,¹ Ye Tian,² Yang Ning,¹ Hao Zhang,¹ Jie Ju,¹ Delong Li,¹ Shidong Xiang,¹ and Bai Yang¹

¹ State Key Lab for Supramolecular Structure and Materials, College of Chemistry, Jilin University, Changchun 130012, China

² College of Chemistry, Northeast Normal University, Changchun 130024, China

Received 28 March 2007; Accepted 4 October 2007

Recommended by Wieslaw Strek

Poly(vinylcarbazole) (PVK) was decorated with surfactant group to achieve amphiphilic polymer with luminescent property. The composition and properties of the polymers were systematically investigated using FTIR, EA, TGA, UV-Vis, and PL characterizations. Different CdTe nanocrystals (NCs) prepared in aqueous medium were directly transferred to organic phase using the PVK-based polymers. The quantum yield of NCs in the composites had been improved by 50% compared with their parent aqueous solution due to the short distance from carbazole moieties to NCs, which facilitated the Förster resonant energy transfer (FRET) between them. Moreover, efficient electron transfer at the interface of NCs and polymers had been confirmed which also indicated the application in photovoltaic cell for such composites.

Copyright © 2007 Haizhu Sun et al. This is an open access article distributed under the Creative Commons Attribution License, which permits unrestricted use, distribution, and reproduction in any medium, provided the original work is properly cited.

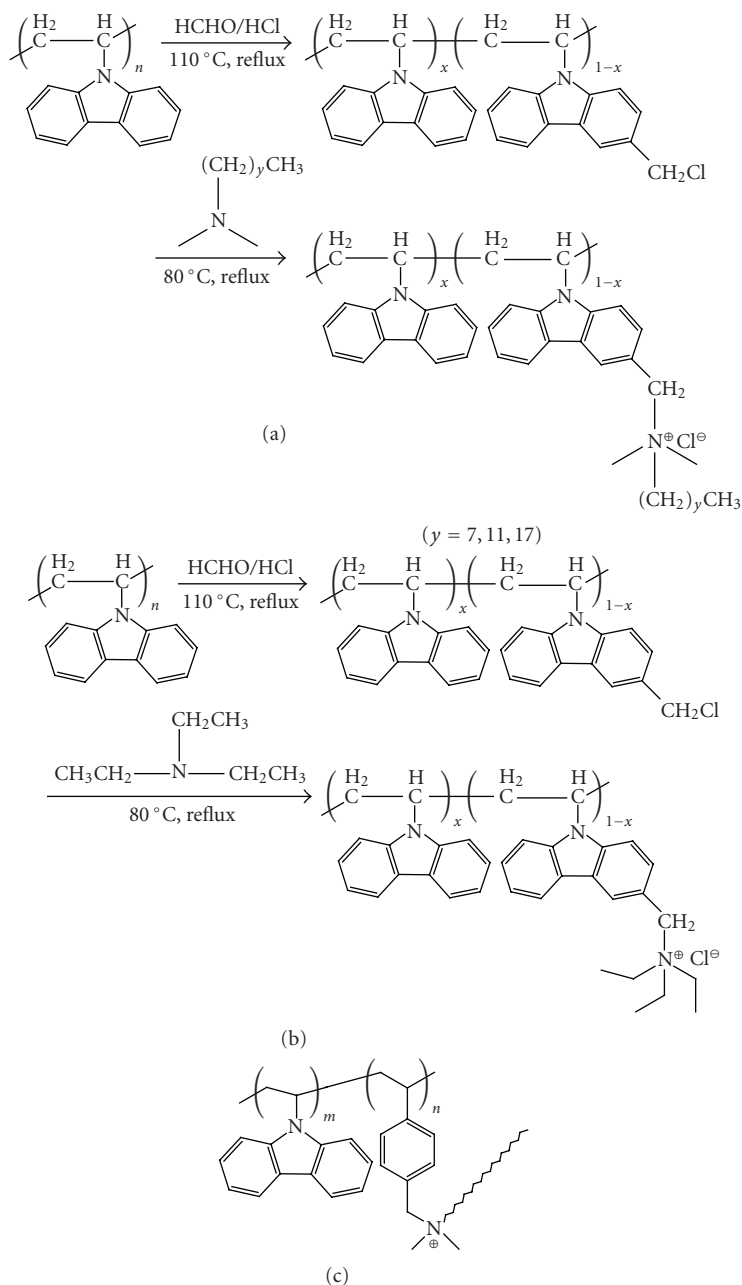
1. INTRODUCTION

Nowadays, a novel kind of luminescent polymers, namely, polymer with amphiphilic groups, has been extensively studied because such kind of polymers possesses several advantages. (1) They can offer particular properties compared with the normal neutral polymers due to their ionic side groups attached to the main chain. (2) Most amphiphilic polymers are typically soluble in water or alcohol, which are environment-friendly solvents. (3) Amphiphilic polymers are important building blocks for nanocrystal assembly via electrostatic interaction [1]. These advantages donate amphiphilic polymers with much more extensive applications; they can be used as the active layer in light-emitting diodes (LEDs) through layer-by-layer self-assembly method [2]; they are considered as highly sensitive materials in biological [3] and chemical sensors as well [4].

Semiconductor nanocrystals (NCs) directly synthesized in aqueous solution using water-soluble thio-compounds as ligands have intrigued much interests in recent years, because they are cheaper, less toxic, and biocompatible in comparison with the ones prepared in nonaqueous synthesis [5–8]. Many researchers pay attention to how to incorporate NCs into the polymers, because people expect that the resulted NC-polymer composites will combine the ad-

vantages of both NCs and polymers. Luminescent polymers with amphiphilic groups naturally become one of the best choices to realize this aim. In our recent work [9, 10], we have developed a novel method to incorporate NCs into functional amphiphilic polymers. First, we designed a novel amphiphilic copolymer of poly(9-vinylcarbazole-co-octadecyl-4-vinylbenzyl-dimethyl-ammonium chloride) (CPVKOVDAC) with blue fluorescence. Then, NCs in aqueous phase were transferred to organic phase using the polymers to achieve NC-polymer multifunctional composites. Moreover, this method provided a chance of incorporating several different color-emitting NCs into a functional polymer. Therefore, by incorporating two types of CdTe NCs having two distinct PL emissions at 524 and 650 nm into the polymer, white-light PL and electroluminescence (EL) have been obtained from the solution processable NC-polymer composite. However, the quantum yield (QY) of the composites was low and hence we could not get the EL devices with high efficiency.

In this paper, we directly grafted surfactant group on poly(vinylcarbazole) (PVK) (see Scheme 1) in order to achieve PVK-based amphiphilic polymer. Different CdTe NCs prepared in aqueous medium were directly transferred to the organic phase using the PVK-based polymers. Compared with the CPVKOVDAC copolymer which we used in



SCHEME 1: (a), (b) Synthesis route of PVK-N⁺ polymers. (c) The structure of CPVKOVDAC.

previous studies, the novel polymer had several advantages. It was (1) simple to characterize and had (2) better property of carrier transport. (3) The length of alkyl chains could be changed easily, which allowed us to investigate the effect of alkyl chain length on the PL properties of NCs. (4) The quantum yield of NCs had been improved by 50% due to the shorter distance between carbazole groups and NCs. The results of interaction between polymers and CdTe NCs indicated that the CdTe NC-PVK-based composites would possess good luminescent or photovoltaic properties just by varying the content of CdTe NCs in the composites.

2. EXPERIMENTAL

2.1. Materials

Poly(9-vinylcarbazole) (M_w 90 000) and tellurium powder (−200 mesh, 99.8%) were purchased from Sigma-Aldrich Chemical Corporation (Mo, USA). 3-Mercaptopropionic acid (MPA), thioglycolic acid (TGA), N, N-dimethyl octadecylamine, N, N-dimethyl dodecyl amine, N, N-dimethyl octyl amine, and 4-vinylbenzyl chloride were purchased from Acros Organics (UK). CdCl₂ (99+%), NaBH₄ (99%), and

triethylamine were commercially available products. All of the solvents had analytical grade and were used as received.

2.2. Synthesis of decorated PVK polymer

Concentrated hydrochloric acid (2.3 mL, 36.7%) and aqueous formaldehyde (1.25 mL, 30%) were added to a stirred solution (0–5°C) of PVK (1 g) in 1,4-dioxane (100 mL). The reaction mixture was allowed to warm to room temperature and was stirred for 1 hour. The reaction mixture was then heated to reflux for 4 hours. Cooling back to 80°C, tertiary amines were added to the reactant mixture and reacted for 4 hours. The mixtures were poured into a large amount of methanol to remove the unreacted small molecules, and the polymers were obtained by centrifugation. The polymer was dissolved in chloroform and precipitated in methanol several times to achieve pure decorated PVK polymer. Then, the product was kept at 40°C in vacuum overnight (FTIR (KBr): 2923, 2851 (ν , C–H stretch vibrations in octadecyl), 1624, 1595 (two aromatic vibrations in carbazole moieties), 1482, 1449 (vibrations in five-membered ring of carbazole), 1325, 1227 (ν , C–N stretch vibrations)).

2.3. Preparation of CdTe NC-PVK-based polymer composites

A series of aqueous solutions of CdTe nanocrystals capped with MPA or TGA was prepared according to previous reports [11]. The polymer was dissolved in chloroform at some concentration. The polymer solution was added to an aqueous CdTe solution (0.00125 N according to Cd^{2+}) with vigorous stirring. The organic phase was then separated to yield the CdTe NC-composite solution. The chloroform solvent was removed under reduced pressure and the resulting composite solids were kept in vacuum overnight. The composite solid can be dissolved again in chloroform for characterization.

2.4. Characterizations

FTIR spectra were recorded from a KBr window on a Nicolet AVATAR 360 FTIR spectrophotometer. UV-Vis spectra were acquired using a Shimadzu 3100 UV-Vis spectrophotometer. Fluorescence experiments were performed on a Shimadzu RF-5301 PC spectrofluorimeter. NETZSCH STA 449C thermogravimetric analyzer (TGA) with a heating rate of 10°C/min, up to 800°C, was used for the thermal degradation of the polymers under nitrogen. Element analysis was performed on Elementar Analysensysteme GmbH VarioEL. The quantum yields (QYs) of CdTe NC-polymer composites were determined using quinine sulfate (10^{-5} M in 0.5 mol/L H_2SO_4) as reference. The absorbance at the excitation wavelength was below 0.1 in order to avoid any significant reabsorption.

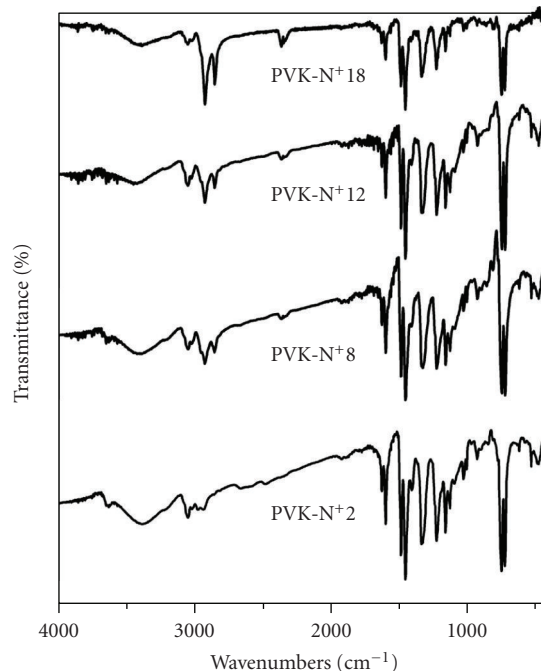


FIGURE 1: FTIR spectra of PVK-N⁺ polymers.

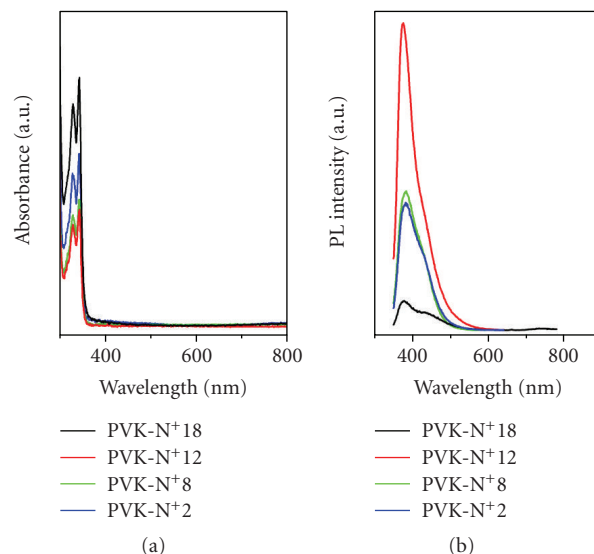


FIGURE 2: (a) UV-Vis absorption spectra and (b) PL spectra excited at 325 nm of the PVK-N⁺ polymers in chloroform.

3. RESULTS AND DISCUSSION

3.1. Synthesis and properties of PVK-based polymer

PVKs have been considered as potential polymer hosts for high-efficiency blue light-emitting diodes, and they found applications in photovoltaics, photoconductive materials, electroluminescence (EL) devices, photorefractive materials, nonlinear optical devices, and so forth [12–16]. It has been reported that chloromethylated PVK was functionalized with

TABLE 1: Basic information of the PVK-N⁺ polymers.

Abbreviations of the polymers	Tertiary amine used in the second step of the reaction	Numbers of quaternary amine decorated on the polymer chain per 100 carbazole moieties	Decomposition temperature (°C) (5% weight loss)
PVK-N ⁺ 18	N, N-dimethyl octadecylamine	25	215
PVK-N ⁺ 12	N, N-dimethyl dodecylamine	18	201
PVK-N ⁺ 8	N, N-dimethyl octylamine	21	211
PVK-N ⁺ 2	Triethylamine	15	209

Disperse Red 1 (DR-1) by Williamson ether synthesis [17]. Because of the higher reactivity of the carbazole ring toward electrophilic substitution, a serious cross-linking reaction occurred in preparation of chloromethylated PVK using chloromethyl methyl ether and zinc chloride, leading to the low content of chloromethyl in the soluble part of chloromethylated PVK. Consequently, further chromophoric functionalization was not easy to complete. In our studies, it was also found that the molecular weight, temperature of reaction, time of reflux, and so forth had an important influence on the resulted polymers. The formation of cross-linking polymers would occur if the experiment conditions were not well controlled. Scheme 1 gives the synthesis route of PVK-based polymer and Table 1 shows the basic information of the polymers. For a given molecular weight of PVK, for example, $M_w = 90\,000$, the concentration of PVK in 1, 4-dioxane should be controlled below 10 mg/mL. The temperature of reaction should be controlled at 80–110°C. Temperature below this will result in low degree of chloromethylation and low yield of PVK-based polymer at last. The reflux time must be shorter than 4 hours in the first step of the reaction in order to avoid the formation of cross-linking polymers. In the second step of the reaction, the tertiary amine probably reacts with surplus hydrochloric acid in the first step to form small quaternary amine molecules. Therefore, we added excessive tertiary amine to insure that there was enough tertiary amine to react with the chloromethylated PVK polymers. The PVK-based polymer was dissolved in chloroform and precipitated in methanol to delete the small quaternary amine molecules. Figure 1 shows the FTIR spectra of the PVK-based polymers. We can clearly observe strong C–H stretch vibration peaks at 2923 and 2851 cm^{-1} , which resulted from alkyl in the amine moieties. The peaks at 1624 and 1595 cm^{-1} are attributed to the two aromatic vibrations in carbazole moieties. The peaks at 1482 and 1449 cm^{-1} resulted from the five-membered ring of carbazole. The peaks at 1325 and 1227 cm^{-1} are attributed to C–N stretch vibration. These characteristic peaks have verified the formation of PVK-based polymers. The numbers of quaternary amine decorated on the polymer chain are also listed in Table 1, which are estimated from element analysis (see Table 2). The decomposition temperature of the polymers was about 200°C, which could satisfy the requirement of fabricating device using spin-coating method.

Figure 2 shows the UV-Vis absorption and PL spectra of the polymers. The electron transition within carbazole moieties leads to the peaks at 343 and 330 nm of absorption spectra. The peaks at 365 nm of PL spectrum are attributed to

TABLE 2: Element analysis of the PVK-N⁺ polymers.

	C (%)	H (%)	N (%)	Cl (%)
PVK-N ⁺ 18	82.415	7.415	6.291	1.640
PVK-N ⁺ 12	83.310	6.379	6.936	1.000
PVK-N ⁺ 8	83.145	6.352	7.074	1.600
PVK-N ⁺ 2	83.260	5.760	7.201	1.700

the high-energy excimer radiation of carbazole moieties. The UV-Vis and PL spectra indicate that the resultant polymers retain the photophysical properties of PVK.

3.2. Composite of semiconductor Nanocrystals and PVK-N⁺

The PVK-N⁺ polymers are readily soluble in common organic solvents such as chloroform, dichloromethane, N, N-dimethylformamide, and so forth. Different CdTe NCs as prepared in aqueous medium were directly transferred to the organic phase using the PVK-N⁺18 polymers to achieve composites 1–5, respectively (see Table 3). In this process, the electrostatic interaction between negatively charged CdTe NCs and positively charged moieties in polymers was the driving force for the formation of composite. Figures 3(a) and 3(b) show the UV-Vis absorption and PL spectra of the resultant composites 1–5 in chloroform. Absorption and PL spectra at different wavelengths correspond to distinct CdTe NCs, which confirms the presence of NCs in the polymer and the successful transfer of NCs from the aqueous phase to the organic phase. Furthermore, the full width at half maximum (FWHM) of PL peaks of the composite is similar to that of the parent NCs as prepared in aqueous medium, which indicates that the excellent properties of CdTe NCs were retained after they were capped with polymers. A clear solution of NCs in organic solvent strongly indicates a homogeneous distribution of NCs in the composites (see Figure 3(c)). The QYs of CdTe NCs in the composites 1–5 are 0.612, 0.476, 0.168, 0.368, and 0.146, respectively. For composites 1, 2, 3, and 5, the QYs are higher than their parent NC aqueous solutions. When we used polymer CPVKOVDAC to obtain NC composites, the QYs of CdTe NCs in the composites were always lower than parent NC aqueous solutions [9, 10]. The improvement of QY in this study is believed to be brought by the shorter distance from carbazole moieties to CdTe NCs in PVK-N⁺ system, which facilitates the Förster resonant energy transfer (FRET) between them.

TABLE 3: Component and quantum yields (QYs) of the composites.

Abbreviations of the composites	CdTe NCs used	QYs ^(b) of CdTe NCs in aqueous solution	QYs of CdTe NCs in the composites
Composite 1	TGA (530 nm) ^(a)	0.400	0.612
Composite 2	TGA (540 nm)	0.462	0.476
Composite 3	MPA (490 nm)	0.141	0.168
Composite 4	MPA (540 nm)	0.395	0.368
Composite 5	MPA (600 nm)	0.108	0.146

^(a) Reference to the CdTe NCs capping with TGA ligand and absorption of exciton at 530 nm. ^(b) Using quinine sulfate (10^{-5}) as PL reference.

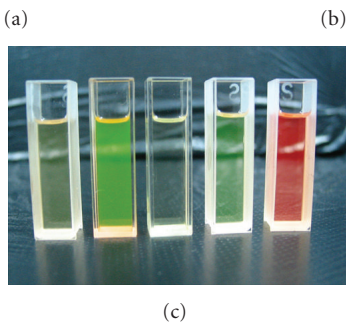
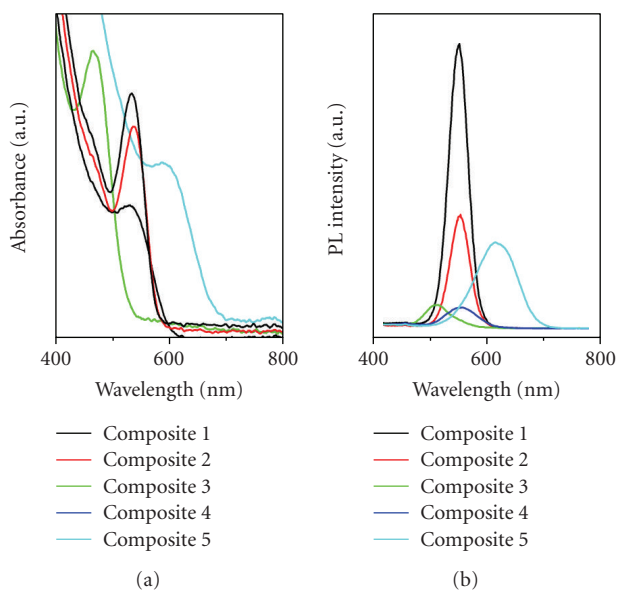


FIGURE 3: (a) UV-Vis absorption and (b) PL spectra excited at 400 nm of CdTe NC-polymer composites 1–5 in chloroform containing different CdTe NCs. (c) Photographs of composites 1–5 in chloroform.

3.3. Interaction between CdTe NCs and PVK-N⁺

Several methods have been developed to obtain the composites such as directly mixing the NCs into the polymers, in situ synthesis of NCs in polymer matrix, layer-by-layer assembly to achieve NC-polymer composite, and so forth [18–24]. Although some composites have been obtained using these methods, new problems also confronted chemists, such as aggregation of NCs in polymer matrix and PL quenching due to the different kinds of interaction between polymers and NCs. In our system, the process of composition of poly-

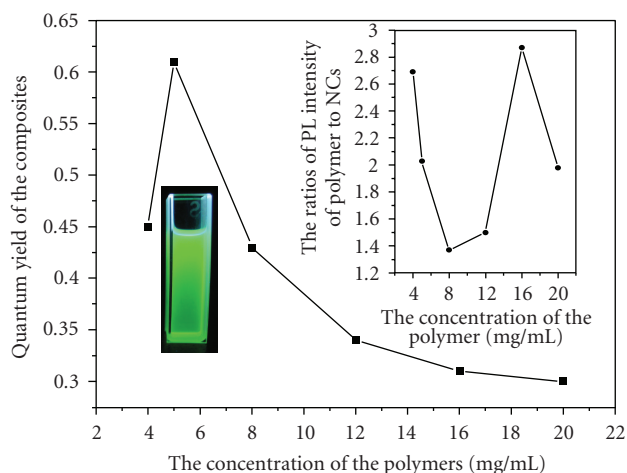


FIGURE 4: The curves of QYs versus concentration of polymer. Inset is the photograph of the composites with QY of 0.612, and the curves of the ratios of PL intensity of polymer to NCs versus concentration of polymer.

mer and CdTe NCs overcomes the major problems associated with the miscibility of NCs with polymer matrix and PL quenching of NCs in the polymer. However, we did find that the photophysical properties of NCs were influenced by the electrostatic interaction between polymers and NCs. Figure 4 shows that the QYs of the composites increase with increasing polymer concentration when the concentration of the polymer is below 5 mg/mL (the contents of CdTe were kept constant and the CdTe NCs were completely transferred from aqueous phase to organic phase). We conclude that the interaction between carbazole and CdTe NCs is mainly FRET whose energy is transferred by the excited carbazole moieties to CdTe NCs via dipole-dipole interaction at such concentrations. The highest QY was 0.612 when the concentration of the polymer was equal to 5 mg/mL. Inset of Figure 4 is the photo of the composite with the highest QY under UV illumination. The QY of CdTe NCs decreases with increasing polymer concentration when the concentration of the polymer is higher than 5 mg/mL. We suppose that electron transfer from carbazole moieties and CdTe NCs occurred, which quenched the PL of the resultant composites. For the PVK-N⁺ polymer, the PL intensity increases with increasing polymer concentration from 5 mg/mL to 20 mg/mL. However, from the inset curve of Figure 4, it can be observed that

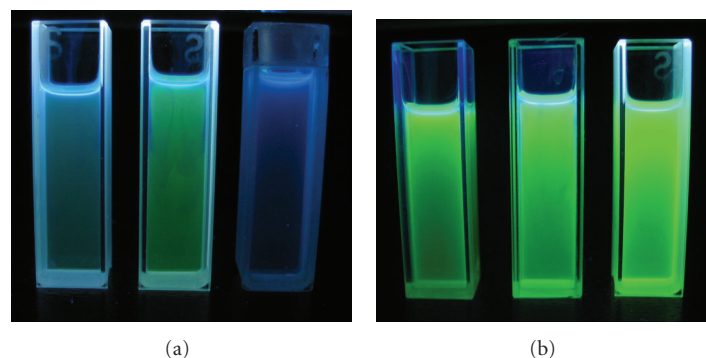


FIGURE 5: The photographs of (a) the composites with low-content CdTe NCs (the QYs of the NCs in the composite were 0.043, 0.107, and 0.061 from left to right) and (b) high-content CdTe NCs (the QYs of the NCs in the composite were 0.489, 0.571, and 0.612 from left to right). The photographs of (a) and (b) were taken under the same condition. The composites with low content of CdTe NCs refer to the composites obtained via 10 mL (5 mg/mL) PVK-N⁺ polymer solution adding 10, 20, 40 mL CdTe NC aqueous solutions, while the composites with high content of CdTe NCs refer to the composites obtained via 10 mL (5 mg/mL) PVK-N⁺ polymer solution adding 60, 80, 100 mL CdTe NC aqueous solutions.

the ratios of PL intensity of polymer to NCs decrease first and then increase when the polymer concentration increases continuously. These results indicate that the most efficient FRET occurred at the point at which the concentration of the polymer was about 8 mg/mL.

The tendency of PL changes of the composites became much more obvious when the concentration of the polymer was set constant, namely, 5 mg/mL, and the content of NCs was varied at some range. In CdTe NC aqueous solution, the QYs of the NCs increase with decreasing NC concentration because the self-quenching occurs at higher concentration. In the composite system, however, when the concentration of the polymer was about 5 mg/mL, the QYs of the NCs were higher in the composites with high content of CdTe NCs than those of the composites with low content of CdTe NCs. Figure 5 gives the photos of the composites with different contents of CdTe NCs under UV illumination. It can be clearly observed that the composites with low content of CdTe NCs show weak PL intensity (see Figure 5(a); the QYs of the NCs in the composite are 0.043, 0.107, 0.061 from left to right) while the ones with high content of CdTe NCs show strong PL intensity (see Figure 5(b); the QYs of the NCs in the composite are 0.489, 0.571, 0.612 from left to right). This phenomenon verifies the conclusion we have drawn above. We have ever systematically studied in our recent work [25] the mechanism of interaction between carbazole moieties and CdTe NCs. It is believed that the excited carbazole moieties could form carbazole anions and carbazole cations via resonance with carbazole moieties at the ground state under UV illumination. The carbazole anions migrated to the positively charged surface of CdTe NC-polymer composite and then shortened the distance between carbazole moieties and CdTe NCs. Carbazole anions donated their electrons to CdTe NCs, and then the donated electrons recombined with the holes in CdTe NCs. The result of electron transfer was that holes were confined to polymers while electrons were limited within CdTe NCs. The more the polymer was, the more positive net charges and carbazole moieties were. Therefore, the electron transfer became efficient with decreasing CdTe NCs.

4. CONCLUSION

In summary, we prepared a novel kind of PVK-based amphiphilic polymer with luminescent properties. CdTe NCs were directly transferred to the organic phase using the PVK-based polymers to achieve composites. The quantum yield of NCs had been improved by 50% compared with their parent aqueous solution due to the shorter distance from carbazole groups to NCs which facilitated the FRET between them. More efficient electron transfer at the interface of NCs and polymers was confirmed for composites by decreasing NC content. The results indicated that the composites could find applications in LEDs or photovoltaic devices.

ACKNOWLEDGMENTS

This work is financially supported by the Special Funds for Major State Basic Research Projects (Grant no. 2002CB613401), the National Natural Science Foundation of China (Grant no. 20534040), the Program for Changjiang Scholars and Innovative Research Team in University (Grant no. IRT0422), the Program of Introducing Talents of Discipline to Universities (Grant no. B06009), and Science Foundation for Young Teachers of Northeast Normal University (Grant no. 20070306).

REFERENCES

- [1] F. Huang, L. Hou, H. Wu, et al., "High-efficiency, environment-friendly electroluminescent polymers with stable high work function metal as a cathode: green- and yellow-emitting conjugated polyfluorene polyelectrolytes and their neutral precursors," *Journal of the American Chemical Society*, vol. 126, no. 31, pp. 9845–9853, 2004.
- [2] J. L. Casson, D. W. McBranch, J. M. Robinson, et al., "Reversal of interfacial dipole orientation in polyelectrolyte superlattices due to polycationic layers," *Journal of Physical Chemistry B*, vol. 104, no. 50, pp. 11996–12001, 2000.
- [3] K. Doré, S. Dubus, H.-A. Ho, et al., "Fluorescent polymeric transducer for the rapid, simple, and specific detection of

- nucleic acids at the zeptomole level,” *Journal of the American Chemical Society*, vol. 126, no. 13, pp. 4240–4244, 2004.
- [4] D. T. McQuade, A. E. Pullen, and T. M. Swager, “Conjugated polymer-based chemical sensors,” *Chemical Reviews*, vol. 100, no. 7, pp. 2537–2574, 2000.
- [5] M. Bruchez Jr., M. Moronne, P. Gin, S. Weiss, and A. P. Alivisatos, “Semiconductor nanocrystals as fluorescent biological labels,” *Science*, vol. 281, no. 5385, pp. 2013–2016, 1998.
- [6] W. C. W. Chan and S. Nie, “Quantum dot bioconjugates for ultrasensitive nonisotopic detection,” *Science*, vol. 281, no. 5385, pp. 2016–2018, 1998.
- [7] A. Schroedter, H. Weller, R. Eritja, W. E. Ford, and J. M. Wessels, “Biofunctionalization of silica-coated CdTe and gold nanocrystals,” *Nano Letters*, vol. 2, no. 12, pp. 1363–1367, 2002.
- [8] S. Wang, N. Mamedova, N. A. Kotov, W. Chen, and J. Studer, “Antigen/antibody immunocomplex from CdTe nanoparticle bioconjugates,” *Nano Letters*, vol. 2, no. 8, pp. 817–822, 2002.
- [9] H. Sun, J. Zhang, H. Zhang, et al., “Preparation of carbazole-containing amphiphilic copolymers: an efficient method for the incorporation of functional nanocrystals,” *Macromolecular Materials and Engineering*, vol. 291, no. 8, pp. 929–936, 2006.
- [10] H. Sun, J. Zhang, H. Zhang, et al., “Pure white-light emission of nanocrystal-polymer composites,” *ChemPhysChem*, vol. 7, no. 12, pp. 2492–2496, 2006.
- [11] H. Zhang, Z. Zhou, B. Yang, and M. Gao, “The influence of carboxyl groups on the photoluminescence of mercaptocarboxylic acid-stabilized CdTe nanoparticles,” *Journal of Physical Chemistry B*, vol. 107, no. 1, pp. 8–13, 2003.
- [12] A. van Dijken, J. J. A. M. Bastiaansen, N. M. M. Kiggen, et al., “Carbazole compounds as host materials for triplet emitters in organic light-emitting diodes: polymer hosts for high-efficiency light-emitting diodes,” *Journal of the American Chemical Society*, vol. 126, no. 24, pp. 7718–7727, 2004.
- [13] J. L. Kim, J. K. Kim, H. N. Cho, D. Y. Kim, C. Y. Kim, and S. I. Hong, “New polyquinoline copolymers: synthesis, optical, luminescent, and hole-blocking/electron-transporting properties,” *Macromolecules*, vol. 33, no. 16, pp. 5880–5885, 2000.
- [14] E. A. Plummer, A. van Dijken, H. W. Hofstraat, L. De Cola, and K. Brunner, “Electrophosphorescent devices based on cationic complexes: control of switch-on voltage and efficiency through modification of charge injection and charge transport,” *Advanced Functional Materials*, vol. 15, no. 2, pp. 281–289, 2005.
- [15] X. Gong, J. C. Ostrowski, D. Moses, G. C. Bazan, and A. J. Heeger, “Electrophosphorescence from a polymer guest-host system with an iridium complex as guest: forster energy transfer and charge trapping,” *Advanced Functional Materials*, vol. 13, no. 6, pp. 439–444, 2003.
- [16] J. G. Winiarz, L. Zhang, M. Lal, C. S. Friend, and P. N. Prasad, “Photogeneration, charge transport, and photoconductivity of a novel PVK/CdS-nanocrystal polymer composite,” *Chemical Physics*, vol. 245, no. 1–3, pp. 417–428, 1999.
- [17] J. Luo, J. Qin, H. Kang, and C. Ye, “A postfunctionalization strategy to develop PVK-based nonlinear optical polymers with a high density of chromophores and improved processibility,” *Chemistry of Materials*, vol. 13, no. 3, pp. 927–931, 2001.
- [18] B. O. Dabbousi, M. G. Bawendi, O. Onitsuka, and M. F. Rubner, “Electroluminescence from CdSe quantum-dot/polymer composites,” *Applied Physics Letters*, vol. 66, no. 11, pp. 1316–1318, 1995.
- [19] S. Wang, S. Yang, C. Yang, Z. Li, J. Wang, and W. Ge, “Poly(*N*-vinylcarbazole) (PVK) photoconductivity enhancement induced by doping with CdS nanocrystals through chemical hybridization,” *Journal of Physical Chemistry B*, vol. 104, no. 50, pp. 11853–11858, 2000.
- [20] M. Gao, C. Lesser, S. Kirstein, E. Möhwald, A. L. Rogach, and H. Weller, “Electroluminescence of different colors from polycation/CdTe nanocrystal self-assembled films,” *Journal of Applied Physics*, vol. 87, no. 5, pp. 2297–2302, 2000.
- [21] M. Gao, J. Sun, E. Dulkeith, N. Gaponik, U. Lemmer, and J. Feldmann, “Lateral patterning of CdTe nanocrystal films by the electric field directed layer-by-layer assembly method,” *Langmuir*, vol. 18, no. 10, pp. 4098–4102, 2002.
- [22] D. Wang, A. L. Rogach, and F. Caruso, “Semiconductor quantum dot-labeled microsphere bioconjugates prepared by stepwise self-assembly,” *Nano Letters*, vol. 2, no. 8, pp. 857–861, 2002.
- [23] T. Franzl, T. A. Klar, S. Schietinger, A. L. Rogach, and J. Feldmann, “Exciton recycling in graded gap nanocrystal structures,” *Nano Letters*, vol. 4, no. 9, pp. 1599–1603, 2004.
- [24] T. Franzl, A. Shavel, A. L. Rogach, et al., “High-rate unidirectional energy transfer in directly assembled CdTe nanocrystal bilayers,” *Small*, vol. 1, no. 4, pp. 392–395, 2005.
- [25] H. Sun, H. Zhang, J. Zhang, et al., “Effect of electrostatic interaction on the photophysical properties of the composites of CdTe nanocrystals and carbazole-containing polymers,” in preparation.

Review Article

Rare Earth-Activated Silica-Based Nanocomposites

C. Armellini,¹ A. Chiappini,¹ A. Chiasera,¹ M. Ferrari,¹ Y. Jestin,¹ M. Mortier,² E. Moser,³
R. Retoux,⁴ and G. C. Righini^{5,6}

¹ CSMFO group, CNR-IFN, Istituto di Fotonica e Nanotecnologie, via Sommarive, 14-38050 Povo, Trento, Italy

² Laboratoire de Chimie Appliquée de l'Etat Solide, Ecole Nationale Supérieure de Chimie de Paris (ENSCP),
UMR-CNRS 7574, 11 rue Pierre et Marie Curie, 75231 Paris, France

³ Dipartimento di Fisica, Università degli Studi di Trento, Gruppo CSMFO, Via Sommarive, 14-38100 Povo, Trento, Italy

⁴ Laboratoire CRISMAT, UMR 6508, ENSICAEN, 6 Boulevard du Maréchal Juin, 14050 Caen Cedex, France

⁵ CNR-IFAC, Istituto di Fisica Applicata, Nello Carrara, via Madonna del Piano, 10-50019 Sesto Fiorentino, Firenze, Italy

⁶ CNR, Dipartimento Materiali e Dispositivi, via dei Taurini 19, 00185 Roma, Italy

Received 3 August 2007; Accepted 23 November 2007

Recommended by Le Quoc Minh

Two different kinds of rare earth-activated glass-based nanocomposite photonic materials, which allow to tailor the spectroscopic properties of rare-earth ions: (i) Er³⁺-activated SiO₂-HfO₂ waveguide glass ceramic, and (ii) core-shell-like structures of Er³⁺-activated silica spheres obtained by a seed growth method, are presented.

Copyright © 2007 C. Armellini et al. This is an open access article distributed under the Creative Commons Attribution License, which permits unrestricted use, distribution, and reproduction in any medium, provided the original work is properly cited.

1. INTRODUCTION

The recent developments of nanocomposite materials activated by rare-earth ions have opened new possibilities in the field of both basic and applied physics, in a large area covering information communication technologies, health and biology, structural engineering, and environment monitoring systems. As far as luminescence properties are concerned, Er³⁺-activated nanocomposite glasses have become one of the key materials because of their relevance for to the development of optical amplifiers. The short-term goal is to develop appropriate material systems and devices to exploit, at the best, the luminescence properties of erbium with optimal optical properties of the host. The last decade has seen a remarkable increase in the experimental efforts to control and enhance emission properties of luminescent ions by tailoring the dielectric surrounding of the source [1–4]. With this aim, several approaches, using nanocomposite materials and/or specific geometries, such as planar interfaces, photonic crystals, solid state planar microcavities, dielectric nanospheres, and spherical microresonators, have been proposed.

The aim of this paper is to give an overview of the advances in glass-based photonic systems, where the nanoscale structures or the presence of nanostructured hosts induces an enhancement of optical and spectroscopic properties of the rare-earth ions. In particular, the following topics will

be highlighted: (i) rare earth-activated glass-ceramics planar waveguides, where the active ions are embedded in the crystalline phase, combining the mechanical and optical properties of the glass with a crystal-like environment for the rare-earth ions, and (ii) a procedure for the synthesizing of monosize silica spheres and the fabrication of core-shell-like structures of Er³⁺-activated silica spheres obtained by a seed growth method. Optical and spectroscopic assessment, as well as morphological and structural characterization of these systems, is reported.

2. TRANSPARENT GLASS-CERAMICS

Since the pioneer work in 1993, when Wang and Ohwaki discovered a novel glass-ceramic system characterized by a transparency comparable to glass [5], considerable efforts have been made in order to fabricate rare earth-activated glass-ceramic materials with active ions embedded in the crystalline phase [6]. The motivation for this research is combining the mechanical and optical properties of the glass with a crystal-like environment for the rare-earth ions, where their higher cross-sections can be exploited in order to fabricate more compact devices [4, 7]. Moreover, glass-ceramic materials may be a valid alternative method to control chemical parameters of the rare-earth ions, and thus may avoid undesirable effect like clustering as proposed by Auzel

and Goldner [8]. Thanks to the low phonon environment favourable to enhance the radiative rate and quantum efficiency, significant results have been achieved using oxyfluoride and fluoride transparent glass-ceramics activated by rare-earth ions, such as Er^{3+} , Eu^{3+} , Tm^{3+} , Nd^{3+} , and Pr^{3+} incorporated in fluoride nanocrystalline phases [9–14]. Using a top-down technique based on an appropriate thermal process of the glasses containing rare-earth fluorides, nanocrystals of $\beta\text{-PbF}_2$ were nucleated in the glassy matrix. Concerning telecom application, the paper by Hayashi et al. concerning Tm^{3+} ion-doped transparent oxyfluoride glass-ceramics containing PbF_2 nanocrystals around 20 nm in size, is of particular interest [15]. From spectroscopic measurements performed at low temperature, authors show the possibility of optical amplification in the S telecommunication band. Tikhomirov et al. have measured a bandwidth of about 90 nm for the ${}^4\text{I}_{13/2} \rightarrow {}^4\text{I}_{15/2}$ transition when Er^{3+} -activated oxyfluoride glass-ceramics were prepared with $\beta\text{-PbF}_2$ nanocrystals of about 2.5 nm in diameter [16].

Oxide-based glass-ceramics have been obtained both by conventional melting and by sol-gel route. Oishi et al. reported highly transparent glass ceramics obtained by heating, at 410–460°C, the $\text{K}_2\text{O-MgO-Nb}_2\text{O}_5\text{-TeO}_2$ glass precursor activated by Er^{3+} and Eu^{3+} ions [17]. It was demonstrated that the addition of Er^{3+} and Eu^{3+} ions was effective for the formation of the crystalline phase showing second harmonic generation, as well as enhancing the NIR-to-green upconversion, in the case of Er^{3+} -activated glass ceramics [17]. Attractive results have been obtained by sol-gel route. Kępiński and Wołczyr report on formation of nanocrystalline rare-earth silicates inside or at the surface of amorphous SiO_2 matrix upon heat treatment in air [18]. An intense room temperature photoluminescence at 1.531 μm is reported by Que et al. for erbium oxide nanocrystals dispersed in $\text{TiO}_2/\gamma\text{-glycidoxypropyltrimethoxysilane}$ (GLYMO) composite sol-gel thin films [19].

It should be mentioned that these nanocomposite systems are of particular interest for photonic application when the glass-ceramics can be prepared in waveguiding configuration. Concerning this, Strohhöfer et al., ten years ago, reported on active optical properties of Er-containing crystallites in sol-gel derived glass films [20]. Authors employed controlled heat treatment procedures to obtain a certain fraction of the rare-earth ions in crystallites. The active phases precipitated were $\text{Er}_2\text{Ti}_2\text{O}_7$ and ErPO_4 in $\text{SiO}_2\text{-TiO}_2$ -based sol-gel films. Doping of the glass matrix with Er^{3+} -containing crystallites improved the Er^{3+} fluorescence lifetime of the 1.55 μm transition, in some cases by more than 200%, unfortunately, no satisfactory waveguiding properties were achieved [20]. A pure $\text{Er}_2\text{Ti}_2\text{O}_7$ pyrochlore waveguiding structure was proposed by Langlet et al. with interesting spectroscopic properties because this compound has a much lower phonon energy than silica, which would permit to minimize nonradiative absorption mechanisms [21]. Recently, Jestin et al. have shown that $\text{SiO}_2\text{-HfO}_2\text{:Er}^{3+}$ glass-ceramic planar waveguides prepared by sol-gel route present valuable optical, spectroscopic, and structural features for successful applications in the telecommunication area [22–24].

2.1. Glass-ceramics fabrication and characterization

$(100-x)\text{SiO}_2\text{-}x\text{HfO}_2$ ($x = 10, 20, 30$ mol) planar waveguides, activated by 0.3 mol % Er^{3+} ions, were prepared by sol-gel route, using dip-coating deposition on $v\text{-SiO}_2$ substrates cleaned by ultrasound and alcohol [24]. Depending on their HfO_2 molar content ($x = 10, 20, 30$ mol), the waveguides discussed in this section are labeled W10, W20, and W30, respectively. The starting solution obtained by mixing tetraethylorthosilicate (TEOS), ethanol, deionized water, and hydrochloric acid as a catalyst was prehydrolyzed for one hour at 65°C. The molar ratio of $\text{TEOS} : \text{HCl} : \text{EtOH} : \text{H}_2\text{O}$ was 1 : 0.01 : 37.9 : 2. An ethanolic colloidal suspension was prepared using a precursor HfOCl_2 , and then added to the TEOS solution with an Si/Hf molar ratio of 90/10, 80/20, and 70/30. Erbium was added as $\text{Er}(\text{NO}_3)_3 \cdot 5 \text{H}_2\text{O}$ with an $\text{Er}/(\text{Si} + \text{Hf})$ molar concentration of 0.3 mol %. Erbium-activated silica-hafnia films were deposited on $v\text{-SiO}_2$ substrates by dip-coating with a dipping rate of 40 mm/min. Before further coating, each layer was annealed in air for 50 seconds at 900°C. Finally, the films, resulting of 30 coatings, were stabilized by a treatment in air and introduced directly in the furnace at 900°C (optimized temperature to fully densify the waveguides) for 5, 210 minutes, and 30 hours for the waveguides W30, W20, and W10, respectively. As a result of this procedure, transparent and crack-free waveguides were obtained. In order to nucleate nanocrystals inside the planar waveguide, an additional heat treatment was performed in air at a temperature of 1000°C for 30 minutes [22].

Specimens for high resolution transmission electron microscopy (HRTEM) observations were prepared by scraping off the thin films in ethanol using a diamond knife. A drop of the suspension is deposited and dried onto a carbon coated copper grid. A HRTEM study of the scraped samples was performed in a 200 kV side entry JEOL 2010 FEG by transmission electron microscope (TEM) fitted with a double-tilt sample holder (tilt $\pm 30^\circ$).

The losses at 1542 nm, for the TE_0 mode, were evaluated using the moving fiber method in which the exponential decay of light is measured by a fiber probe scanning down the length of the propagating steak [25]. The TE_0 mode waveguiding excitation was used for photoluminescence (PL) measurements. PL measurements in the region of the ${}^4\text{I}_{13/2} \rightarrow {}^4\text{I}_{15/2}$ transition and the decay curves from the ${}^4\text{I}_{13/2}$ level were obtained using the 514 nm line of a CW argon laser as an excitation source, and dispersing the luminescence light with a 320 mm single-grating monochromator with a resolution of 2 nm, with the experimental setup described elsewhere [22, 23, 26].

2.2. Glass-ceramics results and discussion

Nanostructured morphology of the sample W30, annealed at 1000°C for 30 minutes, was analyzed by means of HRTEM. The HRTEM images of a scrapped part of the film presented in Figures 1(a) and 1(b) show nanocrystals of about 4 nm to 6 nm in size, homogeneously dispersed in the amorphous matrix. Figure 1(b) evidences that each nanocrystal presents single domain features. The EDS analysis confirmed that

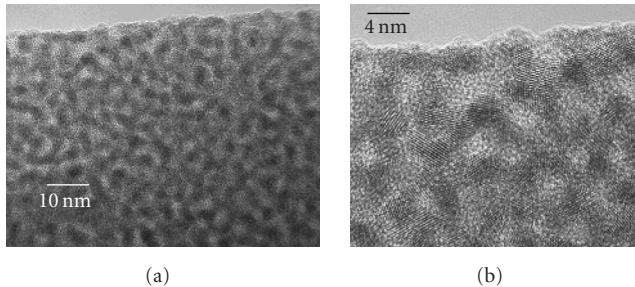


FIGURE 1: HRTEM image of the silica-hafnia W30 sample, annealed at 1000°C for 30 minutes, showing HfO₂ nanocrystals homogeneously dispersed in the amorphous matrix (a). Single domain nanocrystals are clearly evidenced in (b).

the nanocrystals and the surrounding amorphous matrix are composed of Hf oxide and Si oxide, respectively.

The glass-ceramic waveguides present a thickness of 1.3, 1.15, and 1 μm, and a refractive index close to 1.485, 1.538, and 1.597 measured at 1532 nm in the TE polarization for W10, W20, and W30, respectively. They are all a single mode at 1.5 μm, and the refractive index is highly dependent on the hafnium concentration. The losses of about 1 dB cm⁻¹ measured at 1542 nm, for this kind of glass-ceramics, make them suitable for operation in the C telecommunication band.

Figure 2 shows the normalized PL spectra for the glass-ceramic W10, W20, and W30 waveguides in the region of the ⁴I_{13/2} → ⁴I_{15/2} transition of Er³⁺ ions. The changes in the shape and bandwidth, with respect to the shape usually observed in the amorphous silica hafnia system (Figure 2(d)) [22, 26], indicate the significant modification of erbium ions environment in glass-ceramic systems. PL spectra show that Stark components are better resolved in the glass-ceramic, indicating that the Er³⁺ environment is more crystalline like. As the Er³⁺ local environment becomes ordered, it limits the inhomogeneous broadening typical of glassy environment, and therefore, the bandwidth narrows. The spectral width measured at 3 dB from the maximum intensity is 28, 19, 17 ± 1 nm for W10, W20, and W30 glass ceramic waveguides, respectively. Note that the bandwidth of the planar waveguide annealed at 900°C for 5 minutes, which is amorphous, is 51 ± 1 nm (see Figure 2(d)).

The decay curves of the luminescence from the ⁴I_{13/2} metastable state of Er³⁺ ions exhibit a single exponential profile for W20 and W30 glass-ceramics, and a double exponential profile for W10 sample. This nonsingle exponential profile is explained by the fact that not all erbium ions are feeling the same local environment. By fitting the decay curves with two different single exponential profiles, we can notice two different contributions: one corresponding to the erbium ions in the glass matrix leading to a lifetime close to 7.0 milliseconds, and the second part corresponding to erbium ions embedded in the crystalline environment leading to a lifetime close to 9 milliseconds. In the case of W20 and W30, as the decay profiles are single exponential, we can assume that all erbium ions are embedded in the crystalline environment. The decrease of the lifetime of Er in

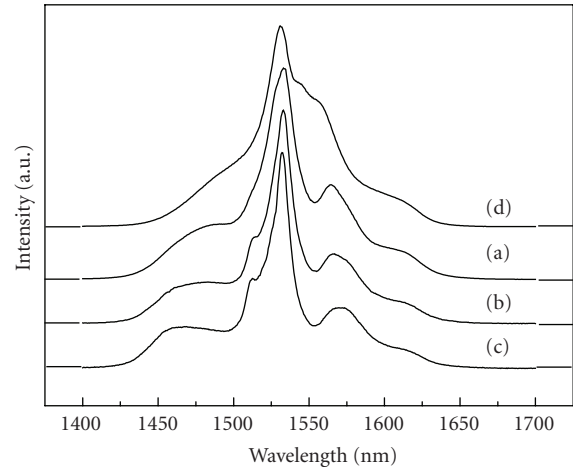


FIGURE 2: Room temperature luminescence spectra, obtained by exciting the TE₀ mode at 514.5 nm, of the ⁴I_{13/2} → ⁴I_{15/2} transition of Er³⁺ ion for the (a) W10, (b) W20, and (c) W30 planar waveguides annealed at 1000°C for 30 minutes. The emission spectrum of the W30 amorphous waveguide annealed at 900°C for 5 minutes is also reported for comparison (d).

crystals from 9 milliseconds to 8.7 and 7.2 milliseconds, as the HfO₂ content increases from 10% to 20% and to 30%, is attributed to an increase of the radiative electric dipole transition rate in a hafnia-dominated local field [24, 27]. The shortening of the lifetime with the increasing of HfO₂ content was already observed also for amorphous waveguides. Zampedri et al. have shown that in the case of (100-x)SiO₂-xHfO₂ waveguides (x = 10, 20, 30, 40 mol), the ⁴I_{13/2} lifetime decreases from 7.1 milliseconds to 5.5 milliseconds when the HfO₂ content increases from 10 mol % to 40 mol % [28]. They invoke the role of hafnia in increasing both distortion and crystal field strength around the Er³⁺ ion. However, this effect surely deserves further experimental investigation. Besides, computer simulation could be useful to take into account possible differences in the chemical environment of Er³⁺ ion for waveguides of different composition.

3. CORE-SHELL-LIKE STRUCTURES BY SOL-GEL-DERIVED ER³⁺-ACTIVATED SILICA NANOSPHERES

Monodisperse colloidal spheres in solution can be self-organized into an ordered structure if their size is adequate and their size polydispersity is low enough, yielding a periodic photonic bandgap structure or photonic crystal [29]. Furthermore, monodisperse colloidal spheres of predictable size and shape, activated with a controllable concentration of rare-earth ions like Er³⁺, have significant potential for use in optical devices such as microlasers, integrated optics structures, luminescent markers or nanosensors, and active photonic bandgap materials. In particular, in order to use rare-earth-activated colloids in photonic crystals, it is well known that the size polydispersity of the particles needs to be low and controllable.

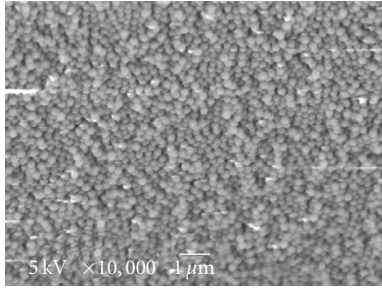


FIGURE 3: SEM images of the core-shell-like particles after seeded growth using the acid-based reaction.

3.1. Core-shell-like Er^{3+} -activated silica spheres fabrication and characterization

The core-shell-like Er^{3+} -activated silica spheres, where the core is the silica sphere and the shell is an Er_2O_3 - SiO_2 coating, were prepared using the following protocol: (i) the core was realized using the Stober method, discussed in detail in [30], and (ii) the shell was obtained by a seeded growth method [31]. Briefly, 150 mg of silica spheres of 270 nm diameter, obtained by the Stober method, were added to a solution with the molar ratio $\text{TEOS} : \text{CH}_3\text{COOH} : \text{H}_2\text{O}$ of 1 : 8 : 8, plus 0.2 wt% of ErCl_3 . The mixture was stirred for 45 minutes with a magnetic stirrer. After synthesis, the SiO_2 particles were separated from the solution by centrifuging at 1000 rpm and washed at least twice with pure ethanol. Subsequently, the core-shell-like Er^{3+} -activated silica spheres were heat treated at 950°C for 30 minutes [32].

The particle sizes were determined from electron micrographs taken with a scanning electron microscope, (SEM: JEOL-JSM 6300). The diameters of over a hundred particles were used in calculations of the average size and standard deviation δ of each sample. For photoluminescence spectroscopy on core-shell-like structures, the experimental setup described above for glass-ceramics was employed. The photoluminescence measurements were performed on pressed KBr pellets, containing 5% of doped silica spheres.

3.2. Core-shell-like Er^{3+} -activated silica spheres results and discussion

Figure 3 shows an SEM image of the core-shell-like Er^{3+} -activated silica spheres, obtained using a seeded growth method on the 270 nm monosize silica spheres. Figure 4 presents the PL spectra for the core-shell-like structure in the region of the ${}^4\text{I}_{13/2} \rightarrow {}^4\text{I}_{15/2}$ transition of Er^{3+} ions, obtained upon excitation at 980 nm.

The SEM image of Figure 3 demonstrates that seeded growth in the Er solution occurs on individual particles that do not collapse in higher-size clusters. PL measurements confirm the incorporation of Er^{3+} ions in the silica shell. In fact, the shape of the emission band in Figure 4 is typical of Er^{3+} -activated silica glasses with a main emission peak at 1533 nm [33] and a spectral bandwidth, measured at 3 dB from the maximum intensity of 27 ± 2 nm.

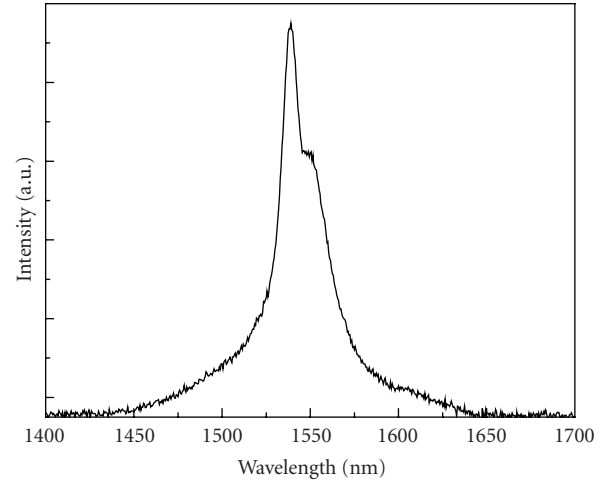


FIGURE 4: Room temperature photoluminescence spectra of the ${}^4\text{I}_{13/2} \rightarrow {}^4\text{I}_{15/2}$ transition of the Er^{3+} ions for the silica core-shell-like structure upon excitation at 980 nm.

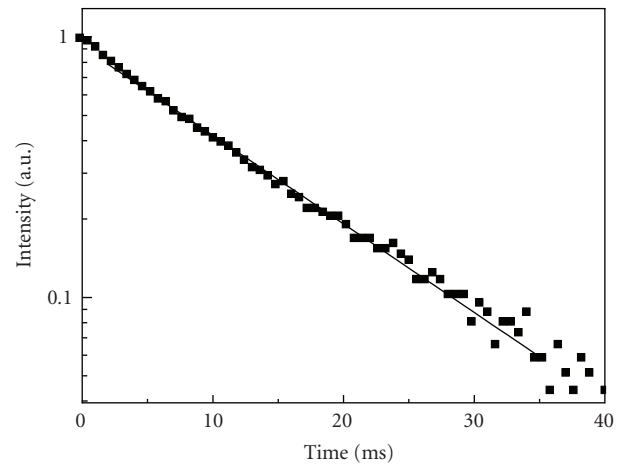


FIGURE 5: Room temperature luminescence decay curve from the ${}^4\text{I}_{13/2}$ state of Er^{3+} ions for the silica core-shell-like structure, upon excitation at 514.5 nm, after annealing for 30 minutes at 950°C .

The luminescence decay curve from the ${}^4\text{I}_{13/2}$ state of Er^{3+} ions for the silica core-shell-like structure, upon excitation at 514.5 nm, is reported in Figure 5. The decay profile exhibits a single exponential behavior with a lifetime of 12.8 ± 0.1 milliseconds. In order to give an estimation of the quantum efficiency η , defined by the ratio $\eta = \tau_{\text{meas}}/\tau_{\text{rad}}$, the measured lifetime (τ_{meas}) must be compared with the radiative lifetime τ_{rad} . Recently, many investigations were performed on SiO_2 spherical colloids doped with Er^{3+} ions in order to study the spontaneous emission and determine the local optical density of states in these systems [34, 35]. In these papers, Dood et al. determined a radiative lifetime of 18 ± 3 milliseconds for the ${}^4\text{I}_{13/2}$ state of Er^{3+} ions in pure silica. Note that this value is larger than the radiative lifetime reported for the ${}^4\text{I}_{13/2}$ state of Er^{3+} ions in silicate glasses [33]. Assuming a τ_{rad} of 18 milliseconds, a quantum efficiency η of 71% can be estimated for our core-shell spheres.

4. CONCLUSIONS

The paper presents some recent results in specific dielectric-based nanostructured and nanocomposite systems useful for the enhancement of Er^{3+} spectroscopic properties.

$\text{SiO}_2\text{-HfO}_2\text{:Er}^{3+}$ glass-ceramic planar waveguides were prepared by sol-gel route, with nanocrystals of about 4 nm to 6 nm in size, homogeneously dispersed in the amorphous matrix. These waveguides exhibit a single mode at $1.5\ \mu\text{m}$, their refractive index is highly dependent on the hafnium concentration, and the attenuation coefficient is about $1\ \text{dB cm}^{-1}$ at 1542 nm. The spectroscopic properties of Er^{3+} ions are determined by the crystalline local environment.

Seeded growth was successfully applied to synthesize core-shell-like Er^{3+} -activated silica spheres. Typical photoluminescence spectrum of erbium, with a lifetime of 12.8 milliseconds, was observed for the core-shell-like structure after annealing for 30 minutes at 950°C leading to a quantum efficiency of 71%.

ACKNOWLEDGMENTS

This research was partially supported by PAT (2004–2006) FAPVU and PAT (2007–2010) FaStFAL research projects. Part of this work has also been performed in the frame of the European forum on new glass applications (EFONGA) FP6 coordination action.

REFERENCES

- [1] P. Moriarty, "Nanostructured materials," *Reports on Progress in Physics*, vol. 64, pp. 297–381, 2001.
- [2] R. S. Meltzer, W. M. Yen, H. Zheng, et al., "Effect of the matrix on the radiative lifetimes of rare earth doped nanoparticles embedded in matrices," *Journal of Luminescence*, vol. 94-95, pp. 217–220, 2001.
- [3] R. S. Meltzer, S. P. Feofilov, B. Tissue, and H. B. Yuan, "Dependence of fluorescence lifetimes of $\text{Y}_2\text{O}_3\text{:Eu}^{3+}$ nanoparticles on the surrounding medium," *Physical Review B*, vol. 60, no. 20, pp. R14012–R14015, 1999.
- [4] M. Mortier and F. Auzel, "Rare-earth doped transparent glass-ceramics with high cross-sections," *Journal of Non-Crystalline Solids*, vol. 256-257, pp. 361–365, 1999.
- [5] Y. Wang and J. Ohwaki, "New transparent vitroceraamics codoped with Er^{3+} and Yb^{3+} for efficient frequency upconversion," *Applied Physics Letters*, vol. 63, no. 24, pp. 3268–3270, 1993.
- [6] M. C. Gonçalves, L. F. Santos, and R. M. Almeida, "Rare-earth-doped transparent glass ceramics," *Comptes Rendus Chimie*, vol. 5, no. 12, pp. 845–854, 2002.
- [7] M. Mortier, "Between glass and crystal: glass-ceramics, a new way for optical materials," *Philosophical Magazine B*, vol. 82, no. 6, pp. 745–753, 2002.
- [8] F. Auzel and P. Goldner, "Towards rare-earth clustering control in doped glasses," *Optical Materials*, vol. 16, no. 1-2, pp. 93–103, 2001.
- [9] V. K. Tikhomirov, V. D. Rodríguez, J. Méndez-Ramos, P. Núñez, and A. B. Seddon, "Comparative spectroscopy of $(\text{ErF}_3)(\text{PbF}_2)$ alloys and Er^{3+} -doped oxyfluoride glass-ceramics," *Optical Materials*, vol. 27, no. 3, pp. 543–547, 2004.
- [10] L. L. Kukkonen, I. M. Reaney, D. Furniss, M. G. Pellatt, and A. B. Seddon, "Nucleation and crystallisation of transparent, erbium III-doped, oxyfluoride glass-ceramics," *Journal of Non-Crystalline Solids*, vol. 290, no. 1, pp. 25–31, 2001.
- [11] M. Mattarelli, V. K. Tikhomirov, A. B. Seddon, et al., " Tm^{3+} -activated transparent oxy-fluoride glass-ceramics: structural and spectroscopic properties," *Journal of Non-Crystalline Solids*, vol. 345-346, pp. 354–358, 2004.
- [12] F. Liu, Y. Wang, D. Chen, and Y. Yu, "Investigation on crystallization kinetics and microstructure of novel transparent glass ceramics containing Nd:NaYF_4 nano-crystals," *Materials Science and Engineering B*, vol. 136, no. 2-3, pp. 106–110, 2007.
- [13] G. Dantelle, M. Mortier, D. Vivien, and G. Patriarche, "Influence of Ce^{3+} doping on the structure and luminescence of Er^{3+} -doped transparent glass-ceramics," *Optical Materials*, vol. 28, no. 6-7, pp. 638–642, 2006.
- [14] M. Mortier, A. Bensalah, G. Dantelle, G. Patriarche, and D. Vivien, "Rare-earth doped oxyfluoride glass-ceramics and fluoride ceramics: synthesis and optical properties," *Optical Materials*, vol. 29, no. 10, pp. 1263–1270, 2007.
- [15] H. Hayashi, S. Tanabe, and T. Hanada, "1.4 μm band emission properties of Tm^{3+} ions in transparent glass-ceramics containing PbF_2 nanocrystals for S-band amplifier," *Journal of Applied Physics*, vol. 89, no. 2, pp. 1041–1045, 2001.
- [16] V. K. Tikhomirov, D. Furniss, A. B. Seddon, et al., "Fabrication and characterization of nanoscale, Er^{3+} -doped, ultratransparent oxyfluoride glass-ceramics," *Applied Physics Letters*, vol. 81, no. 11, pp. 1937–1939, 2002.
- [17] H. Oishi, Y. Benino, and T. Komatsu, "Preparation and optical properties of transparent tellurite based glass-ceramics doped by Er^{3+} and Eu^{3+} ," *Physics and Chemistry of Glasses*, vol. 40, no. 4, pp. 212–218, 1999.
- [18] L. Kępiński and M. Wołczyr, "Nanocrystalline rare earth silicates: structure and properties," *Materials Chemistry and Physics*, vol. 81, no. 2-3, pp. 396–400, 2003.
- [19] Q. Que, Y. Zhou, Y. L. Lam, et al., "Photoluminescence of erbium oxide nanocrystals/ TiO_2/γ -glycidoxypropyltrimethoxysilane (GLYMO) composite sol-gel thin films derived at low temperature," *Journal of Applied Physics*, vol. 89, no. 5, pp. 3058–3060, 2001.
- [20] C. Strohhofer, J. Fick, H. C. Vasconcelos, and R. M. Almeida, "Active optical properties of Er-containing crystallites in sol-gel derived glass films," *Journal of Non-Crystalline Solids*, vol. 226, no. 1-2, pp. 182–191, 1998.
- [21] M. Langlet, C. Coutier, J. Fick, et al., "Sol-gel thin film deposition and characterization of a new optically active compound: $\text{Er}_2\text{Ti}_2\text{O}_7$," *Optical Materials*, vol. 16, no. 4, pp. 463–473, 2001.
- [22] Y. Jestin, N. Afify, C. Armellini, et al., " Er^{3+} activated silica-hafnia glass-ceramics planar waveguides," in *Integrated Optics, Silicon Photonics, and Photonic Integrated Circuits*, vol. 6183 of *Proceedings of SPIE*, pp. 1–8, Strasbourg, France, April 2006.
- [23] Y. Jestin, C. Arfuso-Duverger, C. Armellini, et al., "Cerimization of erbium activated planar waveguides by bottom up technique," in *Optical Components and Materials IV*, vol. 6469 of *Proceedings of SPIE*, pp. 1–9, San Jose, Calif, USA, January 2007.
- [24] Y. Jestin, C. Armellini, A. Chiappini, et al., "Erbium activated HfO_2 based glass-ceramics waveguides for photonics," *Journal of Non-Crystalline Solids*, vol. 353, no. 5–7, pp. 494–497, 2007.
- [25] Y. Okamura, S. Yoshinaka, and S. Yamamoto, "Measuring mode propagation losses of integrated optical waveguides: a simple method," *Applied Optics*, vol. 22, no. 23, pp. 3892–3894, 1983.

- [26] R. R. Gonçalves, G. Carturan, L. Zampedri, et al., "Sol-gel erbium-doped silica-hafnia planar and channel waveguides," in *Rare-Earth-Doped Materials and Devices VII*, vol. 4990 of *Proceedings of SPIE*, pp. 111–120, San Jose, Calif, USA, January 2003.
- [27] N. D. Afify, G. Dalba, C. Armellini, M. Ferrari, F. Rocca, and A. Kuzmin, "Local structure around Er^{3+} in SiO_2 - HfO_2 glassy waveguides using EXAFS," *Physical Review B*, vol. 76, Article ID 024114, 8 pages, 2007.
- [28] L. Zampedri, G. C. Righini, H. Portales, et al., "Sol-gel-derived Er-activated SiO_2 - HfO_2 planar waveguides for 1.5 μm application," *Journal of Non-Crystalline Solids*, vol. 345-346, pp. 580–584, 2004.
- [29] A. Chiappini, C. Armellini, S. N. B. Bhaktha, et al., "Fabrication and optical assessment of sol-gel-derived photonic bandgap dielectric structures," in *Photonic Crystal Materials and Devices III*, vol. 6182 of *Proceedings of SPIE*, pp. 1–10, Strasbourg, France, April 2006.
- [30] A. Chiappini, C. Armellini, A. Chiasera, et al., "Design of photonic structures by sol-gel-derived silica nanospheres," *Journal of Non-Crystalline Solids*, vol. 353, no. 5–7, pp. 674–678, 2007.
- [31] G. H. Bogush, M. A. Tracy, and C. F. Zukoski IV, "Preparation of monodisperse silica particles: control of size and mass fraction," *Journal of Non-Crystalline Solids*, vol. 104, no. 1, pp. 95–106, 1988.
- [32] M. J. A. de Dood, B. Berkhout, C. M. van Kats, A. Polman, and A. van Blaaderen, "Acid-based synthesis of monodisperse rare-earth-doped colloidal SiO_2 spheres," *Chemistry of Materials*, vol. 14, no. 7, pp. 2849–2853, 2002.
- [33] W. J. Miniscalco, "Erbium-doped glasses for fiber amplifiers at 1500 nm," *Journal of Lightwave Technology*, vol. 9, no. 2, pp. 234–250, 1991.
- [34] M. J. A. de Dood, L. H. Slooff, A. Polman, A. Moroz, and A. van Blaaderen, "Modified spontaneous emission in erbium-doped SiO_2 spherical colloids," *Applied Physics Letters*, vol. 79, no. 22, pp. 3585–3587, 2001.
- [35] M. J. A. de Dood, L. H. Slooff, A. Polman, A. Moroz, and A. van Blaaderen, "Local optical density of states in SiO_2 spherical microcavities: theory and experiment," *Physical Review A*, vol. 64, no. 3, Article ID 033807, 7 pages, 2001.

Review Article

Sol-Gel Processing of Nanostructured Inorganic Scintillating Materials

J. M. Nedelec

Laboratoire des Matériaux Inorganiques, CNRS UMR 6002, Université Blaise Pascal and ENSCCF, 24 Avenue des Landais, Aubière Cedex 63177, France

Received 30 April 2007; Accepted 4 October 2007

Recommended by Wieslaw Streck

The development of scintillating materials is believed to reach a new step by controlling their preparation on a nanometric level. Sol-Gel chemistry offers very unique tools for nanoscale mastering of the materials preparation. In particular, shaping of the materials as thin films or nanoparticles offers new application in medical imaging. The control of doping ions dispersion thanks to soft chemistry is also a great advantage of such synthetic routes. In this paper, we will review recent work devoted to the sol-gel preparation of inorganic scintillating materials. We will focus on the new possibilities and advantages offered by sol-gel chemistry for the preparation of new scintillators and improvement of existing ones.

Copyright © 2007 J. M. Nedelec. This is an open access article distributed under the Creative Commons Attribution License, which permits unrestricted use, distribution, and reproduction in any medium, provided the original work is properly cited.

1. INTRODUCTION

Since the discovery of X-ray by Röntgen and the concomitant use of the first scintillator, research directed towards materials that can convert high-energy radiations (X-rays, γ -rays, neutrons) into UV-visible light, easily detectable with conventional detectors, is in constant development [1–7]. These materials spread over various applications such as medical imaging, high energy physics, and nondestructive testing (airport security, industrial control, etc.).

During the past twenty years, numerous materials have been proposed to be used as scintillators. Among them, a lot of oxides materials have successfully been developed up to industrial applications. In order to provide efficient scintillators for X or γ rays, the choice of the oxide matrix is crucial. Since the first step of the scintillation mechanism involves absorption of high-energy photon (from a few KeV to several MeV), photoelectrical effect has to be favored. To do so, materials with high $\rho \cdot Z_{\text{eff}}^4$ are required. In this formulation, ρ is the density of the material and Z_{eff} is the effective atomic number defined as [8]

$$Z_{\text{eff}}^4 = \sum_i w_i Z_i^4, \quad (1)$$

where w_i is the mass fraction of atom i and Z_i is its atomic number. More recently, research focused more on improving the performances of known scintillators rather than de-

veloping new materials. It appears that a good way to improve scintillators is to get a control of the material on a nanometric scale. It is indeed very important to control the dispersion of doping ions in the matrix and to control the size of the grains in case of powders. The possibility to prepare nanocrystals could allow the preparation of transparent ceramics that could replace advantageously single crystals. Another very attractive solution is the direct preparation of scintillating thin films. Thin scintillating films are particularly valuable in fundamental spectroscopic studies when the absorption coefficient of the material is high or when the excitation energy is close to the absorption edge. They are also very interesting for high-resolution imaging where the scintillator is required as a homogeneous coating. Both solutions provide low-cost substitutions for single crystals. The use of sol-gel processes for the preparation of scintillating materials seems to be a very interesting way to reach these objectives. In effect, the use of molecular precursors is the guarantee of very high chemical homogeneity which is usually also observed in the final material. Furthermore, the high versatility of the sol-gel process allows to reach various compositions and to vary the nature and the concentration of the doping ion easily. This cannot be usually done for single crystal growth. Even if sol-gel chemistry appears to be a valuable way to prepare new scintillators and scintillators with enhanced properties, not so many works propose such an approach. This paper tries to summarize the state-of-the-art on sol-gel processing

of scintillating materials and in particular scintillating thin films. Only crystalline materials will be considered, obviously sol-gel process is also very valuable for amorphous materials like glasses and hybrid materials incorporating organic molecules. Because this point will not be developed in the following, we would like to list the main tendencies.

Sol-Gel chemistry has been initially developed as an alternative route to glasses. Sol-Gel derived glasses in particular doped with Ce^{3+} ions have been considered as scintillating materials; see for instance work from Chiodini et al. [9, 10] or Nogues et al. [11] and references therein. Another interesting possibility is offered by the intrinsic porosity of sol-gel-derived glasses. In this case, the porous glass or gel can be used as a host for active species. If the guest species is organic, the resulting material is an inorganic-organic hybrid material. Depending on the interaction between the two components, class I and class II hybrids can be found [12]. Molecules classically used in liquid scintillators can be embedded in the silica framework [13] and in the case of PPO and POPOP the active molecules can be covalently grafted to the silica network [14]. An important axis concerns the development of cationic complexes mainly of rare-earth ions and their incorporation in inorganic sol-gel-derived networks. A lot of work can be found in the literature including the incorporation of various rare-earth complexes [15], covalently grafted or not and including recently cryptates [16] and podates [17].

2. SOL-GEL PROCESSING OF MATERIALS

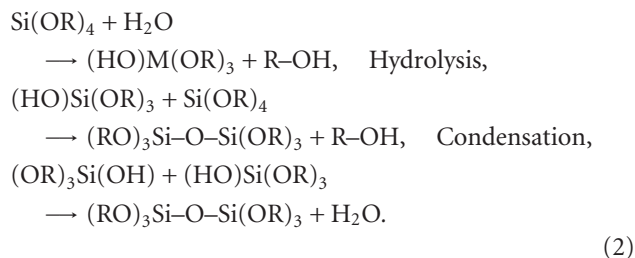
Numerous excellent reviews can be found in the literature concerning the sol-gel processing of materials. In this section, we would like to summarize the main features and to underline the major advantages in the view of producing scintillators.

During the last 30 years, sol-gel processes have been widely used for the preparation of glasses and ceramics. Usually, starting with molecular precursors like alkoxides or acetates, the sol-gel process takes place in solution. This provides definitive homogeneity for multicomponent systems. In the particular case of doping, the sol-gel process provides an ideal way to control the level and the homogeneity of doping. For luminescent materials, this is crucial since the light emission is usually due to doping ions like rare-earth or transition metals ions. Quenching concentrations are usually found higher for sol-gel-derived materials because of better dispersion of doping ions and thus higher average distance between emitting centers. Several authors have also developed heterometallic precursors associating different elements through chemical bonding and thus providing the highest homogeneity [18, 19]. As far as alkoxides chemistry is concerned, it is useful to distinguish the case of silicon alkoxides (Si being a semimetal) and the case of metal alkoxides.

2.1. Silicon alkoxides

The sol-gel process involving silicon alkoxide can be described in two steps, the hydrolysis of the alkoxide and its polycondensation. For a given alkoxide of general formula

$Si(OR)_4$, R being an alkyl chain, these reactions can be written as follows:



Usually, silicon alkoxides are very stable against hydrolysis. Step 1 thus requires catalysis usually performed by using acids or bases. Excellent review can be found in [20]. Briefly, base-catalyzed hydrolysis occurs through an S_N2 mechanism involving a 5-fold coordinated silicon atom. On the other hand, acid catalysis proceeds through a limiting step corresponding to the protonation of an oxygen atom resulting in an S_N1 mechanism. Acidic catalysis leads to a much quicker hydrolysis than basic catalysis resulting in different final structures for the gels networks.

2.2. Metal alkoxides

Contrary to silicon alkoxides, metal alkoxides react very quickly with water in absence of catalysts. In particular, transition metal alkoxides are very reactive because of the presence of highly electronegative OR groups that stabilize the central atom in its highest oxidation state. This in turn makes the metal atom very susceptible to nucleophilic attack. An excellent review presents the chemical reactivity of metal alkoxides [21]. Recently, some controversy appeared with respect to the well-acknowledged mechanism of hydrolysis condensation of metal alkoxides [22] supported for instance by the recently demonstrated impossibility of S_N2 mechanism [23] classically invoked to explain the higher reactivity of metal alkoxides.

In any case, both for silicon and metal alkoxides, the ongoing polycondensation process leads to the formation of a 3D network. The point where this network extends throughout the reactor is described by the percolation theory and named the gel point. The obtained wet gel can be dried in various conditions leading a xerogel with residual porosity. Further heating of the xerogel in controlled conditions allows obtaining the desired glass or ceramic.

Before the gel point, the colloidal solution can be stabilized and used directly to coat various substrates by classical techniques like dip coating, spin coating, laminar induction or spray. This provides a low cost and efficient way to produce nanometric thin films with good homogeneity.

Furthermore, the temperatures required for the full densification and crystallization of the desired glass/ceramic are usually lower than the ones required by classical melting or solid-state processes. This can be interesting from an economical point of view but also because in some cases, the obtained phases can differ from the one obtained by classical procedures. By this way, new phases can be obtained or high-temperature phases can be stabilized at room temperature. In the following sections, we will propose an exhaustive

overview of literature works specifically aiming the developments of scintillating materials by sol-gel chemistry.

3. YTTRIUM AND RARE-EARTH SESQUIOXIDES

Yttrium, lutecium, and gadolinium sesquioxides have been acknowledged as efficient scintillating materials when activated with rare-earth ions.

In 2003, Montes et al. proposed a new sol-gel route to Nd^{3+} doped Y_2O_3 thin films [24]. Authors have used Yttrium and Neodymium nitrates together with coconut water to prepare the sol that has been deposited by dip coating on glass substrates. After annealing at 500°C , the films are crystallized with crystallite size ranging between 17 and 23 nm depending on the densification conditions. The radioluminescence of the films is observed but not quantified.

Gd_2O_3 powders and thin films have been prepared by García-Murillo et al. in 2001 [25] and later by Guo et al. [26]. In the first reference, the authors used gadolinium isopropoxide $\text{Gd}(\text{iOPr})_3$ as precursor and acetylacetonate as chelating agent to control hydrolysis/condensation of the very reactive alkoxide. Thin films of good optical quality have been obtained by multistep dip-coating operation on various amorphous substrates. In the second reference, the authors used gadolinium acetate as precursor and diethylenetriamine as complexant. García-Murillo et al. paid particular attention to the material formation by using several complementary techniques like TEM, Raman, and m-lines spectroscopies. Raman spectroscopy performed in the waveguiding configuration [27] allowed a detailed study of crystallization of Gd_2O_3 thin films. The films begin to crystallize around 650°C in the cubic phase and transform partially to the monoclinic phase above 800°C [28].

For scintillation purpose, Eu^{3+} doped films (5%) have been prepared by the same group [29]. Emission spectra were dominated by europium $^5\text{D}_0$ to $^7\text{F}_2$ transition around 611 nm and in agreement with the cubic structure of the gadolinium oxide. Under X-ray excitation, the films showed intense emission (Figure 1) estimated by comparison with $\text{NaI}(\text{Tl})$ with the photopeak method [30]. Light yield of 18500 photons/MeV was found with an afterglow of 0.1% after 10 milliseconds which remains too high for medical imaging.

Due to its high atomic number, lutecium containing materials have been widely considered for scintillation application. Complex oxides will be described in the following section. Lutecium sesquioxide Lu_2O_3 is isostructural to Gd_2O_3 but presents a much higher density ($8.4 \text{ g}\cdot\text{cm}^{-3}$ instead of $7.1 \text{ g}\cdot\text{cm}^{-3}$). Starting from Lutecium 2,4 pentanedionate in isopropanol, García-Murillo et al. prepared Lu_2O_3 powders and thin films by dip coating [31]. The reported work and results are indeed very similar to the ones reported for Gd_2O_3 . Activation of Lu_2O_3 thin films with Eu^{3+} ions results in good scintillation performances (Figure 1), 19750 photons per MeV under X-ray excitation but still an afterglow of about 0.1% after 10 milliseconds. Codoping with Tb^{3+} ions for instance can reduce this afterglow.

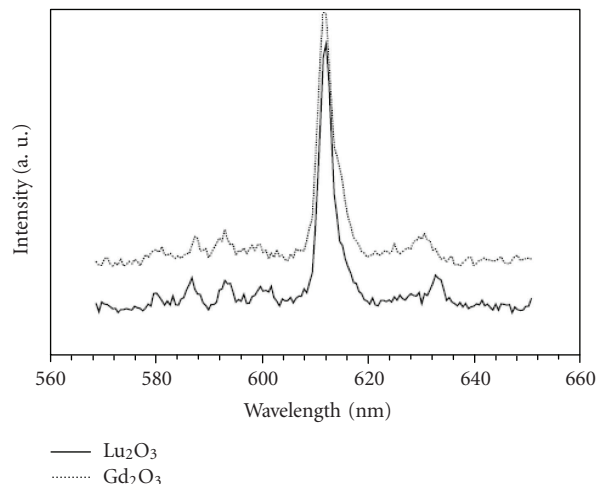


FIGURE 1: Emission of $\text{Gd}_2\text{O}_3 : \text{Eu}^{3+}$ 5% and $\text{Lu}_2\text{O}_3 : \text{Eu}^{3+}$ 5% thin films under X-ray excitation, reproduced from [15] © 2002 with permission from Elsevier.

4. LUTECIUM OXIDES

As stated above, lutecium oxides have received considerable interest to be used as host matrices for scintillators applications. Lutecium oxides are obviously very dense materials and rare-earth substitution can easily be performed in these materials. Among all rare-earth ions, Ce^{3+} occupy a specific situation because of its electronic scheme and the subsequent allowed 5d-4f transitions lying in the UV-visible range (300–500 nm). These transitions are also very fast (20–60 nanoseconds) and very intense.

4.1. Silicates

Cerium-doped lutecium oxyorthosilicate Lu_2SiO_5 is actually used in the detection system of PET scanners. In 2000, Bescher et al. proposed the first sol-gel route to lutecium containing scintillator [32]. At this time, the inorganic phase was not clearly identified and embedded in an amorphous SiO_2 matrix. A few years later, Mansuy et al. proposed the first reported preparation of Lu_2SiO_5 (LSO) by sol-gel chemistry [33]. Due to the very high reactivity and cost of rare earth alkoxides, the authors proposed the in situ preparation of $\text{Lu}(\text{iOPr})_3$ by metathesis reaction between Lutecium chloride and potassium alcolate. TEOS was used as the silicon precursor. Doping was achieved through the same procedure starting with europium, terbium, or cerium nitrates. The obtained multicomponent sol was stable and could be used to prepare thin films or destabilized to yield powders. Single phase materials were obtained and high scintillation efficiency under X-ray was measured (20 000 photons/MeV). Following this first paper, the same authors proposed a detailed study of rare-earth substitution in LSO using Eu^{3+} ion as a structural probe [34]. Combining X-ray absorption and luminescence spectroscopies, a clear preferential substitution on one of the two Lu sites has been evidenced. This behaviour was already described for Ce^{3+} but the attribution of the sites

was clearly wrong. This is a very nice example of the interest of the sol-gel process both from an applicative point of view (low-cost efficient alternative to single crystals preparation) and from the fundamental point of view (first preparation of Eu^{3+} doped LSO and detailed study of substitution).

Mansuy et al. also evidenced the sol-gel formation of lutecium pyrosilicate $\text{Lu}_2\text{Si}_2\text{O}_7$ [35]. This material has been recently studied for scintillation application and acknowledged as very interesting candidate in particular for medical imaging applications [36, 37].

4.2. Borates

Lutecium orthoborate LuBO_3 is also a good candidate for scintillation applications. Boyer et al. reported the first sol-gel elaboration of LuBO_3 thin films [38]. Using Boron triisopropoxide and Lutecium isopropoxide, the authors prepared amorphous powders and thin films that could be transformed into vaterite LuBO_3 around 700°C . In this first work, only Eu^{3+} doping was considered and was achieved for a single doping concentration. Using the same procedure, Mansuy et al. proposed a systematic study of scintillation properties of LuBO_3 powders and thin films doped with Eu^{3+} , Tb^{3+} , and Ce^{3+} ions with various concentrations.

Ce^{3+} doped LuBO_3 powders showed maximum scintillation yield for 0.5% doping concentration corresponding to a light yield under X-ray of about 8100 photons/MeV equivalent to commercial $\text{Bi}_4\text{Ge}_3\text{O}_{12}$ scintillator [39]. The afterglow was low, 0.2% after 1 second. For Eu^{3+} and Tb^{3+} doping, maximum emission under X-rays was observed for $\text{LuBO}_3 : \text{Eu}^{3+}$ 5% and $\text{LuBO}_3 : \text{Tb}^{3+}$ 5% with light output of 8900 and 4400 photons/MeV, respectively [40].

The evolution of the relative scintillation yield as a function of the doping level is displayed in Figure 2 for $\text{LuBO}_3 : \text{Eu}$, Tb , Ce . The rare-earth-doped LuBO_3 thin films were thoroughly characterized by XPS and RBS techniques demonstrating the good homogeneity of the coatings and an inter diffusion process between the layer and the substrate [41]. Scintillation was clearly evidenced but not quantified because of the inherent difficulty to get quantitative light yield for thin films.

4.3. Aluminates

Lutecium-aluminium garnet, $\text{Lu}_3\text{Al}_5\text{O}_{12}$, has been the subject of various works. Activated with Ce^{3+} ions, it turned to be a very promising scintillating material. Recently, Min et al. proposed a Pechini sol-gel route to Tb^{3+} doped LuAG films [42]. Combining Pechini method and dip coating, LuAG films doped with various concentrations of Tb^{3+} ions were coated onto silicon substrates. Crystalization begins around 900°C and the luminescence properties have been reported but not under high-energy excitation. Liu et al. reported in 2007 the preparation of nanosized cerium-doped LuAG phosphors by a sol-gel combustion process [43]. Aluminium, cerium, and lutecium nitrates were mixed in required proportions together with glycine (fuel). Upon stirring at 60°C , a gel is formed. This gel was then heated at 180°C where an autocombustion process took place. After annealing the final

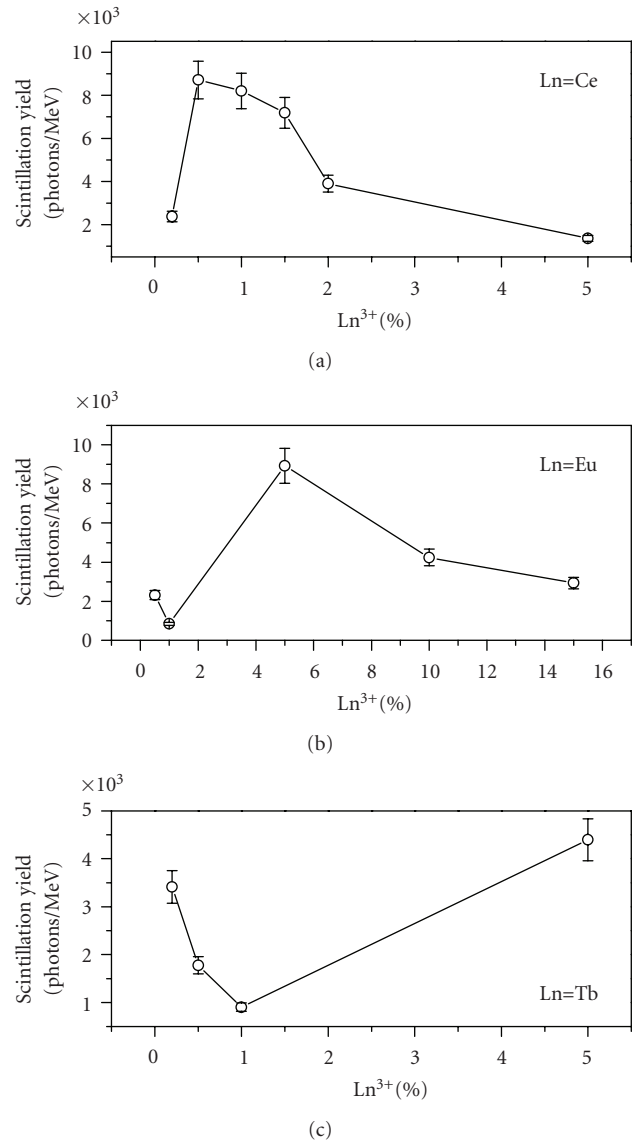


FIGURE 2: Scintillation yield under X-ray excitation for $\text{LuBO}_3 : \text{Ln}^{3+}$ ($\text{Ln} = \text{Ce}, \text{Eu}, \text{Tb}$) as a function of rare-earth concentration.

solid at $800\text{--}1000^\circ\text{C}$, the garnet phase is obtained. The radioluminescence was observed but not quantified.

4.4. Phosphates

Lutecium orthophosphate LuPO_4 is known as an efficient scintillator [44–47]. First, all-alkoxide sol-gel route to orthophosphate was described in 2002 [48]. In this procedure, phosphorous and rare-earth or yttrium oxides are formed in situ by reacting isopropanolate with P_2O_5 and rare-earth chlorides. Following the same procedure, LuPO_4 was prepared as nanometric powder and doped successfully with Eu^{3+} ions up to 5% mol [49]. Successful doping of $(\text{Y}, \text{Lu})\text{PO}_4$ with cations like Eu^{3+} or Ce^{3+} is not evident since EuPO_4 and CePO_4 crystalize in a different crystalline structure (monazite instead of xenotime). Once again, the use of sol-gel

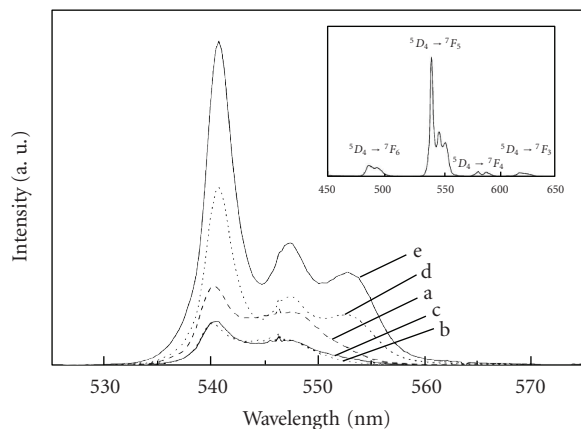


FIGURE 3: Room temperature emission spectra under X-ray excitation of 1% Tb^{3+} doped HfO_2 powders with (a) 0, (b) 1, (c) 4, (d) 9, and (e) 20% Y^{3+} . Reproduced from [34] © 2003 with permission from Elsevier.

process is responsible for the good homogeneity of the materials and the efficient dispersion of doping ions throughout the matrix. LuPO_4 powders doped with Ce^{3+} , Eu^{3+} , and Tb^{3+} ions at various concentrations were prepared and their scintillation properties reported [50].

The optima for scintillation yield were found to be 0.1, 10, and 5%, respectively for Ce^{3+} , Eu^{3+} , and Tb^{3+} (Table 1). An important afterglow was observed that could be limitative for some practical applications.

5. HAFNIUM OXIDES

Due to its rather large band gap and low-phonon energy, hafnia is a suitable host matrix for rare-earth doping. Rare-earth doped HfO_2 and SiO_2 - HfO_2 thin films have been prepared by sol-gel chemistry [51, 52]. In particular, Lange et al. studied Ln-doped HfO_2 thin films (Ln = Sm, Eu, Tb) as potential scintillators [53]. The sol was prepared by reacting Hafnium butoxide in hexane solution, doping was performed by adding rare-earth chlorides. Films were deposited by dip coating on quartz and silicon substrates. Strongly observed photoluminescence suggested an efficient transfer from the host material to the rare-earth ions.

In 2003, Villanueva-Ibañez et al. published a paper reporting the preparation of Yttrium-Hafnium oxide powders by sol-gel chemistry [54]. Yttrium was substituted to Hafnium from 0 to 20% yielding phase transformation and facilitating doping with Tb^{3+} ions (1%). Hafnium ethoxide and Yttrium and Terbium nitrates were mixed in ethanol in the presence of acetylacetonone. The xerogels were calcined up to 1000°C where complete crystallization was observed. The emission of the various samples has been measured under X-ray excitation (Figure 3). The most efficient materials are $\text{HfO}_2 : \text{Tb}^{3+}$ 1% and $\text{HfO}_2 : \text{Y}^{3+}$ 20% Tb^{3+} 1%. No quantitative information on the scintillation yield and afterglow is reported in the paper.

Strontium hafnium perovskite SrHfO_3 has been identified as potential scintillator in particular when activated with

Ce^{3+} ions [55]. Sol-gel preparation of SrHfO_3 films and powders has been reported recently [56]. The authors used in situ prepared strontium ethoxide and hafnium ethoxide in methoxyethanol for the preparation of a stable sol. Doping with Ce^{3+} ions was performed by adding cerium nitrate (1 mol% Ce^{3+}). Samples were annealed from 600 to 1100°C. Samples crystallize with the perovskite structure at 800° and 750°C for powders and films, respectively. Upon heating at higher temperature, monoclinic HfO_2 phase also appears. Ce^{3+} emission is detected under X-ray excitation on powders annealed at 1100°C but not for other conditions and not for the films. The same authors studied the influence of the Sr/Hf ratio on the scintillation properties of sol-gel-derived Ce^{3+} doped strontium hafnate powders [57]. Varying the Sr/Hf ratio from 0.66 to 1.63, it was shown that the best scintillation efficiency was observed for the perovskite stoichiometric ratio Sr/Hf = 1 and for powders annealed at 1200°C. At this temperature, the perovskite phase is well crystallized but HfO_2 monoclinic phase is also observed. It seems that optimization of the preparation procedure is still not achieved and that improvement is possible.

6. TUNGSTATES

Due to their high densities, tungsten oxides have received much attention from the scintillators community in particular lead tungstate [58, 59] and cadmium tungstate [60, 61]. These materials are intrinsically luminescent and do not require further doping with emitting ions.

Very few works can be found in the literature for the preparation of tungstate scintillators by sol-gel chemistry. In 2003, Lennstrom et al. proposed the sol-gel elaboration of CdWO_4 thin films by using WCl_6 and cadmium acetate in ethanol [62]. Stable sol was spin coated on various substrates. Powders and films were produced which showed photoluminescence corresponding to the CdWO_4 phase. No measurement was performed under high-energy excitation.

More recently, Shang et al. studied the effect of doping in nanostructured CdWO_4 films [63]. Tungsten isopropoxide was prepared from WOCl_4 and reacted with cadmium nitrate. Solution was doped with either lithium, boron or bismuth. The doped sols were then used to prepare thin films by spin coating or hydrolyzed to yield powders. Study of photoluminescence (UV excitation) showed that doping with Li^+ , Bi^{3+} , or B^{3+} enhanced the luminescence of the material. This has been associated with diminution of grains size and higher density. Here again, no scintillation measurement has been performed.

7. CONCLUSIONS

Through an exhaustive survey of recent literature, it has been shown that sol-gel chemistry is an efficient tool to prepare various scintillating oxides. Available data have been reported and summarized in Table 1. As observed for other domains, the possibility to prepare thin films is considered the most important advantage of sol-gel process. The other important advantage brought by sol-gel chemistry is the possibility to easily vary the composition and to dope the

TABLE 1: Compositions, form, and scintillation yield (when available) of sol-gel-derived scintillating materials.

Compound	Emitting ion	Form	Light yield (Photons/MeV)	Reference
Y ₂ O ₃	Nd ³⁺ (1%)	Films	—	[11]
Gd ₂ O ₃	Eu ³⁺ (5%)	Powders, films	18500	[17]
Lu ₂ O ₃	Eu ³⁺ (5%)	Powders, films	19750	[17]
LuBO ₃	Eu ³⁺ (5%)	Powders, films	8900	[27]
	Tb ³⁺ (5%)		4400	[27]
	Ce ³⁺ (0.5%)		8100	[26]
LuPO ₄	Eu ³⁺ (10%)	Powders	5400	[34]
	Tb ³⁺ (5%)		9200	
	Ce ³⁺ (0.1%)		7400	
Lu ₂ SiO ₅	Eu ³⁺ (2%)	Powders, films	2900	[22]
	Tb ³⁺ (1.5%)		13100	[22]
	Ce ³⁺ (0.5%)		20000	[20]
Lu ₃ Al ₅ O ₁₂	Tb ³⁺	Powders, films	—	[29]
	Ce ³⁺ (1%)	Powders	—	[30]
HfO ₂	Sm ³⁺ , Eu ³⁺ , Tb ³⁺ (0.4%)	Films	—	[37]
	Y ³⁺ (20%)/Tb ³⁺ (1%)	Powders	—	[38]
SrHfO ₃	Ce ³⁺ (1%)	Powders	< 4000	[40, 41]
CdWO ₄	—	Films	—	[49]
	Li ⁺ , B ³⁺ , Bi ³⁺ (0.5–10%)	Powders, films	—	[50]

materials. In most cases, the emission of scintillators comes from doping ions like rare earth ions. Efficient doping with such ions can be achieved by sol-gel chemistry. It is indeed striking to note that optimal doping concentration is usually found much higher for sol-derived materials when compared to solid-state-derived synthesis. In our opinion, this comes from the conjunction of two opposite effects. The light yield of sol-gel derived materials is usually found lower than the ones prepared by solid state reaction for a given doping level, see [48] for instance. This is usually associated with residual hydroxyl groups provoking luminescence quenching. On the other hand, sol-gel derived materials are known to present a better dispersion of doping ions. This allows higher doping concentration to be reached without concentration quenching and thus higher emission efficiency. These two effects going into opposite directions somehow compensate each other and the optimum light yield is usually found equivalent for the different synthesis routes but with different doping levels (see Table 1).

In the specific case of Ce³⁺ doping which is a very important case for scintillation applications, a detailed study has been proposed by combining X-ray photoelectron spectroscopy (XPS) and X-ray absorption spectroscopy (XANES) [64]. Considering various materials, it has been shown that mixed oxidation state Ce³⁺/Ce⁴⁺ was clearly observed for sol-gel-derived materials. This tends to lower the scintillation efficiency but this lowering is compensated by higher doping concentrations without quenching.

In conclusion, the sol-gel process appears to be a very valuable way to prepare scintillators with enhanced properties and to develop new scintillators thanks to the versatility of this chemical route. In particular, thin films applications

are very attractive. The sol-gel process also allows fundamental studies by changing easily the nature of the doping ions or the composition. Finally, the possibility to prepare hybrid materials, not reported in this work, is a new opportunity to develop new generation scintillation materials for medical imaging.

ACKNOWLEDGMENTS

The author would like to thank C. Mansuy, R. Mahiou, and C. Dujardin for fruitful collaboration and discussions. Financial support from French FRT under Project LuminiX (RNTS-01B262) and FNS under “ACI Nanostructures” Project LuNaTIC (N5501) is gratefully acknowledged.

REFERENCES

- [1] in *Crystal 2000: Proceedings of International Workshop on Heavy Scintillators for Scientific and Industrial Applications*, Chamonix, France, September 1992.
- [2] in *Proceedings of the MRS Symposium on Scintillator and Phosphor Materials*, vol. 348, Materials Research Society, Pittsburgh, Pa, USA, 1994.
- [3] in *Proceedings of the International Conference on Inorganic Scintillators and Their Applications (SCINT '95)*, Delft University Press, Delft, The Netherlands, August-September 1995.
- [4] in *Proceedings of the International Conference on Inorganic Scintillators and Their Applications (SCINT '97)*, Shangai Branch Press, Shangahi, China, September 1997.
- [5] in *Proceedings of the International Conference on Inorganic Scintillators and Their Applications (SCINT '99)*, Moscow, Russia, August 1999.

- [6] in *Proceedings of the 6th International Conference on Inorganic Scintillators and Their Use in Scientific and Industrial Applications (SCINT '01)*, Chamonix, France, September 2001.
- [7] in *Proceedings of the 7th International Conference on Inorganic Scintillators and Their Use in Scientific and Industrial Applications (SCINT '03)*, Valencia, Spain, September 2003.
- [8] C. W. E. van Eijk, "New scintillators, new light sensors, new applications," in *Proceedings of the International Conference on Inorganic Scintillators and Their Applications (SCINT '97)*, p. 3, Shanghai Branch Press, Shanghai, China, September 1997.
- [9] N. Chiodini, M. Fasoli, M. Martini, et al., "High-efficiency $\text{SiO}_2\text{:Ce}^{3+}$ glass scintillators," *Applied Physics Letters*, vol. 81, no. 23, pp. 4374–4376, 2002.
- [10] N. Chiodini, M. Fasoli, M. Martini, et al., "Rare-earth doped sol-gel silicate glasses for scintillator applications," *Radiation Effects and Defects in Solids*, vol. 158, no. 1–6, pp. 463–467, 2003.
- [11] J.-L. Noguez, S. Majewski, J. K. Walker, M. Bowen, R. Wojcik, and W. V. Moreshead, "Fast, radiation-hard scintillating detector: a potential application for sol-gel glass," *Journal of the American Ceramic Society*, vol. 71, no. 12, pp. 1159–1163, 1988.
- [12] C. Sanchez and F. Ribot, "Design of hybrid organic-inorganic materials synthesized via sol-gel chemistry," *New Journal of Chemistry*, vol. 18, no. 10, pp. 1007–1047, 1994.
- [13] M. E. Keillor and L. W. Burggraf, "Detecting alpha radiation by scintillation in porous materials," *IEEE Transactions on Nuclear Science*, vol. 44, no. 5, pp. 1741–1746, 1997.
- [14] I. Hamerton, J. N. Hay, J. R. Jones, and S.-Y. Lu, "Covalent incorporation of 2,5-diphenyloxazole in sol-gel matrices and their application in radioanalytical chemistry," *Chemistry of Materials*, vol. 12, no. 2, pp. 568–572, 2000.
- [15] L. Matthews and E. T. Knobbe, "Luminescence behavior of europium complexes in sol-gel derived host materials," *Chemistry of Materials*, vol. 5, no. 12, pp. 1697–1700, 1993.
- [16] R. Reisfeld, T. Saraidarov, M. Gaft, and M. Pietraszkiewicz, "Luminescence of cryptate-type Eu^{3+} complexes incorporated in inorganic and ormoer sol-gel matrices," *Optical Materials*, vol. 29, no. 5, pp. 521–527, 2007.
- [17] S. Comby, F. Gumy, J.-C. G. Bünzli, T. Saraidarov, and R. Reisfeld, "Luminescent properties of an Yb podate in sol-gel silica films, solution, and solid state," *Chemical Physics Letters*, vol. 432, no. 1–3, pp. 128–132, 2006.
- [18] D. C. Bradley, R. C. Mehrotra, and D. P. Gaur, *Metal Alkoxides*, Academic Press, London, UK, 1978.
- [19] V. G. Kessler, "Molecular structure design and synthetic approaches to the heterometallic alkoxide complexes (soft chemistry approach to inorganic materials by the eyes of a crystallographer)," *Chemical Communications*, no. 11, pp. 1213–1222, 2003.
- [20] C. J. Brinker and G. W. Scherer, *Sol-Gel Science: The Physics and Chemistry of Sol-Gel Processing*, Academic Press, Boston, Mass, USA, 1990.
- [21] J. Livage, M. Henry, and C. Sanchez, "Sol-gel chemistry of transition-metal oxides," *Progress in Solid State Chemistry*, vol. 18, no. 4, pp. 259–341, 1988.
- [22] V. G. Kessler, G. I. Spijksma, G. A. Seisenbaeva, S. Håkansson, D. H. A. Blank, and H. J. M. Bouwmeester, "New insight in the role of modifying ligands in the sol-gel processing of metal alkoxide precursors: a possibility to approach new classes of materials," *Journal of Sol-Gel Science and Technology*, vol. 40, no. 2-3, pp. 163–179, 2006.
- [23] A. Senouci, M. Yaakoub, C. Huguenard, and M. Henry, "Molecular templating using titanium(IV) (oxo)alkoxides and titanium(IV) (oxo)aryloxides," *Journal of Materials Chemistry*, vol. 14, no. 21, pp. 3215–3230, 2004.
- [24] P. J. R. Montes, M. E. G. Valerio, M. A. Macêdo, F. Cunha, and J. M. Sasaki, "Yttria thin films doped with rare earth for applications in radiation detectors and thermoluminescent dosimeters," *Microelectronics Journal*, vol. 34, no. 5–8, pp. 557–559, 2003.
- [25] A. García-Murillo, C. Le Luyer, C. Dujardin, C. Pedrini, and J. Mugnier, "Elaboration and characterization of Gd_2O_3 waveguiding thin films prepared by the sol-gel process," *Optical Materials*, vol. 16, no. 1-2, pp. 39–46, 2001.
- [26] H. Guo, X. Yang, T. Xiao, W. Zhang, L. Lou, and J. Mugnier, "Structure and optical properties of sol-gel derived Gd_2O_3 waveguide films," *Applied Surface Science*, vol. 230, no. 1–4, pp. 215–221, 2004.
- [27] C. Duverger, M. Benatsou, J. M. Nedelec, et al., "Waveguide Raman spectroscopy: a non-destructive tool for the characterization of amorphous thin films," *Journal of Molecular Structure*, vol. 480-481, pp. 169–178, 1999.
- [28] C. Le Luyer, A. García-Murillo, E. Bernstein, and J. Mugnier, "Waveguide Raman spectroscopy of sol-gel Gd_2O_3 thin films," *Journal of Raman Spectroscopy*, vol. 34, no. 3, pp. 234–239, 2003.
- [29] A. García-Murillo, C. Le Luyer, C. Garapon, et al., "Optical properties of europium-doped Gd_2O_3 waveguiding thin films prepared by the sol-gel method," *Optical Materials*, vol. 19, no. 1, pp. 161–168, 2002.
- [30] A. García-Murillo, C. Le Luyer, C. Dujardin, et al., "Elaboration and scintillation properties of Eu^{3+} -doped Gd_2O_3 and Lu_2O_3 sol-gel films," *Nuclear Instruments and Methods in Physics Research A*, vol. 486, no. 1-2, pp. 181–185, 2002.
- [31] A. García-Murillo, C. Le Luyer, C. Pedrini, and J. Mugnier, "Synthesis and properties of Lu_2O_3 sol-gel films," *Journal of Alloys and Compounds*, vol. 323-324, pp. 74–77, 2001.
- [32] E. Bescher, S. R. Robson, J. D. Mackenzie, B. Patt, J. Iwanczyk, and E. J. Hoffman, "New lutetium silicate scintillators," *Journal of Sol-Gel Science and Technology*, vol. 19, no. 1–3, pp. 325–328, 2000.
- [33] C. Mansuy, R. Mahiou, and J. M. Nedelec, "A new sol-gel route to Lu_2SiO_5 (LSO) scintillator: powders and thin films," *Chemistry of Materials*, vol. 15, no. 17, pp. 3242–3244, 2003.
- [34] C. Mansuy, F. Leroux, R. Mahiou, and J. M. Nedelec, "Preferential site substitution in sol-gel derived Eu^{3+} doped Lu_2SiO_5 : a combined study by X-ray absorption and luminescence spectroscopies," *Journal of Materials Chemistry*, vol. 15, no. 38, pp. 4129–4135, 2005.
- [35] C. Mansuy, "Sol-gel elaboration and characterization of inorganic scintillating materials," Ph.D. thesis, Université Blaise Pascal, Clermont-Ferrand, France, 2004.
- [36] L. Pídol, O. Guillot-Noël, M. Jourdir, et al., "Scintillation quenching by Ir^{3+} impurity in cerium doped lutetium pyrosilicate crystals," *Journal of Physics: Condensed Matter*, vol. 15, no. 45, pp. 7815–7821, 2003.
- [37] L. Pídol, A. Khan-Harari, B. Viana, et al., "Scintillation properties of $\text{Lu}_2\text{Si}_2\text{O}_7\text{:Ce}^{3+}$, a fast and efficient scintillator crystal," *Journal of Physics: Condensed Matter*, vol. 15, no. 12, pp. 2091–2102, 2003.
- [38] D. Boyer, G. Bertrand-Chadeyron, R. Mahiou, L. Lou, A. Brioude, and J. Mugnier, "Spectral properties of LuBO_3 powders and thin films processed by the sol-gel technique," *Optical Materials*, vol. 16, no. 1-2, pp. 21–27, 2001.
- [39] C. Mansuy, J. M. Nedelec, C. Dujardin, and R. Mahiou, "Scintillation of sol-gel derived lutetium orthoborate doped with

- Ce³⁺ ions,” *Journal of Sol-Gel Science and Technology*, vol. 32, no. 1–3, pp. 253–258, 2004.
- [40] C. Mansuy, J. M. Nedelec, C. Dujardin, and R. Mahiou, “Concentration effect on the scintillation properties of sol-gel derived LuBO₃ doped with Eu³⁺ and Tb³⁺,” *Optical Materials*, vol. 29, no. 6, pp. 697–702, 2007.
- [41] C. Mansuy, E. Tomasella, R. Mahiou, L. Gengembre, J. Grimblot, and J. M. Nedelec, “Characterization of sol-gel derived scintillating LuBO₃ films doped with rare earth ions,” *Thin Solid Films*, vol. 515, no. 2, pp. 666–669, 2006.
- [42] Y. Baogui, Y. Min, Z. Weiping, G. Hai, and L. Lin, “Luminescence properties of Tb³⁺-doped LuAG films prepared by pechini sol-gel method,” *Journal of Rare Earths*, vol. 24, no. 6, pp. 745–748, 2006.
- [43] X.-J. Liu, H.-L. Li, R.-J. Xie, Y. Zeng, and L.-P. Huang, “Spectroscopic properties of nano-sized cerium-doped lutetium aluminum garnet phosphors via sol-gel combustion process,” *Journal of Luminescence*, vol. 124, no. 1, pp. 75–80, 2007.
- [44] A. Lempicki, E. Berman, A. J. Wojtowicz, M. Balcerzyk, and L. A. Boatner, “Cerium-doped orthophosphates: new promising scintillators,” *IEEE Transactions on Nuclear Science*, vol. 40, no. 4, part 1, pp. 384–387, 1993.
- [45] A. J. Wojtowicz, A. Lempicki, D. Wisniewski, M. Balcerzyk, and C. Brecher, “The carrier capture and recombination processes in Ln³⁺-activated scintillators,” *IEEE Transactions on Nuclear Science*, vol. 43, no. 3, part 3, pp. 2168–2173, 1996.
- [46] W. W. Moses, M. J. Weber, S. E. Derenzo, D. Perry, P. Berdahl, and L. A. Boatner, “Prospects for dense, infrared emitting scintillators,” *IEEE Transactions on Nuclear Science*, vol. 45, no. 3, part 1, pp. 462–466, 1998.
- [47] D. Wisniewski, S. Tavernier, P. Dorenbos, et al., “VUV scintillation of LuPO₄:Nd and YPO₄:Nd,” *IEEE Transactions on Nuclear Science*, vol. 49, no. 3, pp. 937–940, 2002.
- [48] J. M. Nedelec, D. Avignant, and R. Mahiou, “Soft chemistry routes to YPO₄-based phosphors: dependence of textural and optical properties on synthesis pathways,” *Chemistry of Materials*, vol. 14, no. 2, pp. 651–655, 2002.
- [49] J. M. Nedelec, C. Mansuy, and R. Mahiou, “Sol-gel derived YPO₄ and LuPO₄ phosphors, a spectroscopic study,” *Journal of Molecular Structure*, vol. 651–653, pp. 165–170, 2003.
- [50] C. Mansuy, J. M. Nedelec, C. Dujardin, and R. Mahiou, “Scintillation of sol-gel derived lutetium orthophosphate doped with rare earth ions,” *Journal of Sol-Gel Science and Technology*, vol. 38, no. 1, pp. 97–105, 2006.
- [51] R. M. Almeida, A. C. Marques, S. Pelli, et al., “Spectroscopic assessment of silica-titania and silica-hafnia planar waveguides,” *Philosophical Magazine*, vol. 84, no. 13–16, pp. 1659–1666, 2004.
- [52] R. R. Gonçalves, G. Carturan, M. Montagna, et al., “Erbium-activated HfO₂-based waveguides for photonics,” *Optical Materials*, vol. 25, no. 2, pp. 131–139, 2004.
- [53] S. Lange, V. Kiisk, V. Reedo, M. Kirm, J. Aarik, and I. Sildos, “Luminescence of RE-ions in HfO₂ thin films and some possible applications,” *Optical Materials*, vol. 28, no. 11, pp. 1238–1242, 2006.
- [54] M. Villanueva-Ibañez, C. Le Luyer, C. Dujardin, and J. Mugnier, “Elaboration, structural and spectroscopic properties of rare earth-doped yttrium-hafnium sol-gel oxide powders for scintillation applications,” *Materials Science and Engineering B*, vol. 105, no. 1–3, pp. 12–15, 2003.
- [55] H. Yamamoto, M. Mikami, Y. Shimomura, and Y. Oguri, “Host-to-activator energy transfer in a new blue-emitting phosphor SrHfO₃:Tm³⁺,” *Journal of Luminescence*, vol. 87–89, pp. 1079–1082, 2000.
- [56] M. Villanueva-Ibañez, C. Le Luyer, S. Parola, O. Marty, and J. Mugnier, “A new elaboration route by sol-gel process for cerium doped SrHfO₃ films and powders,” *Journal of Sol-Gel Science and Technology*, vol. 31, no. 1–3, pp. 277–281, 2004.
- [57] M. Villanueva-Ibañez, C. Le Luyer, S. Parola, C. Dujardin, and J. Mugnier, “Influence of Sr/Hf ratio and annealing treatment on structural and scintillating properties of sol-gel Ce³⁺-doped strontium hafnate powders,” *Optical Materials*, vol. 27, no. 9, pp. 1541–1546, 2005.
- [58] M. Itoh and M. Fujita, “Optical properties of scheelite and rapsite PbWO₄ crystals,” *Physical Review B*, vol. 62, no. 19, pp. 12825–12830, 2000.
- [59] V. V. Laguta, M. Martini, A. Vedda, et al., “Photoinduced Pb⁺ center in PbWO₄: electron spin resonance and thermally stimulated luminescence study,” *Physical Review B*, vol. 64, no. 16, Article ID 165102, 8 pages, 2001.
- [60] V. Ryzhikov, L. Nagornaya, V. Volkov, V. Chernikov, and O. Zelenskaya, “Thermal neutron detectors based on complex oxide crystals,” *Nuclear Instruments and Methods in Physics Research A*, vol. 486, no. 1–2, pp. 156–159, 2002.
- [61] L. Nagornaya, G. Onyshchenko, E. Pirogov, et al., “Production of the high-quality CdWO₄ single crystals for application in CT and radiometric monitoring,” *Nuclear Instruments and Methods in Physics Research A*, vol. 537, no. 1–2, pp. 163–167, 2005.
- [62] K. Lennstrom, S. J. Limmer, and G. Cao, “Synthesis of cadmium tungstate films via sol-gel processing,” *Thin Solid Films*, vol. 434, no. 1–2, pp. 55–61, 2003.
- [63] H. Shang, Y. Wang, B. Milbrath, M. Bliss, and G. Cao, “Doping effects in nanostructured cadmium tungstate scintillation films,” *Journal of Luminescence*, vol. 121, no. 2, pp. 527–534, 2006.
- [64] C. Mansuy, J. M. Nedelec, and R. Mahiou, “Molecular design of inorganic scintillators: from alkoxides to scintillating materials,” *Journal of Materials Chemistry*, vol. 14, no. 21, pp. 3274–3280, 2004.

Review Article

Photoluminescence of Silicon Nanocrystals in Silicon Oxide

L. Ferraioli,¹ M. Wang,^{2,3} G. Pucker,² D. Navarro-Urrios,¹ N. Daldosso,¹ C. Kompocholis,² and L. Pavesi¹

¹ *Laboratorio di Nanoscienze, Dipartimento di Fisica, Università di Trento, Via Sommarive 14, 38100 Povo, Italy*

² *Fondazione Bruno Kessler, Via Sommarive 18, 38100 Povo, Italy*

³ *State Key Laboratory of Silicon Materials, Zhejiang University, Hangzhou 310027, China*

Received 15 May 2007; Accepted 17 November 2007

Recommended by Tran Kim Anh

Recent results on the photoluminescence properties of silicon nanocrystals embedded in silicon oxide are reviewed and discussed. The attention is focused on Si nanocrystals produced by high-temperature annealing of silicon rich oxide layers deposited by plasma-enhanced chemical vapor deposition. The influence of deposition parameters and layer thickness is analyzed in detail. The nanocrystal size can be roughly controlled by means of Si content and annealing temperature and time. Unfortunately, a technique for independently fine tuning the emission efficiency and the size is still lacking; thus, only middle size nanocrystals have high emission efficiency. Interestingly, the layer thickness affects the nucleation and growth kinetics so changing the luminescence efficiency.

Copyright © 2007 L. Ferraioli et al. This is an open access article distributed under the Creative Commons Attribution License, which permits unrestricted use, distribution, and reproduction in any medium, provided the original work is properly cited.

1. INTRODUCTION

Since the discovery of luminescent properties of porous silicon [1–3], many research efforts were dedicated to the light emitting properties of nanometric-sized silicon. Light emitting Si-based materials promise to allow merging of electronics and photonics in a single chip, thus overcoming the restrictions settled by the power dissipation bottleneck on the short/medium distance interconnects [4, 5]. Unfortunately, bulk Si is a poor light emitting material because of its indirect band gap. Excited electron-hole pairs have very long radiative lifetime (milliseconds), thus competing nonradiative recombinations rule and cause most of the excited electron-hole pairs to recombine nonradiatively. Silicon nanocrystals (Si-nc) are the most promising material to turn Si in an effective light emitter. Quantum confinement and spatial localization in a small region of excited electron-hole pairs push up the radiative efficiency to values as high as 10–50%.

Si-nc have also emerged as promising biophotonics materials [6–8]. Due to their spectral emission in the region of transparency of biological tissues, they could be used as luminescent markers for biological matter. The great advantage with respect to III-V or II-VI semiconductors is the low toxicity of silicon. Many efforts are dedicated right now to the luminescence stabilization of water-dispersed Si-nc by surface passivation with organic compounds [9, 10].

Room temperature luminescence emission in silicon nanocrystals (Si-nc) is routinely observed independently of

the preparation method [11–14]. The emission is characterized by a wide band in the wavelength range 600–900 nm. Qualitatively in agreement with the quantum confinement model, the emission band redshifts with the increase of the Si-nc mean size, which allows to attribute this band to electron-hole recombination in Si-nc. Luminescence efficiency is similar to that reported elsewhere [15, 16] for PECVD samples produced in Catania. Often, the second band, centered at 500 nm, can be observed in the luminescence spectra. It is different by the Si-nc-related band because it does not shift by changing crystallites size. This second band can be related to recombination in matrix defects which can be quenched by post-growth treatment, such as hydrogen passivation.

A way to obtain well-passivated Si-nc is the deposition of Si rich oxide (SiO_x) layers on a substrate (silicon or quartz) by plasma-enhanced chemical vapor deposition (PECVD). Si-nc are formed as a consequence of Si segregation and clustering during high-temperature annealing [13, 14]. In the following, the luminescence properties of PECVD growth Si-nc will be presented.

2. EXPERIMENTAL

A series silicon-rich oxide films were grown on Si (100) wafers by PECVD using SiH₄ and N₂O as precursor gases. The working pressure was maintained at 500 mTorr and the supplied power was 100 W with a radio frequency of

TABLE 1: Samples characteristics and thickness.

Sample	S1	S2	S3	S4	S5	S6	S7
Γ ($\text{N}_2\text{O}/\text{SiH}_4$)	15	15	15	15	25	25	25
Thickness (nm)	50	50	200	200	50	200	200
Si_3N_4 capping layer	Yes	No	Yes	No	Yes	Yes	No

13.56 MHz. Si incorporation into the silicon-rich silicon oxide (SRO) layer is controlled by the N_2O to SiH_4 flow rate ratio, we will refer to this parameter as Γ . The higher is Γ the lower the Si content into the film. Typically, since we are using N_2O , about 1% to 2% atoms of nitrogen were incorporated during the deposition. Si-nc segregation was obtained by one-hour long annealing at 1000°C or 1100°C in a nitrogen atmosphere. In order to explore the application for light-emitting device, films were deposited with two different thicknesses. Some of them were covered by a capping layer to avoid oxygen and nitrogen in-diffusion during the annealing. The description of these films is summarized in Table 1.

Photoluminescence (PL) measurements were performed with two different spectrometers and two different pumping wavelengths for a total of three different configurations.

- (i) “Vis-CCD.” Samples were excited with the 488 nm line of an argon laser, pumping light was filtered with a 488 nm bandpass filter. Pump power was 50 mW corresponding roughly to a pump intensity of $20\text{ W}/\text{cm}^2$. Photoluminescence (PL) emission, in the wavelength range from 500 nm to 1000 nm, was collected by a single grating monochromator coupled with a cooled CCD. A long wavelength pass filter (cutoff at 550 nm) was put on the collection line in order to avoid noise coming from the scattering of pump light from the samples surface.
- (ii) “Vis-PMT.” The same exciting condition as mentioned above. PL emission, in the wavelength range from 500 nm to 900 nm, was collected by a double-grating monochromator coupled with a cooled GaAs photomultiplier.
- (iii) “UV-PMT.” Samples were excited with the 360 nm line of an argon laser. Pump power was 5 mW corresponding roughly to an intensity of $2\text{ W}/\text{cm}^2$. PL emission, in the wavelength range from 400 nm to 900 nm, was collected by a double-grating monochromator coupled with a cooled GaAs photomultiplier.

3. RESULTS AND DISCUSSION

3.1. PECVD samples. Detailed variation of Γ

Detailed variation of Si content was obtained with a fine tuning of Γ ($\text{N}_2\text{O}/\text{SiH}_4$) in the range from 2.5 to 30. $\Gamma = 2.5$ corresponds roughly to 52% of atomic Si ($\text{SiO}_{0.9}$). $\Gamma = 30$ corresponds to a stoichiometric silicon oxide (SiO_2). Photoluminescence measurements were performed in the Vis-CCD configuration (488 nm pump light, monochromator +

CCD). PL spectra are reported in Figures 1(a) and 1(b) for annealing temperatures of 1000°C and 1100°C , respectively. PL emission from samples with Γ below 8 is extremely low and is not reported in Figures 1(a) and 1(b). Despite the large variation in silicon content, the luminescence emission is confined in the wavelength range from 500 nm to 1000 nm. The maximum of PL emission is obtained at $\Gamma 15$ – $\Gamma 16$ for both the annealing temperatures. Peak intensity and peak wavelength are reported in Figures 1(c) and 1(d) as a function of Γ for 1000°C and 1100°C , respectively. In both cases, peak intensity shows a bell-like shape as a function of the ratio between N_2O and SiH_4 . Peak wavelength blue shifts increasing Γ . This indicates a reduction of Si-nc mean size with the reduction of Si content into the SRO layer.

In principle, Si-nc size can be controlled by the annealing temperature and Si content of the SRO. Keeping fixed the content of silicon, Si-nc size can be increased by increasing the annealing temperature or, similarly, at a fixed temperature Si-nc size can be increased by increasing the content of Si into the SRO. The search for high luminescent Si-nc imposes to find a trade-off between Si concentration and annealing temperature.

Figures 1(c) and 1(d) clearly demonstrate that the luminescence emission is not effective in SRO samples with extremely high or extremely low Si concentrations. The reasons are different for the two cases. With high-Si concentration, large size Si-nc are obtained. Quantum confinement effect is highly reduced for Si-nc radius larger than exciton Bohr radius and, as a consequence, oscillator strength for the luminescence transition tends toward the value of bulk Si. Thereby, the luminescence efficiency decreases as the nanocrystal radius increases due to a pure quantum confinement effect. Conversely, the reduction of Si concentration determines the development of smaller size Si-nc, then high emission efficiency can be expected due to quantum confinement effect. This is not the case because two detrimental effects are in competition with the quantum confinement effect and dominate at low Si concentration. The first is the reduction of the Si-nc density with the reduction of Si concentration. The second is connected with the thermodynamics of Si crystallization. Quantum dots crystallization is favored by the size increase because of an increased gain in the volume-free energy during the amorphous to crystalline transition. At a fixed temperature, crystallization process is favored at large Si content thanks to the increase of clusters mean size whereas, at very low Si content, aggregates persist in their amorphous phase also at high temperatures (1000°C and above). Amorphous quantum dots have PL efficiency orders of magnitude lower than crystalline because of the presence of nonradiative centers in the disordered structure. The combined action of density reduction and amorphous fraction growth determines the lowering of PL efficiency at high Γ despite the positive action of quantum confinement.

3.2. Thickness variation

The characterization of the optical properties of Si-nc is performed typically on SRO films hundred of nanometers thick. SRO is intrinsically an insulating material also when Si-nc are

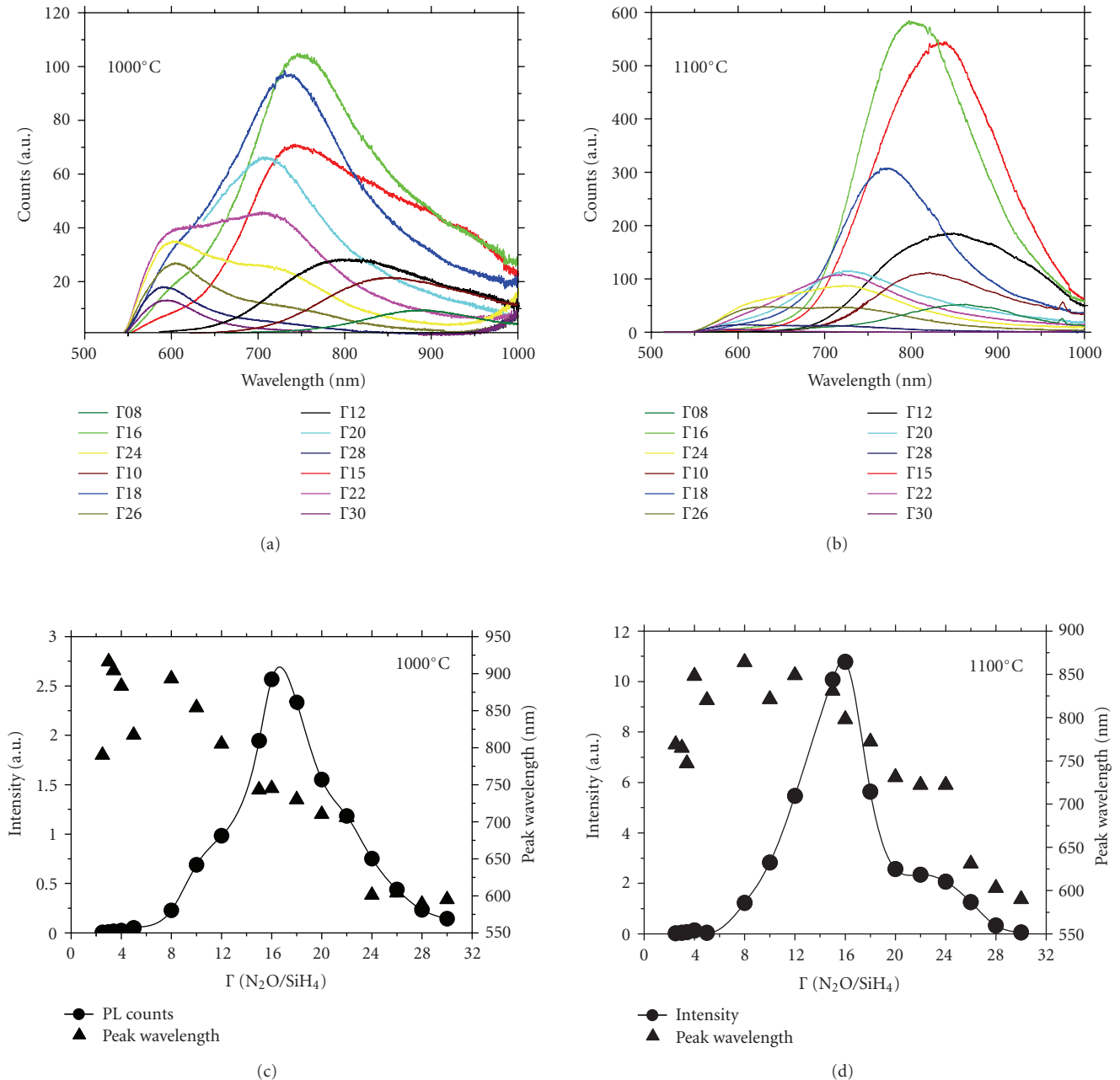


FIGURE 1: (a)-(b) Luminescence spectra of PECVD samples annealed at 1000°C and 1100°C, respectively. The samples are identified by the values of the Γ (N_2O/SiH_4 flow ratio) parameter. (c)-(d) Total luminescence emission and peak wavelength as a function of Γ for samples annealed at 1000°C and 1100°C, respectively. The line is only a guide for eyes.

developed in. In order to explore the possibility of efficient charge injection at low bias for on-chip device integration, a small thickness is required. To explore the formation dynamics and optical properties of Si-nc in very thin films, 50 nm and 200 nm thick SRO layers, with two values of Γ , have been deposited by PECVD. After the deposition, samples were annealed at 1100°C in N_2 atmosphere; detailed characteristics are reported in Table 1. Some samples were covered with a capping layer of Si_3N_4 in order to avoid oxygen in-diffusion

during the annealing process. PL measurements were performed with the UV-PMT (pump wavelength 360 nm) configuration. The luminescence peak intensity was normalized to the samples thickness and reported in Figure 2. Normalized peak intensity (NPI) can be considered as a measure of the PL efficiency of the sample. As can be seen from the figure, thin samples show NPI values one order of magnitude lower than thick samples. The difference is of two orders of magnitude for uncapped samples. A blue shift of the

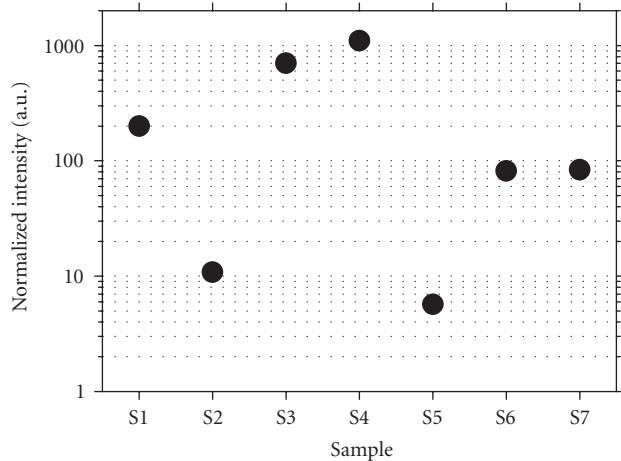


FIGURE 2: Photoluminescence peak intensity normalized to the film thickness. Sample details are reported in Table 1.

luminescence peak can be observed combined with the efficiency reduction (Figure 3) thus indicating the presence of smaller Si-nc.

The whole ensemble of Si-nc seems affected by the thickness of the layer (blue shift of peak wavelength). This means that the kinetics of Si-nc nucleation and growth is influenced by the layer thickness. The reduction of efficiency well correlates with the reduction of mean size and can be attributed to the reduction of nc-Si density and to the increase of Si-nc amorphous fraction as already mentioned.

As a matter of fact [17], SRO can suffer of oxygen in diffusion during the annealing process due to the presence of residual oxygen into the furnace. As a consequence, nc-Si are oxidized and consequently their mean size and their density can be reduced. The capping layer has the purpose of blocking the oxidation process. Thick samples (200 nm thick) are marginally affected by the oxygen in-diffusion process; both intensity (Figure 2) and peak wavelength (Figure 3) are only slightly different in capped and uncapped samples (samples S3, S4, S6, and S7).

Oxygen in-diffusion is, instead, really a detrimental effect for thin samples (S1, S2, and S5); PL emission is noticeably blue shifted (Figure 3) and the efficiency is highly reduced (Figure 2). The presence of the capping layer on the S1 sample is capable of slowing down the oxidation process of nc-Si but it is not enough to completely stop it. PL efficiency of sample S1 is reduced with respect to that of sample S3 and also the peak wavelength is clearly blue shifted. The effect is much more evident on the uncapped S2 sample where the PL efficiency is reduced of two orders of magnitude with respect to the corresponding uncapped thick sample (S4).

3.3. Different pumping wavelength

Silicon rich oxide samples typically develop Si nanocrystals with a wide distribution of size [13, 14]. nc-Si absorption

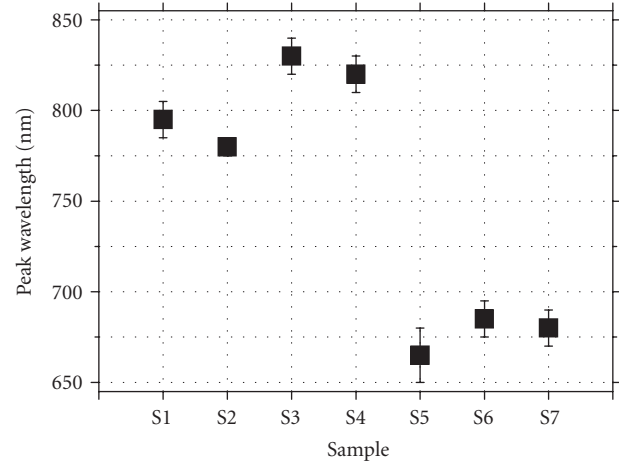


FIGURE 3: Photoluminescence peak wavelength for different samples. Sample details are reported in Table 1.

edge blue shifts with the reduction of the particle size because of the bandgap enlargement. This means that the PL emission can be affected by the choice of the pumping wavelength, that is, by the penetration depth of the laser light or by the selective excitation of a subset of the Si-nc. In order to clarify this effect, photoluminescence measurements were performed with the UV-PMT (pumping wavelength 360 nm) and Vis-PMT (pumping wavelength 488 nm) configurations. Luminescence spectra of sample S3 are reported in Figure 4(a) for both pumping wavelengths. The spectral shape does not change with the change of the pumping wavelength. In Figure 4(b), luminescence spectra of sample S6 are reported for both pumping wavelengths. A slight blue shift can be observed in the case of 360 nm pump. Samples S3 and S6 are different for the Si content, S6 is expected to have smaller size Si-nc than S3. Figure 4(b) clearly indicates that small size Si-nc are better excited by short wavelength light because of bandgap enlargement due to quantum confinement. From the experimental point of view, despite the effect of quantum confinement, PL spectra do not change dramatically and the results obtained with both the wavelength (360 nm and 488 nm) are comparable.

4. CONCLUSIONS

Efficient light emitting silicon nanocrystals of different sizes can be effectively produced by means of PECVD deposition followed by high-temperature annealing of SRO layers. Data point out that luminescence efficiency is a trade-off between positive and negative factors. Light emission is clearly influenced by quantum dots size, being poor for very large or small Si aggregates. A rough control on Si-nc size can be obtained by playing with Si concentration and annealing temperature and time. Unfortunately, a deposition technique capable of independently affecting PL efficiency and Si-nc size is still lacking. Oxygen in-diffusion, during the annealing

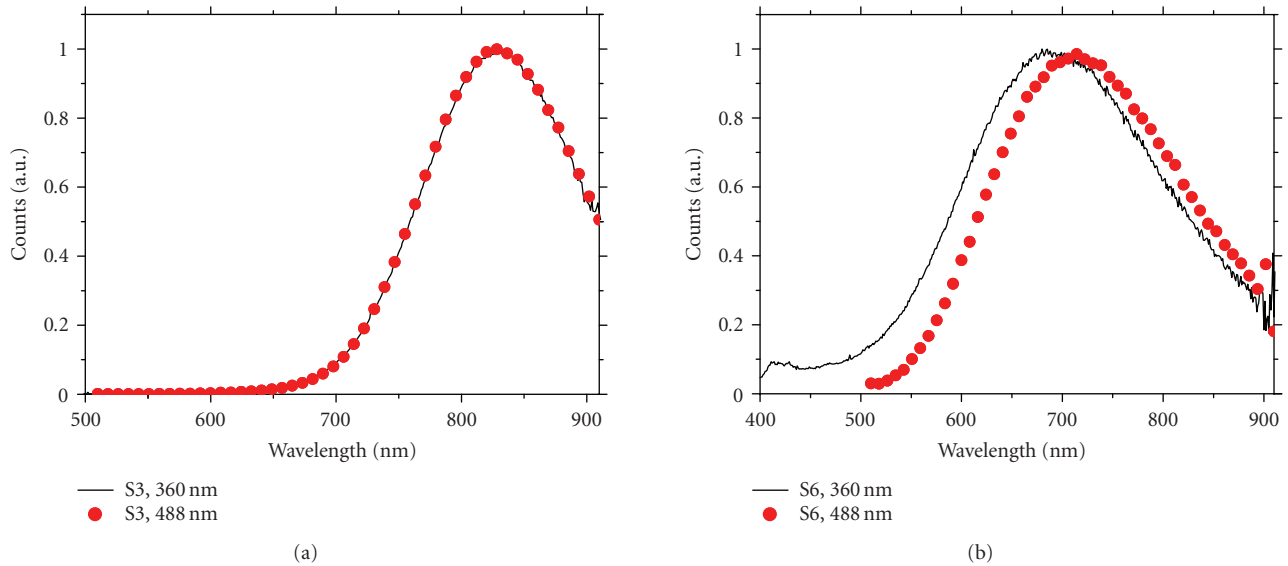


FIGURE 4: (a) Sample S3 luminescence emission for 360 nm (red line) and 488 nm (black line) pumping wavelength. (b) Sample S6 luminescence emission for 360 nm (red line) and 488 nm (black line) pumping wavelength. Sample details are reported in Table 1.

process, affects the PL properties of thin (~ 50 nm) SRO layers. The presence of an Si_3N_4 capping layer is useful to slow down the oxidation process of nc-Si but is not capable to completely stop it especially in thin films. This has to be taken in mind when thinking to device integration.

ACKNOWLEDGMENTS

This work was partially supported by EC through the SEMINANO (NMP-STREP FP6-505285) project. The support of Intel is gratefully acknowledged.

REFERENCES

- [1] S. Ossicini, L. Pavesi, and F. Priolo, *Light Emitting Silicon for Microphotonics*, Tracts in Modern Physics, Springer, New York, NY, USA, 2003.
- [2] L. T. Canham, "Silicon quantum wire array fabrication by electrochemical and chemical dissolution of wafers," *Applied Physics Letters*, vol. 57, no. 10, pp. 1046–1048, 1990.
- [3] L. Pavesi, L. Dal Negro, C. Mazzoleni, G. Franzò, and F. Priolo, "Optical gain in silicon nanocrystals," *Nature*, vol. 408, no. 6811, pp. 440–444, 2000.
- [4] M. Salib, M. Morse, L. Liao, et al., "Silicon photonics," *Intel Technology Journal*, vol. 8, no. 2, 2004.
- [5] G. T. Reed, "Device physics: the optical age of silicon," *Nature*, vol. 427, no. 6975, pp. 595–596, 2004.
- [6] X. Michalet, F. F. Pinaud, L. A. Bentolila, et al., "Quantum dots for live cells, in vivo imaging, and diagnostics," *Science*, vol. 307, no. 5709, pp. 538–544, 2005.
- [7] A. Fu, W. Gu, C. Larabell, and A. P. Alivisatos, "Semiconductor nanocrystals for biological imaging," *Current Opinion in Neurobiology*, vol. 15, no. 5, pp. 568–575, 2005.
- [8] Z. F. Li and E. Ruckenstein, "Water-soluble poly(acrylic acid) grafted luminescent silicon nanoparticles and their use as fluorescent biological staining labels," *Nano Letters*, vol. 4, no. 8, pp. 1463–1467, 2004.
- [9] W. W. Yu, E. Chang, R. Drezek, and V. L. Colvin, "Water-soluble quantum dots for biomedical applications," *Biochemical and Biophysical Research Communications*, vol. 348, no. 3, pp. 781–786, 2006.
- [10] F. Hua, F. Erogbogbo, M. T. Swihart, and E. Ruckenstein, "Organically capped silicon nanoparticles with blue photoluminescence prepared by hydrosilylation followed by oxidation," *Langmuir*, vol. 22, no. 9, pp. 4363–4370, 2006.
- [11] B. Garrido Fernandez, M. López, C. García, et al., "Influence of average size and interface passivation on the spectral emission of Si nanocrystals embedded in SiO_2 ," *Journal of Applied Physics*, vol. 91, no. 2, pp. 798–807, 2002.
- [12] K. Luterova, K. Dohnalova, F. Trojanek, et al., "Porous silicon grains in SiO_2 matrix: Ultrafast photoluminescence and optical gain," *Journal of Non-Crystalline Solids*, vol. 352, no. 28-29, pp. 3041–3046, 2006.
- [13] F. Iacona, G. Franzò, and C. Spinella, "Correlation between luminescence and structural properties of Si nanocrystals," *Journal of Applied Physics*, vol. 87, no. 3, pp. 1295–1303, 2000.
- [14] F. Iacona, C. Bongiorno, C. Spinella, S. Boninelli, and F. Priolo, "Formation and evolution of luminescent Si nanoclusters produced by thermal annealing of SiO_x films," *Journal of Applied Physics*, vol. 95, no. 7, pp. 3723–3732, 2004.
- [15] N. Daldosso, G. Das, S. Larcheri, et al., "Silicon nanocrystal formation in annealed silicon-rich silicon oxide films prepared by plasma enhanced chemical vapor deposition," *Journal of Applied Physics*, vol. 101, no. 11, Article ID 113510, 7 pages, 2007.
- [16] N. Daldosso, G. Das, G. Dalba, et al., "Silicon nanocrystal nucleation as a function of the annealing temperature in SiO_x films," *Materials Research Society Symposium Proceedings Series*, vol. 770, no. 13.4, pp. 1–6, 2003.
- [17] V. Mulloni, P. Bellutti, and L. Vanzetti, "XPS and SIMS investigation on the role of nitrogen in Si nanocrystals formation," *Surface Science*, vol. 585, no. 3, pp. 137–143, 2005.

Research Article

Morphology and Luminescence of Nanocrystalline Nb₂O₅ Doped with Eu³⁺

Daniele Falcomer,¹ Adolfo Speghini,¹ Giulio Ibba,² Stefano Enzo,² Carla Cannas,³
Anna Musinu,³ and Marco Bettinelli¹

¹Dipartimento Scientifico e Tecnologico, Università di Verona and INSTM, UdR Verona, Strada Le Grazie 15, 37134 Verona, Italy

²Dipartimento di Chimica, Università di Sassari and INSTM, UdR Sassari, Via Vienna 2, 07100 Sassari, Italy

³Dipartimento di Scienze Chimiche, Università di Cagliari and INSTM, UdR Cagliari, Complesso Universitario, S.S. 554, Bivio per Sestu, Monserrato, 09042 Cagliari, Italy

Received 12 March 2007; Accepted 4 June 2007

Recommended by Wieslaw Streck

The synthesis of nanocrystalline Nb₂O₅:Eu³⁺ has been achieved by using a Pechini procedure. The obtained materials are single-phase niobia with the orthorhombic structure, average crystallite size around 25 nm and average lattice strain of about 0.002. TEM images show that the particles are rectangular and reasonably isolated. The luminescence of the Eu³⁺ ions in the niobia lattice is efficient and affected by a strong inhomogeneous broadening, due to an important disorder around the lanthanide ions.

Copyright © 2007 Daniele Falcomer et al. This is an open access article distributed under the Creative Commons Attribution License, which permits unrestricted use, distribution, and reproduction in any medium, provided the original work is properly cited.

1. INTRODUCTION

Luminescent niobate crystals activated with trivalent lanthanide ions (Ln³⁺) have been the subject of considerable attention in the past decades. In particular, lithium niobate (LiNbO₃) has attracted huge interest as a valuable host for Ln³⁺ ions, with important applications in the field of optoelectronics and light emitting devices [1]. Moreover, other niobates such as strontium barium niobate (Sr_xBa_{1-x}Nb₂O₆) (SBN) and barium sodium niobate (BNN), activated with Ln³⁺ ions, are very promising materials in the field of photorefractive memories [2] and linear and self-frequency converter solid state laser materials [3, 4]. It is important to note that in all these crystals the location of the Ln³⁺ in the lattice is not obvious, as the trivalent lanthanide ions cannot easily replace the constitutional cations (Li⁺, Na⁺, Sr²⁺, Ba²⁺, Nb⁵⁺) due to clear size and/or charge mismatches. This location has been addressed by several studies where optical and/or structural techniques have been employed [5, 6]. Nevertheless, it is still a matter of debate whether the Ln³⁺ can substitute for the smaller and higher charged Nb⁵⁺ cation in a crystalline lattice [7]. One possible contribution to the solution of this problem is to verify if it is feasible to dope Ln³⁺ ions in a lattice in which *only* the formally pentavalent niobium cations can be replaced, that is, Nb₂O₅. For this reason, we found it in-

teresting to investigate the synthesis and the structural properties of crystalline niobia (Nb₂O₅), doped with Eu³⁺. Moreover, although nanocrystalline niobia has been shown to be a valuable material finding applications as catalyst and sensor [8, 9], very scarce information is available on the preparation and spectroscopic investigation of nanocrystalline Nb₂O₅ activated with lanthanide ions. For this reason, in this paper we report on the synthesis and characterization, and on the optical spectroscopy of Nb₂O₅:Eu³⁺ in nanocrystalline form.

2. EXPERIMENTAL PROCEDURE

Nanocrystalline powders of Eu³⁺ doped Nb₂O₅ were prepared by a Pechini approach [10]. The molar ratio between the niobium and the Eu³⁺ ions was 99:1. An appropriate amount of citric acid was first dissolved in hot water, then niobium ammonium oxalate (NAmOx), Eu(NO₃)₃, and polyethylene glycol (PEG) were added. The resulting solution was stirred for 10 minutes. The gel was obtained by drying the solution at 90°C for 2 days. The nanocrystalline powder was obtained by heat-treating the gel at 400°C for 2 hours and then at 600°C for 1 hour. The sample will be denoted as Nb₂O₅:Eu hereafter.

The powder X-ray diffraction (XRD) pattern of the Nb₂O₅:Eu sample was recorded overnight with a Bruker D8

diffractometer in the Bragg-Brentano geometry using Cu K_α radiation ($\lambda = 1.5418 \text{ \AA}$). The X-ray generator worked at a power of 40 kV and 40 mA and the goniometer was equipped with a graphite monochromator in the diffracted beam. The resolution of the instrument (divergent and antiscatter slits of 0.5°) was determined using $\alpha\text{-SiO}_2$ and $\alpha\text{-Al}_2\text{O}_3$ standards free from the effect of reduced crystallite size and lattice defects. The powder patterns were analyzed according to the Rietveld method [11] using the program MAUD [12] running on a personal computer. It is worth to recall that the MAUD program takes into account precisely the instrument broadening and, under the selected assumption of isotropic peak broadening as a function of reciprocal space, performs the separation of the lattice strain contribution to the broadening from the reduced crystallite size. Relative agreement factors R_{wp} and R_B are generally reported to determine the ability of the implemented structural model in accounting for the experimental data, which are unavoidably affected by statistical noise due to the limited time of pattern collection.

Transmission electronic microscopy (TEM) images were obtained with a JEM 200CX working at 200 kV; selected area diffraction images were obtained with a camera length of 82 cm.

The 488.0 nm line of a Spectra-Physics Stabilite 2017 argon Laser was used to excite the luminescence and Raman spectra. The emission radiation was collected by using an optical fiber and dispersed with a Jobin-Yvon HR460 0.46 m monochromator equipped with a 150 lines/mm (for low-resolution luminescence spectra) or a 1200 lines/mm (for high-resolution luminescence and Raman spectra) grating. A suitable notch filter was employed to measure the Raman spectrum, in order to suppress the 488.0 nm Rayleigh radiation. Due to the notch filter, the Raman spectrum can be collected for Raman shifts higher than 250 cm^{-1} . An air cooled Jobin-Yvon Spectrum One CCD device was employed to detect the emission radiation. The resolution of the luminescence spectra is $\pm 1 \text{ nm}$ for low-resolution luminescence spectra (560–730 nm range) and $\pm 0.2 \text{ nm}$ for high-resolution spectra (577–584 nm range). The spectral resolution of the Raman spectrum is $\pm 2 \text{ cm}^{-1}$. The emission decay curves were measured using as the excitation source the second harmonic (at 532 nm) of the fundamental radiation of a Quanta System pulsed Nd-YAG laser. The emission radiation was dispersed with the above mentioned monochromator and detected with a Hamamatsu GaAs photomultiplier connected to a Le Croy Waverunner 500 MHz digital oscilloscope. All the spectroscopic measurements were performed at room temperature.

3. RESULTS AND DISCUSSION

The X-ray diffraction pattern of the $\text{Nb}_2\text{O}_5\text{:Eu}$ sample is reported in Figure 1 as data points, together with the result of the Rietveld fit (full lines). It is possible to assess that the sample is single phase. The pattern is typical of an orthorhombic Nb_2O_5 structure, reported with space group $Pbam$ by Kato and Tamura [13]. The values of lattice parameters refined from the pattern (see Table 1) are not too different from the

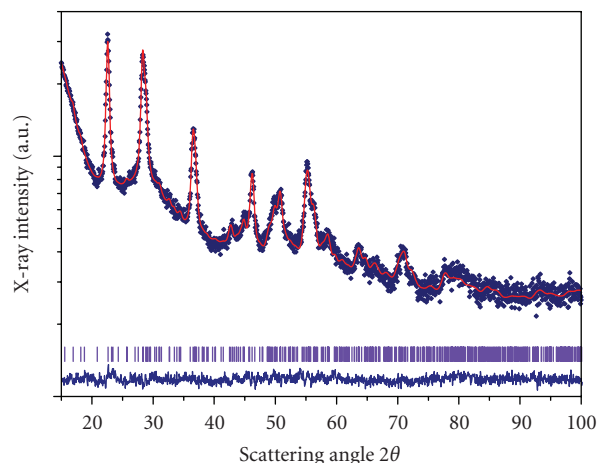


FIGURE 1: XRD patterns for the Eu^{3+} doped nanocrystalline Nb_2O_5 sample. Dots are experimental data points, full lines are the result of the Rietveld fit. The sequence of bars is calculated from the orthorhombic structure factor $Pbam$ with the lattice parameters reported in Table 1 and marks the positions expected for any peak. The band at the very bottom of the plot reports the residuals, that is, the difference between the square root of calculated and experimental intensities.

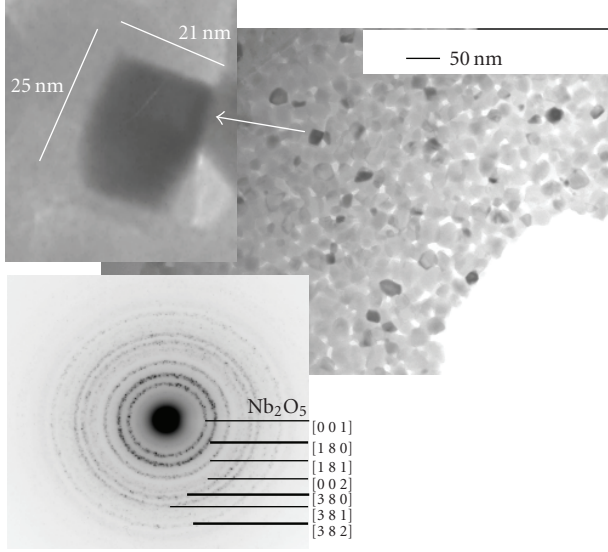
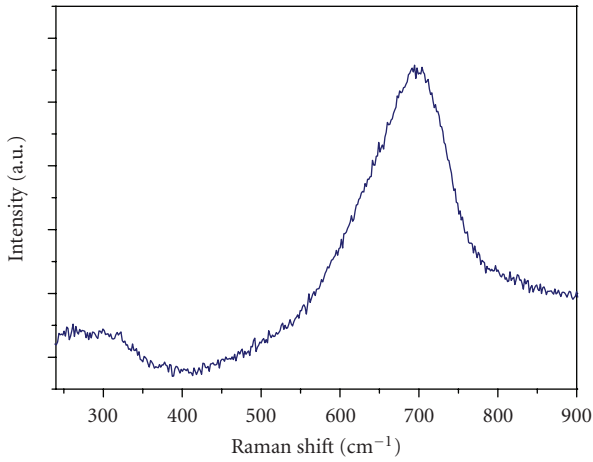
values reported by Kato and Tamura [13] from single crystal data and the small differences found may be ascribed to the insertion into the matrix of the doping agent here used. It should also be noted that various forms of the Nb(V) oxide are known from literature, namely tetragonal [14] and monoclinic [15]. Further, additional monoclinic forms exist, which are modified by pressure and temperature. The pattern of our orthorhombic $\text{Nb}_2\text{O}_5\text{:Eu}$ sample is in close agreement with that reported by Pinna et al. [16]. Direct evaluation of the line broadening by the Rietveld program MAUD, which includes the correction for the instrument function, gives an average crystallite size of about 25 nm with a sensible amount of lattice strain of 0.002.

The crystallography and morphology of the powder were also probed by selected Area electron Diffraction (SAD). In Figure 2(a), a TEM bright field image shows monodisperse rectangular nanoparticles with a narrow particle size distribution. The mean particle dimensions were determined by averaging over about one hundred particles. The average length and width were observed to be 26 and 19 nm, respectively. This result agrees with the size obtained from XRD with the Rietveld method and with the observations by Pinna et al. [16].

The Raman spectrum of the niobia sample under investigation is shown in Figure 3. A strong broad band peaking at about 700 cm^{-1} dominates the Raman spectrum although some weaker features around 300 cm^{-1} can be observed. The spectrum is very similar to the one found by Brayner and Bozon-Verduraz for a nanocrystalline orthorhombic Nb_2O_5 sample prepared by a soft chemical route [17]. The broad band around 700 cm^{-1} can be attributed to the stretching modes of the NbO_6 polyhedra typical of the orthorhombic

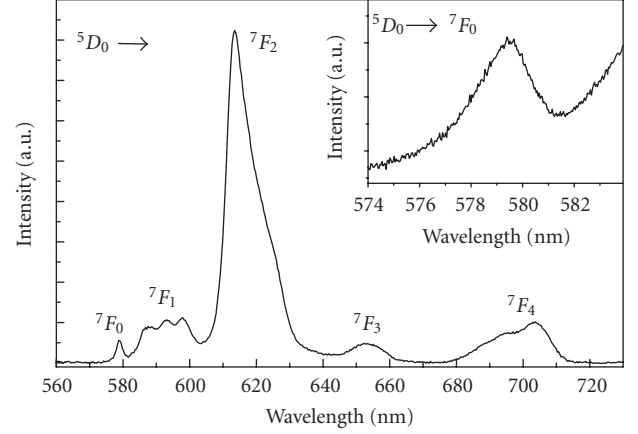
TABLE 1: The main crystallographic and microstructure parameters for the $\text{Nb}_2\text{O}_5:\text{Eu}$ sample from the best-fit data of Figure 1.

Geometry and space group	Lattice parameters (\AA)	Crystallite size (\AA)	Lattice strain ($\times 10^{-3}$)	Agreement index R_{wp}
Orthorhombic $Pbam$	a = 6.191 (± 2) b = 29.244 (± 5) c = 3.926 (± 2)	230 \pm 30	2.0 (± 0.2)	4.7 %

FIGURE 2: TEM and SAD images for the Eu^{3+} doped nanocrystalline Nb_2O_5 sample.FIGURE 3: Room temperature Raman spectrum of the Eu^{3+} doped nanocrystalline Nb_2O_5 sample.

Nb_2O_5 crystalline structure. The remarkable broadening of this band suggests the presence of distorted niobia polyhedra. Besides, the weaker bands around 300 cm^{-1} are characteristic of the bending modes of the Nb–O–Nb linkages [17].

The room temperature laser excited luminescence spectrum in the 560–730 nm region is shown in Figure 4. The spectrum is characterised by emission bands ascribed to

FIGURE 4: Room temperature luminescence spectrum of the Eu^{3+} doped nanocrystalline Nb_2O_5 sample ($\lambda_{\text{exc}} = 488.0\text{ nm}$). Inset: ${}^5D_0 \rightarrow {}^7F_0$ emission band.

${}^5D_0 \rightarrow {}^7F_J$ ($J = 0, 1, 2, 3, 4$) transitions. These bands appear to be significantly broadened, a behaviour typical of lanthanide impurities in disordered environments. It should be noted that the ${}^5D_0 \rightarrow {}^7F_0$ emission band of the Eu^{3+} ion (shown in the inset of Figure 4) is characterised by a full width at half maximum (FWHM) of $32 \pm 2\text{ cm}^{-1}$, which is much higher than for ordered crystalline materials, in agreement with the presence of a high degree of disorder for the Eu^{3+} sites in the Nb_2O_5 host. This FWHM value results to be even higher than the one observed for Eu^{3+} doped strontium barium niobate (SBN) single crystals (FWHM = 24 cm^{-1}) [6], which are among the crystals affected by a high degree of intrinsic disorder. Moreover, the FWHM for the $\text{Nb}_2\text{O}_5:\text{Eu}$ sample is very similar to that found for Eu^{3+} doped SBN nanocrystalline powders (FWHM of about 30 cm^{-1}) [18]. The presence of such disorder is attributed to the difference in the ionic radii in octahedral coordination for Nb^{5+} (78 pm) and for Eu^{3+} (108.7 pm) [19], so that the substitution of the dopant ion cannot easily occur without distortions, which are likely to be affected by a site-to-site variation. Moreover, the necessary charge compensation could also occur in a variety of different ways, giving rise to a distribution of possible sites for the Eu^{3+} ions.

The asymmetry ratio

$$R = \frac{I({}^5D_0 \rightarrow {}^7F_2)}{I({}^5D_0 \rightarrow {}^7F_1)} \quad (1)$$

of the integrated intensities of the hypersensitive ${}^5D_0 \rightarrow {}^7F_2$ and the magnetic dipole ${}^5D_0 \rightarrow {}^7F_1$ transitions can be considered indicative of the asymmetry of the coordination

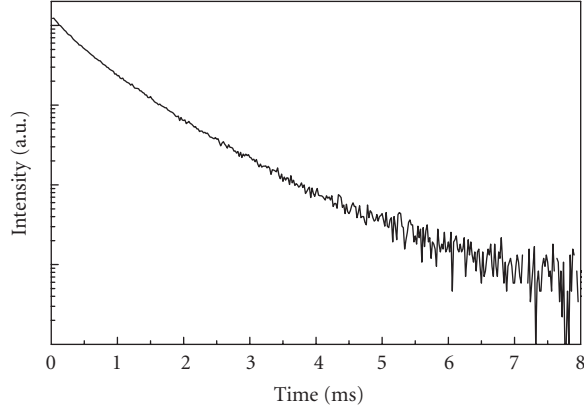


FIGURE 5: Room temperature luminescence decay curve of the Eu^{3+} doped nanocrystalline Nb_2O_5 sample ($\lambda_{\text{exc}} = 532 \text{ nm}$, $\lambda_{\text{em}} = 610 \text{ nm}$).

polyhedron of the Eu^{3+} ion [20]. In particular, the lower the R value is, the higher is the site symmetry at the Eu^{3+} ion. The value of the asymmetry parameter for the $\text{Nb}_2\text{O}_5:\text{Eu}$ sample, obtained from the measured emission spectra (see Figure 4), results to be 6.0 ± 0.1 . This value indicates that the Eu^{3+} ions are accommodated in noncentrosymmetric sites [20], in agreement with the fact that the forbidden transition is clearly detectable. This value appears to be on the upper side of the R range commonly found for Eu^{3+} doped glass hosts ($R = 3 - 6$) [20].

The RT emission decay curve of the 5D_0 level (see Figure 5) show a nonexponential behaviour. The nonexponential shape of the luminescence decay curve is mainly ascribed to the disorder affecting the sites in which the Eu^{3+} ions are accommodated, as also evidenced by the significant inhomogeneous broadening of the emission bands. We evaluate the effective average emission decay time τ_{avg} using the equation (see [21])

$$\tau_{\text{avg}} = \frac{\int tI(t)dt}{\int I(t)dt}, \quad (2)$$

where $I(t)$ represents the luminescence intensity at time t corrected for the background and the integrals are evaluated on a range $0 < t < t^{\text{max}}$, where $t^{\text{max}} \gg \tau_{\text{avg}}$. The obtained τ_{avg} value for the $\text{Nb}_2\text{O}_5:\text{Eu}$ sample is 0.78 ± 0.01 millisecond. This value of the effective decay time is similar to that found for SBN nanopowders (about 0.70 millisecond) [18]. The radiative lifetime τ_R of the 5D_0 level of the Eu^{3+} ion can be estimated using the formula (see [22])

$$\frac{1}{\tau_R} = A_{\text{MD},0} n^3 \left(\frac{I_{\text{tot}}}{I({}^5D_0 \rightarrow {}^7F_1)} \right), \quad (3)$$

where n is the refractive index of the medium, $A_{\text{MD},0}$ is the spontaneous emission probability for the ${}^5D_0 \rightarrow {}^7F_1$ transition in vacuo, and $I_{\text{tot}}/I({}^5D_0 \rightarrow {}^7F_1)$ is the ratio of the total area of the Eu^{3+} emission spectrum to the area of the ${}^5D_0 \rightarrow {}^7F_1$ band. The refractive index of the Nb_2O_5 host is taken as 2.4, as reported for Nb_2O_5 thin films [23, 24]. The

$A_{\text{MD},0}$ value is estimated to be 14.65 s^{-1} [22]. The radiative lifetime τ_R of the 5D_0 level of the Eu^{3+} ion, obtained from (3) and the measured emission spectrum (see Figure 4), results to be 0.56 millisecond. It is worth noting that the experimental effective lifetime τ_{avg} results to be longer than the radiative lifetime obtained from (3). The lengthening of the emission decay time of the 5D_0 level was also observed for some Eu^{3+} doped nanosized materials, such as Eu^{3+} doped Y_2O_3 nanopowders [25] and Eu^{3+} doped nanocrystalline zirconia [26]. This behavior can be due to a lower refractive index (n_{eff}) surrounding the Eu^{3+} ion in the nanocrystalline material with respect to the bulk size host, due to the fact that the filling factor (the fraction of the volume of the host occupied by the nanoparticles) is lower than one [25].

4. CONCLUSIONS

This work has shown that the synthesis of nanocrystalline niobia activated with Eu^{3+} ions is successfully achieved with the Pechini method. The obtained materials are single phase, with rectangular cross section nanoparticles of crystallite average length and width of 26 and 19 nm. Among the possible niobia polymorphs, the orthorhombic one with space group *Pbam* is observed. The luminescence features are affected by sizeable inhomogeneous broadening due to disorder around the dopant ions. The strongest emission band of the Eu^{3+} doped nanocrystalline Nb_2O_5 sample peaks at about 610 nm, suggesting a possible use of the present material as a red phosphor for lighting devices. In fact, the emission is quite efficient with reasonably long decay times, also due to the relatively low phonon cutoff of the niobia lattice (about 700 cm^{-1}), making nonradiative relaxation inefficient. Therefore, it appears justified concluding that nanocrystalline Nb_2O_5 activated with Eu^{3+} ions can be considered as an interesting and promising luminescent and multifunctional material. The present study shows that pentavalent niobium ions can be substituted by trivalent lanthanide ions in crystalline niobates. This substitution is accompanied by a strong disorder around the Ln^{3+} ions.

ACKNOWLEDGMENTS

The authors gratefully acknowledge Erica Viviani (DST, University of Verona) for expert technical assistance and H. C. Starck (GmbH) for kindly providing the niobium ammonium oxalate reagent. Thanks are also expressed to Dr. Luca Lutterotti (<http://www.ing.unitn.it/~luttero>) for making available a copy of the program MAUD running on a personal computer.

REFERENCES

- [1] D. Hreniak, W. Strek, A. Speghini, M. Bettinelli, G. Boulon, and Y. Guyot, "Infrared induced red luminescence of Eu^{3+} -doped polycrystalline LiNbO_3 ," *Applied Physics Letters*, vol. 88, Article ID 161118, 3 pages, 2006.
- [2] T. Imai, S. Yagi, H. Yamazaki, and M. Ono, "Effects of heat treatment on photorefractive sensitivity of Ce- and

- Eu-doped strontium barium niobate,” *Japanese Journal of Applied Physics*, vol. 38, no. 4A, part 1, pp. 1984–1988, 1999.
- [3] M. O. Ramirez, D. Jaque, L. E. Bausá, J. García-Solé, and A. A. Kaminskii, “Coherent light generation from a Nd:SBN non-linear laser crystal through its ferroelectric phase transition,” *Physical Review Letters*, vol. 95, no. 26, Article ID 267401, 4 pages, 2005.
- [4] A. Yoshikawa, H. Itagaki, T. Fukuda, et al., “Synthesis, crystal growth and second harmonic generation properties of trivalent rare-earth-doped non-linear tungsten-bronze-type structure $\text{Ba}_2\text{Na}_{1-3x}\text{RE}_x\text{Nb}_5\text{O}_{15}$ (RE = Sc, Y, La, Gd, Yb and Lu),” *Journal of Crystal Growth*, vol. 247, no. 1-2, pp. 148–156, 2003.
- [5] A. Lorenzo, H. Jaffrezic, B. Roux, G. Boulon, and J. García-Solé, “Lattice location of rare-earth ions in LiNbO_3 ,” *Applied Physics Letters*, vol. 67, no. 25, pp. 3735–3737, 1995.
- [6] M. Bettinelli, A. Speghini, A. Ródenas, et al., “Luminescence of lanthanide ions in strontium barium niobate,” *Journal of Luminescence*, vol. 122-123, pp. 307–310, 2007.
- [7] M. O. Ramirez, L. E. Bausá, A. Speghini, M. Bettinelli, L. Ivleva, and J. García-Solé, “Thermal hysteresis in the luminescence of Yb^{3+} ions in $\text{Sr}_{0.6}\text{Ba}_{0.4}\text{Nb}_2\text{O}_6$,” *Physical Review B*, vol. 73, no. 3, Article ID 035119, 8 pages, 2006.
- [8] O. Friedrichs, J. C. Sánchez-López, C. López-Cartes, T. Klassen, R. Bormann, and A. Fernández, “ Nb_2O_5 “pathway effect” on hydrogen sorption in Mg,” *Journal of Physical Chemistry B*, vol. 110, no. 15, pp. 7845–7850, 2006.
- [9] T. Hyodo, J. Ohoka, Y. Shimizu, and M. Egashira, “Design of anodically oxidized Nb_2O_5 films as a diode-type H_2 sensing material,” *Sensors and Actuators B*, vol. 117, no. 2, pp. 359–366, 2006.
- [10] M. Kakihana, ““Sol-gel” preparation of high temperature superconducting oxides,” *Journal of Sol-Gel Science and Technology*, vol. 6, no. 1, pp. 7–55, 1996.
- [11] H. M. Rietveld, “Line profiles of neutron powder-diffraction peaks for structure refinement,” *Acta Crystallographica*, vol. 22, part 1, pp. 151–152, 1967.
- [12] L. Lutterotti and S. Gialanella, “X-ray diffraction characterization of heavily deformed metallic specimens,” *Acta Materialia*, vol. 46, no. 1, pp. 101–110, 1998.
- [13] K. Kato and S. Tamura, “Die Kristallstruktur von $T - \text{Nb}_2\text{O}_5$,” *Acta Crystallographica B*, vol. 31, part 3, pp. 673–677, 1975.
- [14] W. Mertin, S. Andersson, and R. Gruehn, “Über die Kristallstruktur von $M - \text{Nb}_2\text{O}_5$,” *Journal of Solid State Chemistry*, vol. 1, no. 3-4, pp. 419–424, 1970.
- [15] K. Kato, “Structure refinement of $H - \text{Nb}_2\text{O}_5$,” *Acta Crystallographica B*, vol. 32, part 3, pp. 764–767, 1976.
- [16] N. Pinna, M. Antonietti, and M. Niederberger, “A novel non-aqueous route to V_2O_3 and Nb_2O_5 nanocrystals,” *Colloids and Surfaces A*, vol. 250, no. 1–3, pp. 211–213, 2004.
- [17] R. Brayner and F. Bozon-Verduraz, “Niobium pentoxide prepared by soft chemical routes: morphology, structure, defects and quantum size effect,” *Physical Chemistry Chemical Physics*, vol. 5, no. 7, pp. 1457–1466, 2003.
- [18] M. Daldosso, A. Speghini, P. Ghigna, et al., “Lanthanide doped strontium barium niobate: optical spectroscopy and local structure at the impurity sites,” to appear in *Journal of Alloys and Compounds*.
- [19] <http://www.webelements.com/>.
- [20] R. Reisfeld, E. Zigansky, and M. Gaft, “Europium probe for estimation of site symmetry in glass films, glasses and crystals,” *Molecular Physics*, vol. 102, no. 11-12, pp. 1319–1330, 2004.
- [21] E. Nakazawa, “Fundamentals of luminescence,” in *Phosphor Handbook*, S. Shionoya and W. M. Yen, Eds., p. 104, CRC Press, Boca Raton, Fla, USA, 1999.
- [22] M. H. V. Werts, R. T. F. Jukes, and J. W. Verhoeven, “The emission spectrum and the radiative lifetime of Eu^{3+} in luminescent lanthanide complexes,” *Physical Chemistry Chemical Physics*, vol. 4, no. 9, pp. 1542–1548, 2002.
- [23] K. Kukli, M. Ritala, M. Leskelä, and R. Lappalainen, “Niobium oxide thin films grown by atomic layer epitaxy,” *Chemical Vapor Deposition*, vol. 4, no. 1, pp. 29–34, 1998.
- [24] R. Romero, J. R. Ramos-Barrado, F. Martin, and D. Leinen, “ Nb_2O_5 thin films obtained by chemical spray pyrolysis,” *Surface and Interface Analysis*, vol. 36, no. 8, pp. 888–891, 2004.
- [25] R. S. Meltzer, S. P. Feofilov, B. Tissue, and H. B. Yuan, “Dependence of fluorescence lifetimes of $\text{Y}_2\text{O}_3:\text{Eu}^{3+}$ nanoparticles on the surrounding medium,” *Physical Review B*, vol. 60, no. 20, pp. R14012–R14015, 1999.
- [26] A. Speghini, M. Bettinelli, P. Riello, S. Bucella, and A. Benedetti, “Preparation, structural characterization, and luminescence properties of Eu^{3+} -doped nanocrystalline ZrO_2 ,” *Journal of Materials Research*, vol. 20, no. 10, pp. 2780–2791, 2005.

Research Article

Upconversion Properties of Nanocrystalline $\text{ZrO}_2\text{:Yb}^{3+}, \text{Er}^{3+}$ Phosphors

Iko Hyppänen,¹ Jorma Hölsä,¹ Jouko Kankare,¹ Mika Lastusaari,¹ and Laura Pihlgren^{1,2,3}

¹ Department of Chemistry, University of Turku, FI-20014 Turku, Finland

² Department of Biotechnology, University of Turku, Tykistökatu 6, FI-20520 Turku, Finland

³ Graduate School of Materials Research, Turku, Finland

Received 30 October 2007; Accepted 26 November 2007

Recommended by Wiesław Stręk

Combustion and sol-gel methods were used to prepare the upconverting nanocrystalline $\text{ZrO}_2\text{:Yb}^{3+}, \text{Er}^{3+}$ phosphors. The crystal structure was studied by X-ray powder diffraction and the crystallite sizes were estimated with the Scherrer formula. Impurities and nanomaterials' thermal degradation were analyzed with FT-IR spectroscopy and thermal analysis, respectively. Upconversion luminescence and luminescence decays were studied with IR-laser excitation at 977 nm. All nanomaterials possessed the cubic ZrO_2 fluorite-type structure except for a small monoclinic impurity obtained with the sol-gel method. The conventional NO_3^- and OH^- impurities were observed for the combustion synthesis products. The $\text{ZrO}_2\text{:Yb}_3, \text{Er}^{3+}$ nanomaterials showed red (630–710 nm) and green (510–570 nm) upconversion luminescence due to the $^4\text{F}_{9/2} \rightarrow ^4\text{I}_{15/2}$ and $(^2\text{H}_{11/2}, ^4\text{S}_{3/2}) \rightarrow ^4\text{I}_{15/2}$ transitions of Er^{3+} , respectively. The products of the combustion synthesis exhibited the most intense luminescence intensity and showed considerable afterglow. It was concluded that excitation energy is partially trapped in the system and subsequently bleached thermally to the luminescent Er^{3+} center to yield "persistent upconversion".

Copyright © 2007 Iko Hyppänen et al. This is an open access article distributed under the Creative Commons Attribution License, which permits unrestricted use, distribution, and reproduction in any medium, provided the original work is properly cited.

1. INTRODUCTION

One of the most sophisticated and, at the same time, the most complex applications of lanthanide luminescence is in the medical diagnostics [1]. However, there are some major problems in the use of photoluminescence based on the UV excitation in immunoassays [2]. Human blood absorbs strongly UV radiation as well as the emission of the phosphor in the visible [3]. The observation of luminescence from the lanthanide labels is thus basically disadvantageous. One of the usual ways of overcoming this problem has been the application of long-lifetime lanthanide labels (e.g., those based on terbium and europium). However, the use of these Tb^{3+} - or Eu^{3+} -based lanthanide labels in the whole-blood immunoassays is still difficult because the Tb^{3+} luminescence (maximum emission at 545 nm) is in the same wavelength region as the blood absorption (<600 nm). The Eu^{3+} luminescence (maximum at 615–620 nm) is also slightly overlapping with the blood absorption. Persistent luminescence is a useful method to solve the blood emission problem if the UV excitation is used [4]. Persistent luminescence can be visible for several hours after the excitation has been ceased while

the luminescence lifetime of the blood is in the ns range. Although most persistent luminescence materials emit in green or blue strongly absorbed by blood, some persistent luminescence emitters in the red are known (e.g., Mn^{2+}) [5, 6]. However, the Mn^{2+} ion needs a sensitizer (usually Eu^{2+}) which absorbs the exciting radiation. The upconversion luminescence where the absorption of two or more low-energy photons is followed by the emission of a photon of higher energy has witnessed numerous breakthroughs during the past decades. Upconverting phosphors have a variety of potential applications as lasers, displays, and inks for security printing (e.g., bank notes and bonds) [7–9]. In addition, another promising way to overcome the problems with the blood absorption is to use a long-wavelength excitation and benefit the upconversion luminescence [10]. There is practically no absorption by the whole-blood in the near IR region and it has no capability for upconversion in the excitation wavelength region of the conventional upconverting phosphor based on the Yb^{3+} (sensitizer) and Er^{3+} (activator) combination. It is also possible to find a red emitting ion (Er^{3+}).

For coupling to biological compounds, nanometer-sized upconverting phosphor particles are required. Moreover,

nanophosphors with high luminescent efficiency are vital in the development of novel homogeneous label technology for quantitative all-in-one whole-blood immunoassay which uses low-cost measurement devices [11].

In this work, nanocrystalline upconverting phosphors with zirconium oxide (zirconia, ZrO_2) as the host lattice were prepared. The local environment, the dopant concentration, and the distribution of active ions in the host material affect the upconversion efficiency [12, 13]. Taking into account these requirements (among others), zirconia offers a very appropriate medium for the preparation of highly luminescent materials because it is chemically and photochemically stable, and has a high refractive index (2.15–2.18) and a low phonon energy. The stretching frequency of the Zr–O bond is about 470 cm^{-1} , which is much lower than for Al–O (870) or Si–O (1100) but higher than for Y–O (300–380 cm^{-1}) [12].

In the zirconia host, the lanthanide dopants possess multistate positions that improve the absorption efficiency and potentially enhance the resonant energy transfer from the sensitizer (Yb^{3+}) to the activator (Er^{3+}). The $ZrO_2:Yb^{3+},Er^{3+}$ nanophosphors were obtained with several soft chemistry methods and the possible impurities were studied mainly with FT-IR spectroscopy. Materials' preparation and thermal degradation were studied with thermal analysis (TG, DTA). Crystal structures and phase purities were analyzed with X-ray powder diffraction (XPD). Upconversion luminescence and decays were obtained at room temperature with NIR excitation. A comparison was made between the luminescence intensities and the crystallite size, the crystal structure, as well as the impurities of the phosphors. Finally, a new phenomenon, persistent upconversion luminescence was introduced and discussed.

2. EXPERIMENTAL

The $ZrO_2:Yb^{3+},Er^{3+}$ nanomaterials were prepared with the combustion [14] and sol-gel methods [15]. The synthesis affects the type and amount of impurities as well as the crystallite size, which in turn has a profound influence on the upconversion luminescence intensity. Accordingly, the method of preparation should be chosen carefully taking into account both the crystallite size as well as the intensity and color of luminescence of the nanomaterial. This may lead to quite difficult tradeoffs.

The precursor materials of $ZrO_2:Yb^{3+},Er^{3+}$ prepared with the combustion synthesis were the aqueous solutions of zirconyl nitrate ($ZrO(NO_3)_2$) as well as ytterbium and erbium nitrates ($Yb(NO_3)_3$ and $Er(NO_3)_3$, resp.). The nominal concentrations of Yb^{3+} (99.9%) and Er^{3+} (99.99%) were ten and four mole-%, respectively, of the Zr^{IV} amount. Glycine (NH_2CH_2COOH), semicarbazide ($H_2NCONHNH_2 \cdot HCl$), urea ($(NH_2)_2CO$), citric acid ($HOC(COOH)(CH_2COOH)_2$), or 2-amino-2-methyl-1,3-propanediol (AMP, $(HOCH_2)_2C(NH_2)CH_3$) served as the fuel. Additional ammonium nitrate (NH_4NO_3) was used as an oxidizer with selected fuels. The combustion reaction was carried out in a glass reactor using a weak upward air flow.

Some of the products were postannealed in air at 700°C for 1 hour if the material's crystallinity was poor.

The $ZrO_2:Yb^{3+},Er^{3+}$ nanomaterials obtained with the sol-gel method had the zirconium-*n*-propoxide as a precursor to which the aqueous ytterbium and erbium nitrate solutions were added. After gelation, the materials were dried and annealed for 3 or 6 hours at 400°C and for 10 or 20 hours at 1000°C in static air in a ceramic crucible with a lid.

The FT-IR spectra between 400 and 4000 cm^{-1} were measured with a Mattson Instruments GALAXY 6030 spectrometer with a 4 cm^{-1} resolution. The materials were mixed with KBr and then pressed to transparent discs.

The TG and DTA curves between 25 and 1200°C were measured in flowing air ($100\text{ cm}^3\text{ min}^{-1}$) with a TA instruments SDT 2960 Simultaneous DTA-TGA thermoanalyzer with a heating rate of 5°C min^{-1} . $\alpha\text{-Al}_2\text{O}_3$ was used as both the reference and crucible material.

The crystal structure and phase purity of the $ZrO_2:Yb^{3+},Er^{3+}$ nanomaterials were analyzed with the X-ray powder diffraction (XPD) measurements. The patterns were collected with a Huber 670 image plate (2θ range: $4\text{--}100^\circ$) Guinier-camera ($\text{CuK}\alpha_1$ radiation: 1.5406 \AA).

The crystallite size of each $ZrO_2:Yb^{3+},Er^{3+}$ nanomaterial was estimated from the diffraction data by using the Scherrer formula [16]

$$d = \frac{0.9 \times \lambda}{\beta \times \cos \theta}, \quad (1)$$

where, in this formula, d (m) is the mean crystallite size, λ (m) the X-ray wavelength, β (rad) the full width at half maximum (FWHM) of the [111] reflection ($2\theta = 30.2^\circ$), and θ ($^\circ$) half of the Bragg's angle (2θ). The reflection broadening due to the diffractometer setup was eliminated from the β_s -value by using a microcrystalline ZrO_2 reference (β_r):

$$\beta^2 = \beta_s^2 - \beta_r^2. \quad (2)$$

The upconversion luminescence spectra of the nanomaterials were measured at room temperature with an Ocean Optics PC2000-CCD spectrometer. The excitation ($\lambda_{\text{exc}} = 977\text{ nm}$) source was an HTOE FLMM-0980-711-1300m IR laser diode. The decay curves were measured with the same excitation source at 650 nm . The width of the excitation pulse was 1 millisecond. After each pulse there was a 9-millisecond delay before the next pulse. One measurement consisted of 1000 pulse-delay cycles.

3. RESULTS AND DISCUSSION

3.1. Material impurities

The FT-IR spectra of the $ZrO_2:Yb^{3+},Er^{3+}$ nanomaterials revealed the presence of the conventional impurities (NO_3^- , OH^-) in the materials prepared by the combustion synthesis (see Figure 1). The amount of these impurities depended on the fuel used; the highest amount of impurities was observed when urea was used as a fuel. The organic compounds (fuels) were mainly decomposed to CO_2 , H_2O , and NO_x , but it is possible that the nanomaterials contain also some carbon residue since the ZrO_2 nanomaterials prepared with the

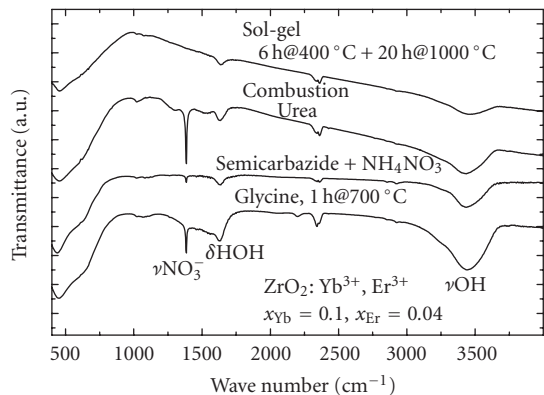


FIGURE 1: FT-IR spectra of selected $\text{ZrO}_2:\text{Yb}^{3+},\text{Er}^{3+}$ nanomaterials prepared with the combustion synthesis.

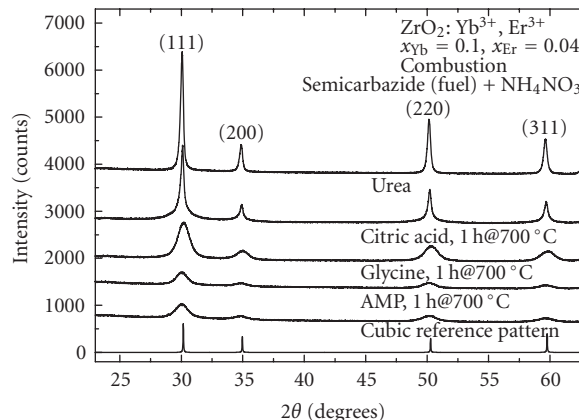


FIGURE 3: XPD patterns of selected $\text{ZrO}_2:\text{Yb}^{3+},\text{Er}^{3+}$ nanomaterials prepared with the combustion synthesis.

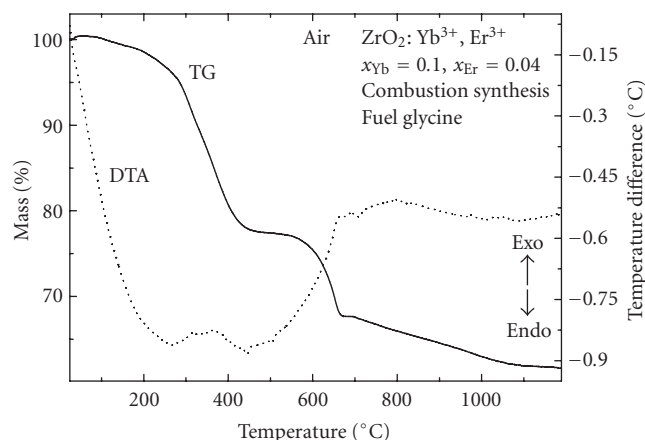


FIGURE 2: TG and DTA curves of the $\text{ZrO}_2:\text{Yb}^{3+},\text{Er}^{3+}$ nanomaterial prepared by the combustion synthesis (glycine as the fuel).

combustion method were generally brown, whereas the body color of pure ZrO_2 is white. On the other hand, as to be discussed later in more detail, the substitution of Zr^{IV} with $\text{Yb}^{3+}/\text{Er}^{3+}$ creates oxygen vacancies which may act as color centers, absorb in the visible, and cause the brownish color. No such impurities were observed in the $\text{ZrO}_2:\text{Yb}^{3+},\text{Er}^{3+}$ nanomaterials prepared with the sol-gel method though it is evident that moisture was present in these materials. The amount of moisture (or OH^- groups) was greatly diminished by postannealing at 1100°C .

The stretching frequency of the $\text{Zr}-\text{O}$ -bond is about 450 cm^{-1} (see Figure 1) which is in agreement with the literature value [12]. The $\text{Yb}-\text{O}$ (or $\text{Er}-\text{O}$) vibrations could not be observed with the present experimental setup.

3.2. Thermal degradation

The TG curve of the $\text{ZrO}_2:\text{Yb}^{3+},\text{Er}^{3+}$ nanomaterial, prepared with the combustion method, showed the decomposition of nitrates at $250\text{--}450^\circ\text{C}$ (see Figure 2). No moisture was present because no low-temperature weight loss was ob-

served below 200°C . With glycine used as the fuel, a further mass change was observed between 500 and 650°C . This change is due to the decomposition of zirconium oxycarbonates/oxynitrates which are surprisingly stable to high temperatures as are the corresponding rare earth oxycarbonates/oxynitrates [17, 18]. The exothermic signal in the DTA curve around 700°C can be related to the appearance of a crystalline phase of $\text{ZrO}_2:\text{Yb}^{3+},\text{Er}^{3+}$ as indicated by the XPD patterns. The gradual weight loss at higher temperatures can be taken as an indication of evaporation of tightly bound species, for example, OH^- groups (as water). The presence of these impurities may have a nefarious effect on the luminescence performance of these nanomaterials.

The TG curve of the material prepared with the sol-gel method showed a practically constant weight. No signals were observed in the DTA curve either.

3.3. Crystal structure and crystallite sizes

The XPD measurements revealed that the structure of the $\text{ZrO}_2:\text{Yb}^{3+},\text{Er}^{3+}$ nanomaterials was that of the typical cubic yttria stabilized zirconia (the cubic YSZ phase: space group $\text{Fm}\bar{3}\text{m}$, no. 225, $Z = 4$) [19]. The nanomaterials, prepared with the combustion synthesis (see Figure 3), were essentially pure, whereas small amounts of the monoclinic zirconia phase ($\text{P}2_1/\text{a}$, no. 14, $Z = 4$) [19] as an impurity was found in the materials prepared with the sol-gel method (see Figure 4). The presence of the monoclinic phase is probably due to the partial segregation of $\text{ZrO}_2:\text{Yb}^{3+},\text{Er}^{3+}$ to the individual ZrO_2 and $(\text{Yb},\text{Er})_2\text{O}_3$ phases since very weak reflections belonging to R_2O_3 were noticed in the XPD patterns. The crystallite sizes estimated with the Scherrer equation [16] were $5\text{--}30$ and ca. 50 nm for materials prepared with the combustion synthesis and the sol-gel method, respectively.

3.4. Upconversion luminescence

The excitation process for the upconversion emission of Er^{3+} ions (see Figure 5) under infrared excitation ($\lambda_{\text{exc}} = 977\text{ nm}$)

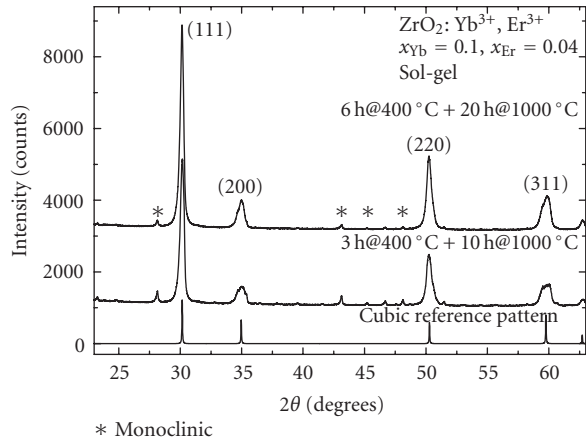


FIGURE 4: XPD patterns of selected $\text{ZrO}_2:\text{Yb}^{3+}, \text{Er}^{3+}$ nanomaterials prepared with the sol-gel method.

has been well established in the literature, for example, [20–22]. Though this mechanism is well known, in view of the phenomenon described later on, it is presented here as well. The first photon of near-infrared (NIR) radiation excites the Yb^{3+} ion to the sole excited $^2\text{F}_{5/2}$ level from which the excitation may relax radiatively back to the ground $^2\text{F}_{7/2}$ level. Taken into account the long radiative life time of the excited $^2\text{F}_{5/2}$ level (typically 1 millisecond), the Yb^{3+} ion may transfer well the excitation energy to an Er^{3+} ion with higher probability than decaying radiatively. The Er^{3+} ion is first promoted to the $^4\text{I}_{11/2}$ level, and further to $^4\text{F}_{7/2}$ due to absorption and energy transfer of another NIR photon. Then Er^{3+} decays rapidly and nonradiatively to the $^2\text{H}_{11/2}$, $^4\text{S}_{3/2}$ or $^4\text{F}_{9/2}$ (or lower) levels. The upconversion emission is customarily assigned to the following transitions: green emission in the 510–570 nm region to the $(^2\text{H}_{11/2}, ^4\text{S}_{3/2}) \rightarrow ^4\text{I}_{15/2}$ transitions; and red emission in the 630–710 nm region to the $^4\text{F}_{9/2} \rightarrow ^4\text{I}_{15/2}$ transitions of the Er^{3+} ion. It should be noted that other pathways (including the initial ground-state absorption (GSA) and further excited-state absorption (ESA)) may be possible involving the Er^{3+} ions only, though their probabilities are low, partly due to the low Er^{3+} concentration.

In the ZrO_2 matrix, the luminescence transitions are rather broad and without evident crystal field fine structure. This observation is in agreement with the multisite positions occupied by the trivalent Yb^{3+} and Er^{3+} ions. This is due to the lack of any trivalent ion site in the ZrO_2 structure and the creation of oxide vacancies (Kröger-Vink notation: $\text{V}_{\text{O}}^{\bullet\bullet}$) results from the Yb^{3+} and Er^{3+} ions occupying the tetravalent Zr^{IV} site (Yb_{Zr} or Er_{Zr}) in the cubic fluorite type structure. At least three different sites with different point symmetries due to the different position of the oxide vacancies around the R^{3+} ion have been found for the $\text{ZrO}_2:\text{Y}^{3+}, \text{Eu}^{3+}$ system with the use of optical site selective excitation techniques [23] and EXAFS measurements [24]. Moreover, the inhomogeneous broadening of the Eu^{3+} emission lines was taken as an indication of a relaxation of the oxide sublattice towards the oxide vacancies creating a number of sites with rather similar point

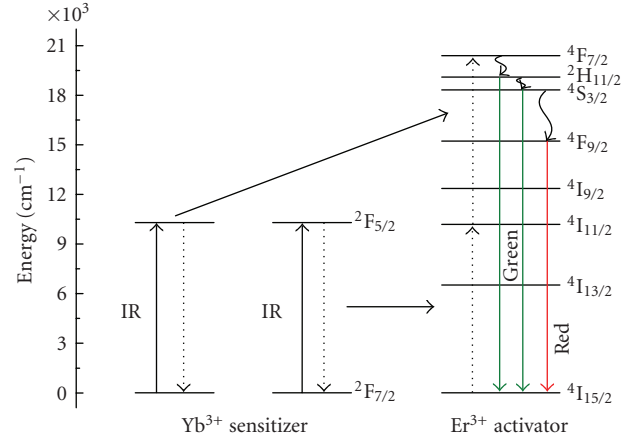
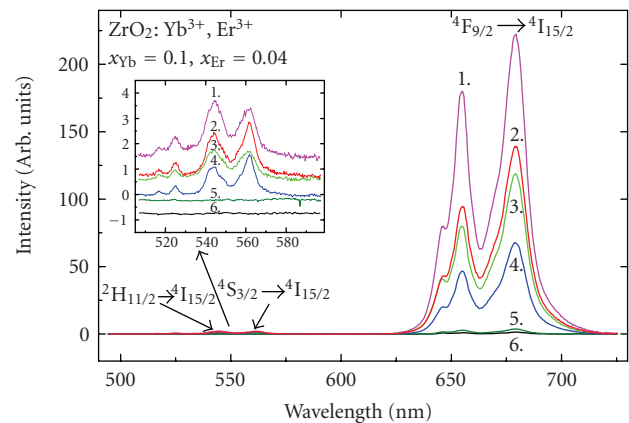


FIGURE 5: Schematic diagram of the Yb^{3+} sensitized Er^{3+} upconversion luminescence.



1. Semicarbazide + NH_4NO_3
2. Sol-gel, 6 h @ 400 °C + 20 h @ 1000 °C
3. Urea
4. Sol-gel, 3 h @ 400 °C + 10 h @ 1000 °C
5. AMP
6. Glycine, 1 h @ 700 °C

FIGURE 6: Upconversion luminescence spectra of selected $\text{ZrO}_2:\text{Yb}^{3+}, \text{Er}^{3+}$ nanomaterials.

symmetries. There is no doubt that similar charge compensation schemes are present in the $\text{ZrO}_2:\text{Yb}^{3+}, \text{Er}^{3+}$ nanomaterials because of the similar size of the Yb^{3+} and Y^{3+} dopants when compared to Zr^{IV} .

The highest luminescence intensity was obtained from the $\text{ZrO}_2:\text{Yb}^{3+}, \text{Er}^{3+}$ nanomaterials obtained with the combustion synthesis with semicarbazide used as the fuel (see Figure 6). This is due to the structurally pure (cubic) material, whereas the material prepared with the sol-gel method was a mixture of both the cubic and monoclinic forms. The difference between the luminescence intensities might also be due to the different surrounding microdomains of the Yb^{3+} and Er^{3+} ions, and due to other impurities.

The heating of the nanomaterial prepared with the combustion synthesis at 1100 °C for 2 hours did not increase

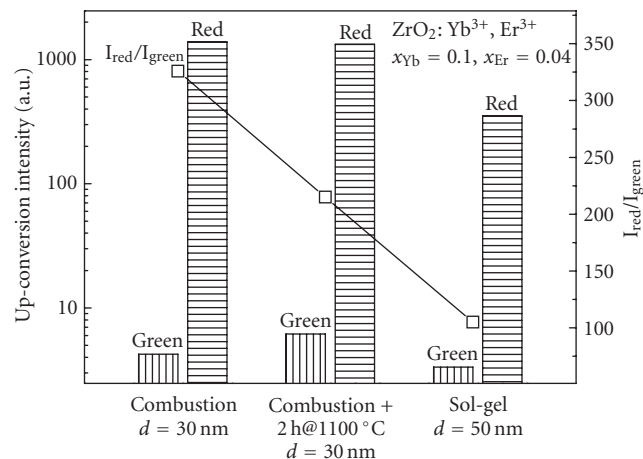


FIGURE 7: Upconversion luminescence intensities of selected ZrO₂:Yb³⁺,Er³⁺ nanomaterials.

the crystallite size. This might be due to a too low heating temperature and/or too short heating time. Because of the equal crystallite sizes, the luminescence intensities of the both materials prepared with the combustion synthesis were also quite equal.

The ZrO₂:Yb³⁺,Er³⁺ nanomaterials exhibit a very high $I_{\text{red}}/I_{\text{green}}$ ratio (note the logarithmic y-scale in Figure 7) compared to other host materials (e.g., NaYF₄) [25]. This is due to the very low intensity of the green luminescence. In the ZrO₂ host, there are three main reasons for the weak green luminescence: the multiphonon relaxation, the cross-relaxation, and trapping of excitation energy by lattice defects. The prerequisites for efficient multiphonon relaxation are an energy level close below the luminescent level and/or high-energy phonon(s). The energy difference between the ⁴S_{3/2} (²H_{11/2}) levels yielding the green luminescence and the next lower level (⁴F_{9/2}) is ca. 3000 cm⁻¹ (ca. 3700). The Zr–O phonon energy is 470 cm⁻¹ [12] and the Er–O energy is approximately the same. In pure materials, the multiphonon relaxation process is not probable because too many (six or seven) lattice phonons are needed to quench the green luminescence. However, when the crystallite size is smaller, there exist impurities (e.g., NO₃⁻, OH⁻) on the large surface area to facilitate the quenching. The surface itself may act as a quenching center too. The probability of the multiphonon relaxation is increased because the impurities have higher phonon energies (up to 1500 and 3500 cm⁻¹ for NO₃⁻ and OH⁻) and thus less phonons (one or two) are needed for quenching. Finally, the multiphonon relaxation of the green luminescence enhances the intensity of the red luminescence by populating the ⁴F_{9/2} level.

The energy difference between the ⁴F_{9/2} level yielding the red luminescent and the next lower ⁴I_{9/2} level is also ca. 3000 cm⁻¹. The probability for the multiphonon relaxation of the red luminescence should be comparable to that of the green one. However, the red emission is much stronger and thus the multiphonon relaxation seems to be inefficient in this case. Finally, it should be noted that both the green and red luminescence of the ZrO₂:Yb³⁺,Er³⁺ nanomaterials are

rather weak when compared to other host lattices studied (e.g., NaYF₄ and Y₂O₂S) [25]. The multiphonon relaxation processes can thus explain the weakness of the *total* but not the individual green luminescence alone.

The second process that may affect the luminescence intensities is cross-relaxation. There may be three possible cross-relaxation processes resulting in the quenching of the green luminescence. First of all, the quenching of the green emission from ⁴S_{3/2} proceeds via the thermally activated ²H_{11/2} level. The first process involves the ²H_{11/2} → ⁴I_{13/2} relaxation and the ⁴I_{9/2} ← ⁴I_{15/2} excitation; the energy being ca. 12500 cm⁻¹. In the second possible cross-relaxation process, there are coupled the ²H_{11/2} → ⁴I_{9/2} relaxation and the ⁴I_{13/2} ← ⁴I_{15/2} excitation [13]. The energy difference related to these processes is ca. 6700 cm⁻¹. It has been claimed that the two cross-relaxation mechanisms are experimentally indistinguishable [26]. The two cross-relaxation processes are competing with the green luminescence, with the multiphonon relaxation, with each other, and also with the trapping of energy. There are no known cross-relaxation processes for the red luminescence of Er³⁺ because of the lack of appropriate energy levels.

The third cross-relaxation process involves the higher excited ⁴F_{7/2} level of Er³⁺ which relaxes to the red emitting ⁴F_{9/2} level bypassing the green emitting levels [27]. The energy balance (ca. 5000 cm⁻¹) is conserved by the excitation of Er³⁺ to the ⁴F_{9/2} level from the ⁴I_{11/2} level which is populated due to the NIR laser pumping. Indeed, this process would favor the red emission.

The cross-relaxation processes of Er³⁺ is naturally favored by the rather high erbium concentration in the ZrO₂:Yb³⁺,Er³⁺ nanomaterials (nominally four mole-%) because then the erbium ions can locate near each other. As a special feature in the zirconia host, the Er³⁺ ions can form pairs with the aid of the oxide vacancy, that is, Er³⁺–V_O^{••}–Er³⁺ (cf. above). In addition to the intraion cross-relaxation processes, the interion ones can thus occur more easily between the Er³⁺ ions and decrease the intensity of the green luminescence.

The very weak green luminescence can thus be explained with both the multiphonon and the cross-relaxation processes but the strong red luminescence only with one of the cross-relaxation processes. However, in order to judge the relative probabilities of these processes, much more detailed spectroscopic work is needed. At the moment, this is out of the scope of the present work.

The energy trapping caused by the oxygen vacancies (cf. the discussion about the color centers above and Section 3.5) is also a competing process with the multiphonon and cross-relaxation processes. The total luminescence intensity can be quenched due to the absorption of the excitation energy but it may also affect the relative intensities of the green and red luminescence.

3.5. Upconversion luminescence decay

The study of the dynamics of the Er³⁺ red upconversion luminescence from the ZrO₂:Yb³⁺,Er³⁺ nanomaterials was

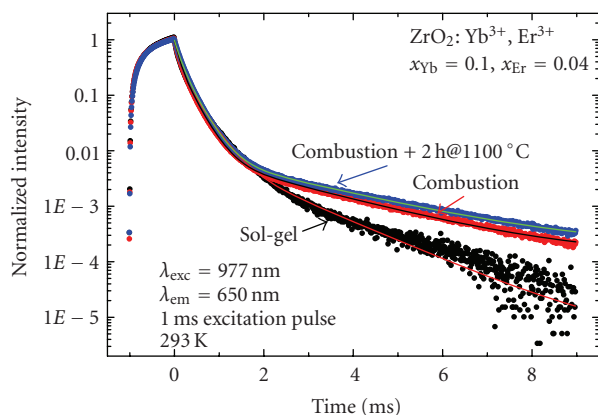


FIGURE 8: Upconversion luminescence decay curves of selected $\text{ZrO}_2:\text{Yb}^{3+},\text{Er}^{3+}$ nanomaterials.

decided to be carried out in two phases: first the feeding processes taking place before (or simultaneously to) the Er^{3+} luminescence; then the decay characteristics of the proper luminescence were examined in detail. It is evident with the first glance at Figure 8, however, that the preluminescence period was too complex and contained too few pieces of information to be exploited to yield reliable results. It should, nevertheless, be noted that the upconversion luminescence feeding time is very long (more than 1 millisecond). It can be deduced in a semiquantitative manner that the Yb^{3+} to Er^{3+} energy transfer is not exceedingly efficient since the other processes involved in the upconversion (absorption by Yb^{3+} (and Er^{3+}) and relaxation from the higher Er^{3+} levels to the emitting $^4\text{F}_{9/2}$ level) should take only a fraction of time when compared to the customary one-millisecond decay time of Yb^{3+} . The probability of the Yb^{3+} – Er^{3+} energy transfer can be deduced to be of the same order of magnitude as the emission from Yb^{3+} . This is supported by the luminescence feeding curve which barely achieves the saturation point during the one-millisecond excitation pulse. The Yb^{3+} -to- Er^{3+} energy transfer seems to be the rate determining step in the excitation process and thus the time to reach the saturation can give some information about the probability of the energy transfer process.

The second part of the decay kinetics proved to be as complex as the first part. However, due to a more expanded time scale, some quantitative measurements and calculations could be accomplished. The fitting of the red upconversion luminescence decay curves, clearly multiexponential or even more complicated, could be carried out to individual exponential components in the linear part of the curves immediately after the influence of the feeding processes had ceased. The results of these calculations showed that there are at least two different luminescence lifetimes in a range from ca. 100 to ca. 300 microseconds. These values are quite typical for the regular red Er^{3+} luminescence [27] and the number of different decay times is consistent with the multisite positions occupied by the Er^{3+} ion. The decay curves show also that there is no significant difference between the different

preparation methods when the shorter lifetimes are considered. Nevertheless, there is a significant difference in the *long* lifetimes of the nanomaterials prepared with different methods. For the $\text{ZrO}_2:\text{Yb}^{3+},\text{Er}^{3+}$ nanomaterials prepared with the combustion synthesis (and subsequently heated at 1100°C for 2 hours), there was observed severe afterglow. The total length of this afterglow could not be measured because of the experimental setup but it will definitely extend to several tens of milliseconds. This afterglow was hardly observed by the naked eye adapted to darkness and thus does not fulfill the requirements of the term “persistent luminescence” in the strictest meaning of the definition (light observed at the illumination level of 0.32 mcd m^{-2}). However, it should be noted that the $\text{ZrO}_2:\text{Yb}^{3+},\text{Er}^{3+}$ nanomaterials for which this afterglow was observed were not optimized for this effects, for example, by adding agents to create lattice defects. The intense and long upconversion luminescence indicates that there occurs trapping of the excitation energy in the system followed by thermal bleaching of this energy and feeding to a luminescence center. In that sense, this emission can be called as “persistent upconversion luminescence”.

As for the mechanism(s) of this persistent upconversion, there are two main possibilities: the trapping of the excitation energy can take place either after the absorption by Yb^{3+} (the sensitizer) or after the final excitation processes by Er^{3+} (the activator). The slightly more probable choice is the energy storage in the vicinity of Yb^{3+} since the decay time of Yb^{3+} is 3 to 10 times that of Er^{3+} . As a further proof to the existence of persistent luminescence for either Yb^{3+} - or Er^{3+} -doped materials, one can find experimental data for (strong) afterglow from Yb^{3+} -doped garnets [28, 29], Er^{3+} -doped silicon, and oxysulfides [28, 30, 31]. It can be thus assumed, though not yet proved, that the persistent upconversion in the $\text{ZrO}_2:\text{Yb}^{3+},\text{Er}^{3+}$ nanomaterials is possible. The resolution of the exact mechanism(s) requires further work, however.

Even without further studies, it is clear that there are vacancies (together with other impurities, e.g., OH^- groups) present in the $\text{ZrO}_2:\text{Yb}^{3+},\text{Er}^{3+}$ nanomaterials both due to the size and charge mismatch between the trivalent Yb^{3+} (and Er^{3+}) and the tetravalent Zr^{IV} ions as well as to the soft chemistry preparation methods used. Similar defects are known to store energy in the persistent luminescence materials (such as Eu^{2+} -doped alkaline earth aluminates and silicates) [32] as well as in the photostimulated materials (such as Eu^{2+} -doped $\text{BaF}(\text{Cl},\text{Br})$) [33]. In the case of the $\text{ZrO}_2:\text{Yb}^{3+},\text{Er}^{3+}$ nanomaterials, the depths of these traps are compatible with the thermal energy (kT) at room temperature and thus the feeding from the traps can occur.

The probability of trapping the excitation energy can be assumed to be a few orders of magnitude lower than the energy transfer to Er^{3+} or the emission of the Yb^{3+} ion. This can, however, be improved by careful engineering of these materials, as has been done with the alkaline earth aluminates and silicates. It can be assumed that the major advantages of combining the persistent luminescence and IR upconversion are that it can lead to efficient immunoassay materials.

4. CONCLUSIONS

The combustion method was found to be an efficient way to prepare the nanocrystalline upconverting $\text{ZrO}_2:\text{Yb}^{3+},\text{Er}^{3+}$ luminescence materials with the cubic ZrO_2 structure. The sol-gel method yielded a mixed product with slightly larger crystallite sizes, however. All materials showed rather efficient red upconversion luminescence with broad features due to multiple Er^{3+} sites originating from different charge compensation schemes because of aliovalent substitution of Zr^{IV} with R^{3+} . As a result of the structural purity, the combustion route yielded products with the highest luminescence intensity. The red/green intensity ratio was found to increase with the decreasing crystallite size due to the weakening of the green luminescence. This may be due to a very complex relaxation process involving the multiphonon, cross-relaxation, as well as energy trapping caused by lattice defects. Only one of several cross-relaxation processes can explain at the same time the weak green and strong red luminescence, however. This process must thus be considered as the dominating relaxation process of the green luminescence.

The luminescence decay characteristics with at least two different lifetimes in the range typical of red Er^{3+} luminescence agreed with the multisite nature of the ZrO_2 lattice. The materials obtained with different methods showed considerable differences in the longer lifetimes. Moreover, severe afterglow, that is, persistent upconversion luminescence, was observed for the products of the combustion route indicating the inherent energy storage capability of the $\text{ZrO}_2:\text{Yb}^{3+},\text{Er}^{3+}$ materials.

For efficient use in bioassays, more work is needed to yield nanomaterials with smaller and more uniform crystallite sizes. Surface modifications need to be studied to allow for the dispersion in aqueous solutions. On the other hand, further work must be carried out to optimize the persistent luminescence of the $\text{ZrO}_2:\text{Yb}^{3+},\text{Er}^{3+}$ nanomaterials to allow for their use as efficient immunoassay nanomaterials combining the advantages of both upconversion and persistent luminescence.

ACKNOWLEDGMENTS

Financial supports from the Finnish Funding Agency for Technology and Innovation (Tekes) and the Graduate School of Materials Research (Turku, Finland) for L. Pihlgren and from the Graduate School of Chemical Sensors and Microanalytical Systems (Espoo, Finland) for I. Hyppänen are gratefully acknowledged.

REFERENCES

- [1] S. N. Misra, M. A. Gagnani, I. Devi, and R. S. Shukla, "Biological and clinical aspects of lanthanide coordination compounds," *Bioinorganic Chemistry and Applications*, vol. 2, no. 3-4, pp. 155-192, 2004.
- [2] G. Mathis, "Rare earth cryptates and homogeneous fluorimmunoassays with human sera," *Clinical Chemistry*, vol. 39, no. 9, pp. 1953-1959, 1993.

- [3] W. G. Zijlstra, A. Buursma, and W. P. Meeuwse-van der Roest, "Absorption spectra of human fetal and adult oxyhemoglobin, de-oxyhemoglobin, carboxyhemoglobin, and methemoglobin," *Clinical Chemistry*, vol. 37, no. 9, pp. 1633-1638, 1991.
- [4] Q. L. de Chermont, C. Chanéac, J. Seguin, et al., "Nanoprobes with near-infrared persistent luminescence for in vivo imaging," *Proceedings of the National Academy of Sciences of the United States of America*, vol. 104, pp. 9266-9277, 2007.
- [5] T. Aitasalo, A. Hietikko, D. Hreniak, et al., "Structure and luminescence of $\text{BaMg}_2\text{Si}_2\text{O}_7:\text{Eu}^{2+},\text{Mn}^{2+}(\text{R}^{3+})$," to appear in *Journal of Alloys and Compounds*.
- [6] X.-J. Wang, D. Jia, and W. M. Yen, " Mn^{2+} activated green, yellow, and red long persistent phosphors," *Journal of Luminescence*, vol. 102-103, pp. 34-37, 2003.
- [7] S. G. Grubb, K. W. Bennett, R. S. Cannon, and W. F. Humer, "CW room-temperature blue up-conversion fibre laser," *Electronics Letters*, vol. 28, no. 13, pp. 1243-1244, 1992.
- [8] E. Downing, L. Hesselink, J. Ralston, and R. Macfarlane, "A three-color, solidstate, three-dimensional display," *Science*, vol. 273, no. 5279, pp. 1185-1189, 1996.
- [9] R. Gutmann, B. Ahlers, F. Kappe, R. Paugstadt, and A. Franz-Burgholz, US Patent no. 6,234,537, 2001.
- [10] E. Soini, N. J. Meltola, A. E. Soini, J. Soukka, J. T. Soini, and P. E. Hänninen, "Two photon fluorescence excitation in detection of biomolecules," *Biochemical Society Transactions*, vol. 28, pp. 70-74, 2000.
- [11] T. Soukka, K. Kuningas, T. Rantanen, V. Haaslahti, and T. Lövgren, "Photochemical characterization of up-converting inorganic lanthanide phosphors as potential labels," *Journal of Fluorescence*, vol. 15, no. 4, pp. 513-528, 2005.
- [12] A. Patra, C. S. Friend, R. Kapoor, and P. N. Prasad, "Up-conversion in $\text{Er}^{3+}:\text{ZrO}_2$ nanocrystals," *Journal of Physical Chemistry B*, vol. 106, no. 8, pp. 1909-1912, 2002.
- [13] A. Patra, C. S. Friend, R. Kapoor, and P. N. Prasad, "Effect of crystal nature on up-conversion luminescence in $\text{Er}^{3+}:\text{ZrO}_2$ nanocrystals," *Applied Physics Letters*, vol. 83, no. 2, pp. 284-286, 2003.
- [14] F. Vetrone, J.-C. Boyer, J. A. Capobianco, A. Speghini, and M. Bettinelli, "Significance of Yb^{3+} concentration on the up-conversion mechanisms in codoped $\text{Y}_2\text{O}_3:\text{Er}^{3+},\text{Yb}^{3+}$ nanocrystals," *Journal of Applied Physics*, vol. 96, no. 1, pp. 661-667, 2004.
- [15] L. A. Díaz-Torres, E. De la Rosa-Cruz, P. Salas, and C. Angeles-Chavez, "Concentration enhanced red up-conversion in nanocrystalline $\text{ZrO}_2:\text{Er}$ under IR excitation," *Journal of Physics D*, vol. 37, no. 18, pp. 2489-2495, 2004.
- [16] H. P. Klug and L. E. Alexander, *X-Ray Powder Diffraction Procedures*, Wiley, New York, NY, USA, 1959.
- [17] M. Karppinen, P. Kyläkoski, L. Niinistö, and C. Rodellas, "Thermal decomposition as a preparative route to anhydrous rare earth nitrates," *Journal of Thermal Analysis*, vol. 35, no. 2, pp. 347-353, 1989.
- [18] J. Hölsä and T. Turkki, "Preparation, thermal stability and luminescence properties of selected rare earth oxycarbonates," *Thermochimica Acta*, vol. 190, pp. 335-343, 1991.
- [19] PCPDFWIN v. 1.30, "Powder diffraction file," International Centre for Diffraction Data, entries 27-0997 (cubic ZrO_2) and 37-1484 (monoclinic ZrO_2), 1997.
- [20] Y. Mita, "Infrared up-conversion phosphors," in *Phosphor Handbook*, S. Shionoya and W. M. Yen, Eds., pp. 643-650, CRC Press, Boca Raton, Fla, USA, 1999.
- [21] F. Auzel, "Up-conversion in rare-earth-doped systems: past, present and future," in *XI Feofilov Symposium on Spectroscopy*

- of Crystals Activated by Rare-Earth and Transition Metal Ions*, vol. 4766 of *Proceedings of SPIE*, pp. 179–190, Kazan, Russia, September 2001.
- [22] F. Auzel, “Up-conversion and anti-Stokes processes with f and d ions in solids,” *Chemical Reviews*, vol. 104, no. 1, pp. 139–173, 2004.
- [23] J. Dexpert-Ghys, M. Faucher, and P. Caro, “Site selective spectroscopy and structural analysis of yttria-doped zirconia,” *Journal of Solid State Chemistry*, vol. 54, no. 2, pp. 179–192, 1984.
- [24] M. H. Tuilier, J. Dexpert-Ghys, H. Dexpert, and P. Lagarde, “X-ray absorption study of the ZrO_2 - Y_2O_3 system,” *Journal of Solid State Chemistry*, vol. 69, no. 1, pp. 153–161, 1987.
- [25] I. Hyppänen, J. Hölsä, J. Kankare, M. Lastusaari, and L. Pihlgren, Unpublished results.
- [26] M. Campbell and C. D. Flint, “Back transfer in the $^4S_{3/2}$ state of $Cs_2NaEr_xY_{1-x}Cl_6$ extension of the shell model,” *Spectrochimica Acta A*, vol. 54, no. 11, pp. 1583–1591, 1998.
- [27] F. Vetrone, J.-C. Boyer, J. A. Capobianco, A. Speghini, and M. Bettinelli, “Concentration-dependent near-infrared to visible up-conversion in nanocrystalline and bulk $Y_2O_3:Er^{3+}$,” *Chemistry of Materials*, vol. 15, no. 14, pp. 2737–2743, 2003.
- [28] M. Forcales, T. Gregorkiewicz, I. V. Bradley, and J.-P. R. Wells, “Afterglow effect in photoluminescence of Si:Er,” *Physical Review B*, vol. 65, no. 19, Article ID 195208, 8 pages, 2002.
- [29] J. W. Zhang, Y.-L. Liu, and S.-Q. Man, “Afterglow phenomenon in erbium and titanium codoped Gd_2O_3 phosphors,” *Journal of Luminescence*, vol. 117, no. 2, pp. 141–146, 2006.
- [30] N. Guerassimova, N. Garnier, C. Dujardin, A. G. Petrosyan, and C. Pédrini, “X-ray-excited charge transfer luminescence in YAG:Yb and YbAG,” *Journal of Luminescence*, vol. 94–95, pp. 11–14, 2001.
- [31] N. Guerassimova, N. Garnier, C. Dujardin, A. G. Petrosyan, and C. Pédrini, “X-ray excited charge transfer luminescence of ytterbium-containing aluminium garnets,” *Chemical Physics Letters*, vol. 339, no. 3–4, pp. 197–202, 2001.
- [32] T. Aitasalo, J. Hölsä, H. Jungner, M. Lastusaari, and J. Niitykoski, “Thermoluminescence study of persistent luminescence materials: Eu^{2+} - and R^{3+} -doped calcium aluminates, $CaAl_2O_4:Eu^{2+},R^{3+}$,” *Journal of Physical Chemistry B*, vol. 110, no. 10, pp. 4589–4598, 2006.
- [33] S. Schweizer, “Physics and current understanding of X-ray storage phosphors,” *Physica Status Solidi (a)*, vol. 187, no. 2, pp. 335–393, 2001.

Research Article

Femtosecond Transient Absorption Studies in Cadmium Selenide Nanocrystal Thin Films Prepared by Chemical Bath Deposition Method

M. C. Rath, J. A. Mondal, D. K. Palit, T. Mukherjee, and H. N. Ghosh

Radiation and Photochemistry Division, Bhabha Atomic Research Centre, Trombay, 400085 Mumbai, India

Received 30 March 2007; Revised 30 November 2007; Accepted 14 December 2007

Recommended by Tran Kim Anh

Dynamics of photo-excited carrier relaxation processes in cadmium selenide nanocrystal thin films prepared by chemical bath deposition method have been studied by nondegenerate femtosecond transient pump-probe spectroscopy. The carriers were generated by exciting at 400 nm laser light and monitored by several other wavelengths. The induced absorption followed by a fast bleach recovery observed near and above the bandgap indicates that the photo-excited carriers (electrons) are first trapped by the available traps and then the trapped electrons absorb the probe light to show a delayed absorption process. The transient decay kinetics was found to be multiexponential in nature. The short time constant, <1 picosecond, was attributed to the trapping of electrons by the surface and/or deep traps and the long time constant, ≥ 20 picoseconds, was due to the recombination of the trapped carriers. A very little difference in the relaxation processes was observed in the samples prepared at bath temperatures from 25°C to 60°C .

Copyright © 2007 M. C. Rath et al. This is an open access article distributed under the Creative Commons Attribution License, which permits unrestricted use, distribution, and reproduction in any medium, provided the original work is properly cited.

1. INTRODUCTION

Cadmium selenide (CdSe) nanocrystals (NCs) are important materials for optoelectronics, solar cells, and several biological applications [1–5]. Their optical tunability and stability make them ideal candidate for the future optoelectronics devices such as all optical switches and photovoltaics [6–9]. CdSe NCs are often grown over different substrates in the form of thin films. Several methods are employed for growing these thin films such as chemical deposition (CD) [10–13], electrochemical deposition (ECD) [14], photochemical deposition (PCD) [15], chemical vapour deposition (CVD) [16, 17], and molecular beam epitaxy (MBE) [9] methods. Apart from the form of thin films, nanoparticles forms are also prepared and studied in depth [18–20]. The chemical deposition (CD) is the easiest, the cheapest, and the most convenient method, which can produce such materials in a large scale. By changing the deposition parameters, such as concentrations of the individual reagents, bath temperature, and the duration of the deposition time, the NC size and the film thickness can be controlled.

The study of their optical properties is an essential element in the development of above-mentioned devices. Photo-excited carrier relaxation dynamics in these materials have been reported by a number of groups in the recent years. Maly et al. have studied the effect of surface states on the carrier relaxation dynamics in the CdSe NC films in a picosecond time-scale resolution [21]. Simurda et al. have reported the effect of surface passivation by ammonia in the carrier relaxation dynamics in the CdSe NC thin films [22]. Ai et al. have studied charge carrier dynamics in CdSe NC films using a femtosecond degenerate pump-probe technique [23]. Several other groups have reported the carrier dynamics in CdSe quantum structures in various conditions [24–29]. However, the carrier relaxation dynamics in the CdSe NC films prepared by the CD method are still to be investigated in a thoroughly manner. In this study, we report the carrier relaxation dynamics in CdSe NC films prepared by the CD method at different temperatures by femtosecond transient nonresonant nondegenerate pump-probe spectroscopy. We probed the carrier relaxation processes at various probe wavelengths by exciting at photon energy of 3.1 eV (400 nm).

2. EXPERIMENTAL

2.1. Sample preparation

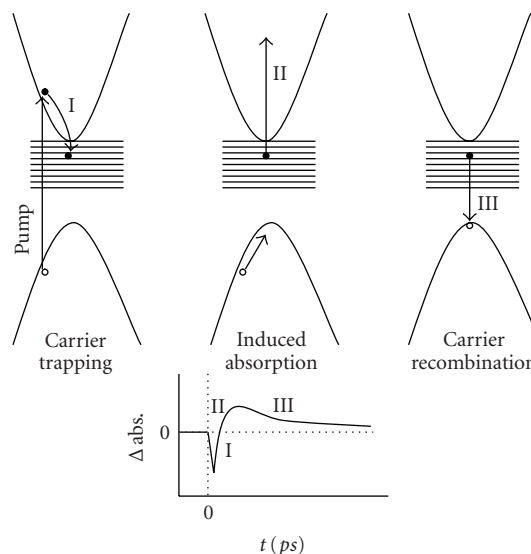
CdSe NC films were grown on clean glass substrates by the chemical deposition (CD) method [10–13]. Briefly, 10 mL 0.5 mol dm^{-3} CdSO_4 solution was taken in a 40 mL beaker. Ammonia solution was added slowly with a constant stirring until the solution became clearly transparent. A freshly prepared 10 mL Na_2SeSO_3 solution was added slowly to it. Clean glass slides were inserted into the beaker and inclined at about 20° angles to its wall. The bath temperature was kept at four different temperatures: 25°C , 40°C , 50°C , and 60°C . The deposition was carried out for 30 minutes to 3 hours depending on the bath temperatures. One side of the slide was cleaned by a cotton plug dipped in a dilute HCl. The films were air-dried and stored for further study. The orange-coloured as-grown films were characterized by XRD, SEM, EDAX, and optical absorption spectroscopy. The samples were characterized by atomic force microscope (AFM) at ambient conditions.

2.2. Femtosecond transient absorption spectrometer

Ultrafast carrier relaxation dynamics study was performed by using a multipass amplified femtosecond Ti:sapphire laser system from Avesta, Russia (1 kHz repetition rate at 800 nm, 50 femtoseconds, $800 \mu\text{J}/\text{pulse}$). The details of the setup are described elsewhere [30]. Typically, the 800 nm output pulses from the multipass amplifier are split into two parts to generate pump and probe pulses. One part, with $200 \mu\text{J}/\text{pulse}$, is frequency doubled in a BBO crystal to generate pump pulse at 400 nm. The other part is focused onto a 1.5 mm thick sapphire window to generate a white-light continuum for the probe pulses (470 nm to 1000 nm). The pump and probe energies at the sample position were $18 \mu\text{J}/\text{pulse}$ and $200 \text{ nJ}/\text{pulse}$, respectively. The angle between the pump and probe pulses is about 8° . The pump pulses are set at magic angle (54.7°) with respect to the probe pulses, which are horizontally polarised. The pump and probe spot sizes at the sample position were about $400 \mu\text{m}$ and $200 \mu\text{m}$, respectively. The pump-probe setup works in transmission mode. The wavelength of the white light (probe pulses) was tuned by the interference filter just before the photodiodes. The signal collected by the photodiodes is fed to the boxcar, and the data acquisition is done by using the Labview programme in a picosecond. The typical noise in the measured absorbance change is less than about 0.4%.

3. RESULTS AND DISCUSSION

The optical absorption spectra (Figure 1) of the films exhibited distinct excitonic absorption peaks (E_1) at around 540 nm (2.29 eV), 550 nm (2.25 eV), 562 nm (2.21 eV), and 574 nm (2.16 eV) for the 25°C , 40°C , 50°C , and 60°C samples, respectively. The optical absorption spectra extend beyond 700 nm. The extended absorption beyond 700 nm that arises in the chemical method of preparation can be attributed to the surface states. The absorption peak corresponds to the lowest allowed transition $1S_e-1S_h$ [27, 31–33].



SCHEME 1: Schematic representation of the photo-excited carrier relaxation processes in the CdSe NC thin films prepared by the CD method. I: carrier trapping process; II: induced absorption process; III: recombination of the trapped carriers. All the three processes occur consecutively and the resultant transient absorption signal for a bandgap probe would look like a model picture as shown at the bottom.

There is a systematic shift in the excitonic absorption peak towards the higher-wavelength side with the increase in the reaction of bath temperature. This indicates that there is an increase in the grain size of the nanocrystals with temperature. The room temperature bandgap of the bulk CdSe is 1.74 eV. The NC grain size was determined from the energy of quantum confinement (i.e., $\Delta E = E_1 - E_g$) using modified Brus equation, which ranges from 1.9 nm to 2.5 nm for the 25°C to 60°C samples, respectively. This indicates that the NC consists of quantum size particles (de Broglie wavelength of the charge carriers = 4.8 nm at room temperature).

The grain sizes of the NC films were also calculated from the XRD data using Scherrer's formula and listed in Table 1. The slight deviation in the grain size obtained from two different results could be due to a broad nature of the absorption spectra. The AFM picture of one of the CdSe samples prepared at 40°C is shown in Figure 2. The picture indicates a nice uniform growth of the nanocrystals of CdSe over the glass substrates. The formation of CdSe nanocrystals prepared by the chemical bath deposition method has been reported by Kale et al. [34] where they have observed a direct evidence of the formation of CdSe nanocrystals from the AFM and SEM data. The thickness of the samples determined from the weight difference method was found to be between 300 and 500 nm. The thickness of the samples as determined from the AFM measurements fairly matches with the previous ones.

The emission from these samples was too weak to be detected by normal steady-state fluorescence spectrometer at room temperature; however, a very weak emission could be observed only at higher wavelengths $>600 \text{ nm}$ for all

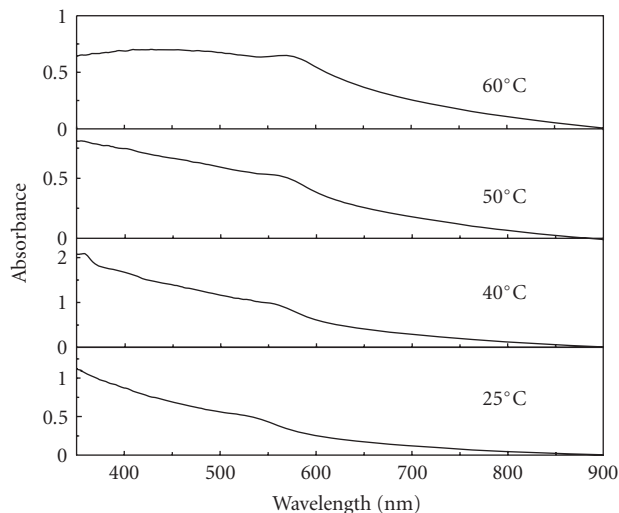


FIGURE 1: The room temperature optical absorption spectra of four different CdSe NC thin films.

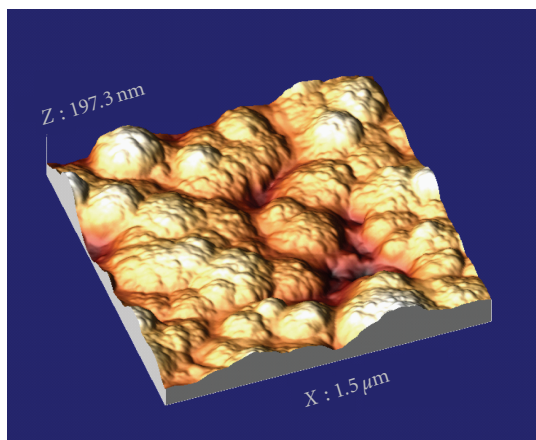


FIGURE 2: A 3-dimensional AFM picture of CdSe NC thin film sample prepared at 40°C.

the samples. This could be due to the predominance of a nonradiative deactivation of photo-excited carriers via the trap states available in these samples. The pump-probe experiments have been carried out at room temperature. The samples were excited (pumped) by a 400 nm (3.1 eV) light and probed at various other wavelengths, such as 470 nm (2.64 eV), 610 nm (2.03 eV), 710 nm (1.75 eV), and 900 nm (1.38 eV). The 470 nm probe light corresponds to an energy higher than the $1S_e-1S_h$ transition level, 610 nm corresponds very close to the $1S_e-1S_h$ transition, 710 nm corresponds to just below the $1S_e-1S_h$ transition, and 900 nm corresponds to very less than the bandgap transition in these materials.

Time-resolved transient absorption spectra of a CdSe NC film grown at 40°C obtained from the pump-probe spectroscopy are shown in Figure 3. A bleach signal was observed in this sample from 470 nm to about 800 nm with a peak at

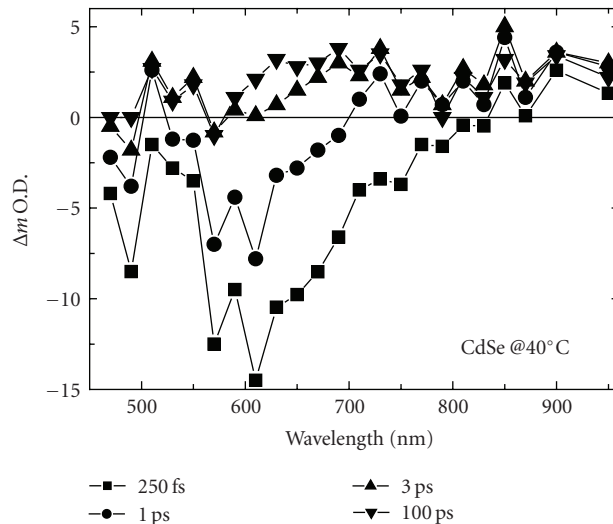


FIGURE 3: The time-resolved transient absorption spectra of CdSe NC thin film prepared at 40°C.

around 610 nm. This recovers within a short time about ≤ 3 picoseconds with the formation of an induced absorption in the entire visible range. One set of the pump-probe kinetic profiles obtained at different probe wavelengths for the sample grown at 25°C is shown in Figure 4. The kinetic profiles for all the four samples monitored at two probe wavelengths 610 nm and 900 nm are shown in Figures 5 and 6, respectively. The kinetic profiles for the other three samples grown at 40°C, 50°C, and 60°C can be found in the supporting information. The inset in the figures shows in a short-time scale. The slight deviations in the kinetic profiles could be related to their transient absorption spectral patterns. There was no change in the kinetic profiles with the reduction in the pump energy from $18 \mu\text{J}/\text{pulse}$ to $8 \mu\text{J}/\text{pulse}$ except that there was a reduction in the signal intensity. The kinetic profiles at various probe wavelengths were fitted with multiexponential fitting parameters by using the Labview fitting programme, and the best-fit results are listed in Table 1.

In this case, the pump pulses photo-excite the valence band (VB) electrons to the conduction band (CB) creating a hot electron density in the CB and holes in the VB. The probe pulses monitor these photo-excited electrons in the CB by a band-to-band absorption process. However, it is true that on photo-excitation, charge carriers are generated which is due to hole in the valence band and electron in the conduction band. So it is quite obvious to think that both the electron and the hole can have transient absorption in the visible region. However, the charge carriers can have different cross-section of transient absorption in different probing regions. Burda et al. [35] carried out ultrafast transient spectroscopy on CdSe nanoparticles monitoring at visible, near IR, and mid-IR regions separately. They have shown clearly that cross-section of electron is more in the visible and mid-IR regions, and on the other hand, the hole has more cross-section in the near-IR region. They have observed that excited dynamics in the visible and mid-IR regions are solely

TABLE 1: Photo-excited electron decays time constants in different CdSe NC thin films probing at different wavelengths. (br: bleach recovery; ia: induced absorption; iad: induced absorption decay; af: absorption formation; ad: absorption decay. The bracket values indicate the relative percentage calculated from their pre-exponential factor values obtained from the best-fit data. The negative percentage values in the bracket indicate the time constants for the decay processes, and the total relative percentage values for a given set of data are normalized to 100.)

Bath temp. ($\pm 2^\circ\text{C}$)	Time constants in picoseconds (relative percentage)				Grain size, a (nm)
	470 nm	610 nm	710 nm	900 nm	
25	0.5 (73%) br	0.65 af	0.25 af	1.5 (62%) ad	2.9 ± 0.3
	2.0 (35%) ia	10 (52%) ad	10 (47%) ad	20 (20%) ad	
	>100 (-8%) iad	>100 (48%) ad	>100 (53%) ad	>100 (18%) ad	
40	0.3 (85%) br	0.3 (77%) br	0.3 (94%) br	2 af	3.2 ± 0.3
	3.5 (10%) br	2.5 (33%) ia	3 (77%) ia	20 (73%) ad	
	>100 (5%) br	>100 (-10%) iad	6 (-51%) iad	>100 (27%) ad	
50	0.6 (112%) br	0.65 (88%) br	0.23 (98%) br	2 af	3.6 ± 0.4
	—	3 (28%) ia	2.5 (16%) ia	5 (14%) ad	
	3 (-13%) iad	>100 (-16%) iad	20 (-10%) iad	50 (5%) ad	
60	0.5 (103%) br	0.35 (140%) br	—	—	3.8 ± 0.4
	6 (33%) ia	1 (8%) ia	—	—	
	10 (-30%) iad	20 (-30%) iad	3 (44%) ad	1 (77%) ad	
	>100 (-6%) iad	>100 (-18%) iad	>100 (56%) ad	20 (23%) ad	

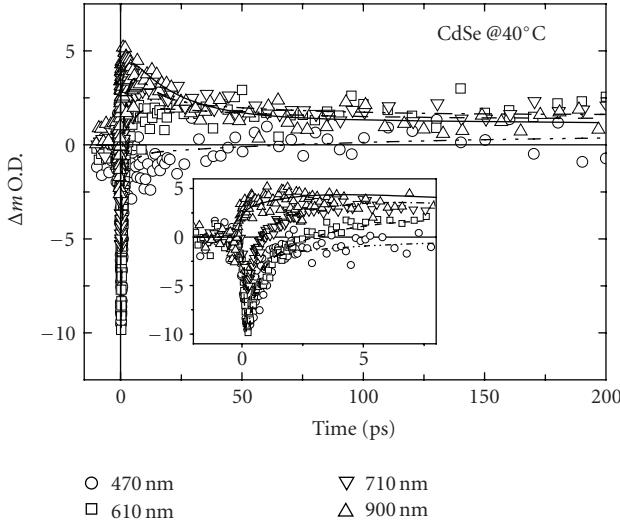


FIGURE 4: Kinetic profiles obtained at different probe wavelengths in the pump-probe experiment for the CdSe NC thin film samples prepared at 40°C . Inset: kinetic profiles at short-time scales. The solid lines represent the best-fit curves.

due to electron in the conduction band; on the other hand, transient absorption in the near-IR region is due to the hole in the valence band. In the present investigation, we are monitoring the charge carriers in the visible region (470–950 nm) which are attributing to the relaxation dynamics due to electron. However, there might be a very little contribution due to the hole absorption in the visible region which is negligible. Now, the kinetic bleach signals obtained at the probe wavelengths other than 900 nm are found to be associated

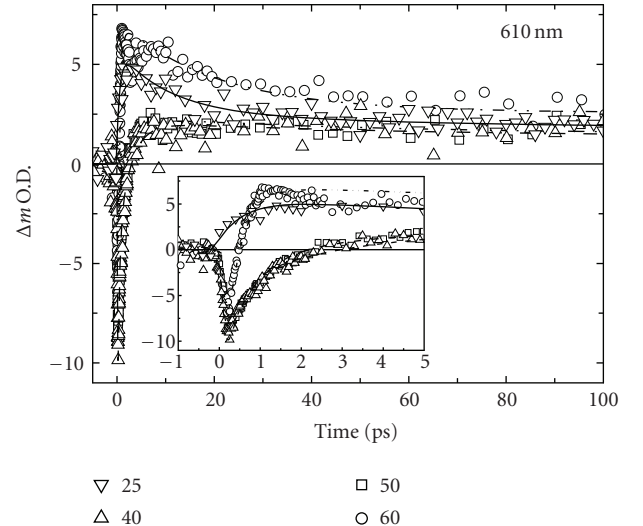


FIGURE 5: Kinetic profiles obtained at 610 nm in the pump-probe experiment for the CdSe NC thin film samples prepared at 25°C , 40°C , 50°C , and 60°C . Inset: kinetic profiles at short-time scales. The solid lines represent the best-fit curves.

with the formation of an induced absorption process, which decays at a long-time scale. The pulse-width-limited rise time in the bleach signal indicates that the carriers relax down to a lower-energy level of the conduction band during this time period (i.e., about 100 femtoseconds). The overall excitation and de-excitation pathways for these samples are represented in Scheme 1. The pump-probe experiments monitor the photo-excited electrons in the CB, as the bandgap absorption is mainly dependent on the CB electron density.

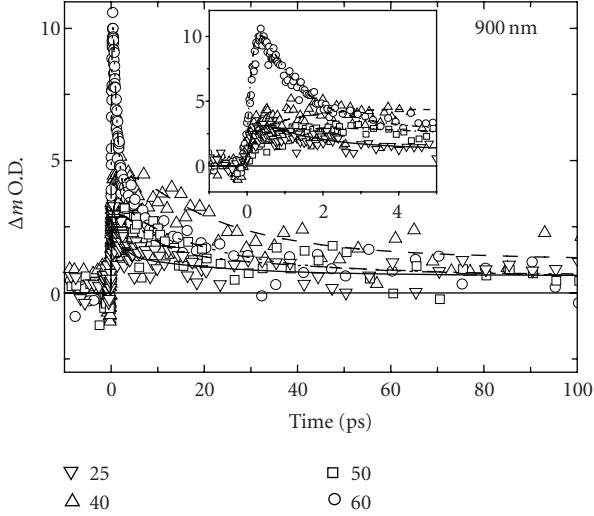


FIGURE 6: Kinetic profiles obtained at 900 nm in the pump-probe experiment for the CdSe NC thin film samples prepared at 25°C, 40°C, 50°C, and 60°C. Inset: kinetic profiles at short-time scales. The solid lines represent the best-fit curves.

The pump-probe kinetic profiles obtained at the bandgap probe wavelengths can be modeled to an empirical equation as written below:

$$-d\alpha/dt = k_1n - k_2(n + m) + k_3n, \quad (1)$$

where k_1 , k_2 , and k_3 are the rate constants for the three processes such as carrier trapping, induced absorption, and carrier recombination, as indicated in Scheme 1. In (1), n is the number density of the photo-excited electrons at the conduction band (CB), m is the inherent free-electron density available at the trap centers, and α is the overall probe absorption in the materials. A model kinetic profile is shown the bottom of Scheme 1. The initial bleach signal is due to the band filling effect for the bandgap probe wavelengths. A bleach signal is not expected for the probe wavelength 900 nm. The time constants for the bleach recovery and the formation of an induced absorption process are found to be less than 1 picosecond and slightly higher than 2 picoseconds, respectively. The fast time constant (<1 picosecond) is due to the trapping of the electrons at the surface traps and/or deep traps. The second component (>2 picoseconds) is due to the absorption of the trapped electrons at the trap centers as represented in Scheme 1. The relative percentages of the observed time constants were calculated from the pre-exponential factors, and the overall percentage was fixed at 100. The relative percentage of the first time constant is found to be always higher than that of the second one. Therefore, the trapping of the electrons and the formation of the absorbing trapped electrons for the further absorption to a higher energy state in the CB are very much comprehensive to each other. The long decay time constants obtained at these probe wavelengths indicate a slow recombination process of the trapped carriers. Similar slow recombination dynamics has been observed

by Benjamin et al. [36] in GaAs semiconductor materials, which have attributed to the recombination dynamics due to midgap trap states. The amplitude of the bleach signal was higher than that of the induced absorption, and the residual part of the absorption decay signal is very less as compared to the previous two. Therefore, the samples could be classified as one of the fast optical response materials. There was a slight difference in the time constants obtained in the four different samples. However, the observed time constants follow a systematic pattern following the model given in Scheme 1. The carrier-relaxation pattern in the 40°C and 50°C samples seems to have a similar trend, whereas the 25°C and 60°C samples found to have a slightly different pattern as compared to the previous two samples.

The results obtained at 900 nm were slightly different from the above. The probe pulse monitors the initially freely available electrons presented in the deep traps and then the trapped electrons populated there. This is because the CdSe nanostructured materials prepared by the CD method have a lot of defect states. As the energy of this probe photon is very less than that of the pump photons as well as that of the excitonic absorption peak position, so there was no bleach signal for this probe wavelength. The decay time constants obtained from kinetic profiles at this probe wavelength indicate the recombination time for the electrons and the holes at the trap centers as well as at the two band structures. The decay time constants match well with the absorption decay time constants obtained for other probe wavelengths. Similarly, there was a slight difference in the time constants obtained in the four different samples. This could be due to the fact that the change in the grain size of around 1 nm within the quantum confinement regime does not make any significant deviations in the photo-excited carrier relaxation processes among these four sets of samples. Hence, it is predicted that these kinds of materials could be useful for the devices based on a fast optical response.

4. CONCLUSION

The photo-excited carrier relaxation processes in cadmium selenide nanocrystal thin films prepared by chemical deposition method have been studied by nondegenerate femtosecond pump-probe spectroscopic method. The induced absorption followed by a fast bleach recovery within a less than 3-picosecond time scale indicates that the photo-excited electrons are first trapped by the trap sites and then the trapped electrons absorb the probe light to a higher-energy level in the conduction band which exhibits such a delayed absorption process. The short time constant, <1 picosecond, was attributed to the trapping of electrons by the surface and/or deep traps, and the long-time constant, >100 picoseconds, was due to the recombination of the trapped carriers. The amplitude of the bleach signal is very high as compared to that of the residual part of the induced absorption decay, which indicates that the carrier trapping process is a major phenomenon in these materials. The samples obtained at 40°C and 50°C were found to have similar carrier relaxation pattern which is different from the other two samples.

ACKNOWLEDGMENTS

The authors would like to acknowledge Ms. Elena Pilina, Nanotec Electronica, Madrid, Spain, for her help in the AFM measurements. They also like to acknowledge Dr. S. K. Sarkar, Head of Radiation and Photochemistry Division for encouragement.

REFERENCES

- [1] L. Han, D. Qin, X. Jiang, et al., "Synthesis of high quality zinc-blende CdSe nanocrystals and their application in hybrid solar cells," *Nanotechnology*, vol. 17, no. 18, pp. 4736–4742, 2006.
- [2] R. E. Bailey, A. M. Smith, and S. Nie, "Quantum dots in biology and medicine," *Physica E*, vol. 25, no. 1, pp. 1–12, 2004.
- [3] O. Niitsoo, S. K. Sarkar, C. Pejoux, S. Rühle, D. Cahen, and G. Hodes, "Chemical bath deposited CdS/CdSe-sensitized porous TiO₂ solar cells," *Journal of Photochemistry and Photobiology A: Chemistry*, vol. 181, no. 2-3, pp. 306–313, 2006.
- [4] A. Nozik, "Quantum dot solar cells," *Physica E*, vol. 14, no. 1-2, pp. 115–120, 2002.
- [5] I. Robel, V. Subramanian, M. Kuno, and P. V. Kamat, "Quantum dot solar cells. Harvesting light energy with CdSe nanocrystals molecularly linked to mesoscopic TiO₂ films," *Journal of the American Chemical Society*, vol. 128, no. 7, pp. 2385–2393, 2006.
- [6] K.-C. Chu, W.-S. Su, and Y.-F. Chen, "Liquid crystals driven by CdSe semiconductor," *Journal of Applied Physics*, vol. 100, Article ID 024516, 4 pages, 2006.
- [7] S. K. J. Al-Ani, H. H. Mohammed, and E. M. N. Al-Fwade, "The optoelectronic properties of CdSe: Cu photoconductive detector," *Renewable Energy*, vol. 25, no. 4, pp. 585–590, 2002.
- [8] Y. Araki, K. Ohkuno, T. Furukawa, and J. Saraie, "Green light emitting diodes with CdSe quantum dots," *Journal of Crystal Growth*, vol. 301-302, pp. 809–811, 2007.
- [9] J. Qiu, H. Cheng, J. M. de Puydt, and M. A. Haase, "Recent developments in the MBE growth of wide bandgap II-VI semiconductors for laser diodes and LEDs," *Journal of Crystal Growth*, vol. 127, no. 1–4, pp. 279–286, 1993.
- [10] S. S. Kale and C. D. Lokhande, "Thickness-dependent properties of chemically deposited CdSe thin films," *Materials Chemistry and Physics*, vol. 62, no. 2, pp. 103–108, 2000.
- [11] R. B. Kale and C. D. Lokhande, "Systematic study on structural phase behavior of CdSe thin films," *Journal of Physical Chemistry B*, vol. 109, no. 43, pp. 20288–20294, 2005.
- [12] C. D. Lokhande, E.-H. Lee, K.-D. Jung, and O.-S. Joo, "Ammonia-free chemical bath method for deposition of microcrystalline cadmium selenide films," *Materials Chemistry and Physics*, vol. 91, no. 1, pp. 200–204, 2005.
- [13] S. Gorer and G. Hodes, "Quantum size effects in the study of chemical solution deposition mechanisms of semiconductor films," *Journal of Physical Chemistry*, vol. 98, no. 20, pp. 5338–5346, 1994.
- [14] K. K. Mishra and K. Rajeshwar, "A re-examination of the mechanisms of electrodeposition of CdX and ZnX (X = Se, Te) semiconductors by the cyclic photovoltammetric technique," *Journal of Electroanalytical Chemistry*, vol. 273, no. 1-2, pp. 169–182, 1989.
- [15] M. Ichimura, K. Takeuchi, A. Nakamura, and E. Arai, "Photochemical deposition of Se and CdSe films from aqueous solutions," *Thin Solid Films*, vol. 384, no. 2, pp. 157–159, 2001.
- [16] Y. Yang, D. Z. Shan, J. Y. Zhang, et al., "The formation mechanism of self-assembled CdSe quantum dots," *Journal of Crystal Growth*, vol. 233, no. 4, pp. 785–790, 2001.
- [17] D. Noda, T. Aoki, Y. Nakanishi, and Y. Hatanaka, "Epitaxial growth of CdSeTe films by remote plasma enhanced metal organic chemical vapor deposition," *Vacuum*, vol. 59, no. 2-3, pp. 701–707, 2000.
- [18] L. Qu and X. Peng, "Control of photoluminescence properties of CdSe nanocrystals in growth," *Journal of the American Chemical Society*, vol. 124, no. 9, pp. 2049–2055, 2002.
- [19] Z. A. Peng and X. Peng, "Nearly monodisperse and shape-controlled CdSe nanocrystals via alternative routes: nucleation and growth," *Journal of the American Chemical Society*, vol. 124, no. 13, pp. 3343–3353, 2002.
- [20] L. Manna, E. C. Scher, and A. P. Alivisatos, "Synthesis of soluble and processable rod-, arrow-, teardrop-, and tetrapod-shaped CdSe nanocrystals," *Journal of the American Chemical Society*, vol. 122, no. 51, pp. 12700–12706, 2000.
- [21] P. Maly, J. Kudma, F. Trojaneck, et al., "Dominant role of surface states in photoexcited carrier dynamics in CdSe nanocrystalline films prepared by chemical deposition," *Applied Physics Letters*, vol. 77, no. 15, pp. 2352–2354, 2000.
- [22] M. Simurda, P. Nemecek, and J. Preclikova, "Ammonia effect on surface-mediated carrier dynamics in CdSe nanocrystals," *Thin Solid Films*, vol. 503, no. 1-2, pp. 64–68, 2006.
- [23] X. Ai, R. Jin, C. Ge, et al., "Femtosecond investigation of charge carrier dynamics in CdSe nanocluster films," *Journal of Chemical Physics*, vol. 106, no. 108, pp. 3387–3392, 1997.
- [24] Q. Darugar, C. Landes, S. Link, A. Schill, and M. A. El-Sayed, "Why is the thermalization of excited electrons in semiconductor nanoparticles so rapid? Studies on CdSe nanoparticles," *Chemical Physics Letters*, vol. 373, no. 3-4, pp. 284–291, 2003.
- [25] V. I. Klimov, A. A. Mikhailovsky, D. W. McBranch, C. A. Leatherdale, and M. B. Bawendi, "Mechanisms for intraband energy relaxation in semiconductor quantum dots: the role of electron-hole interactions," *Physical Review B*, vol. 61, no. 20, pp. R13349–R13352, 2000.
- [26] T. W. Roberti, N. J. Cherepy, and J. Z. Zhang, "Nature of the power-dependent ultrafast relaxation process of photoexcited charge carriers in II-VI semiconductor quantum dots: effects of particle size, surface, and electronic structure," *Journal of Physical Chemistry*, vol. 108, no. 5, pp. 2143–2151, 1998.
- [27] C. Burda and M. A. El-Sayed, "High-density femtosecond transient absorption spectroscopy of semiconductor nanoparticles. A tool to investigate surface quality," *Pure and Applied Chemistry*, vol. 72, no. 1-2, pp. 165–177, 2000.
- [28] H. Wang, C. M. Donega, A. Meijerink, and M. Glasbeek, "Ultrafast exciton dynamics in CdSe quantum dots studied from bleaching recovery and fluorescence transients," *Journal of Physical Chemistry*, vol. 110, no. 2, pp. 733–737, 2005.
- [29] C. Burda, S. Link, T. C. Green, and M. A. El-Sayed, "Electron shuttling across the interface of CdSe nanoparticles monitored by femtosecond laser spectroscopy," *Journal of Physical Chemistry*, vol. 103, no. 11, pp. 1783–1788, 1999.
- [30] G. Ramakrishna, A. K. Singh, D. K. Palit, and H. N. Ghosh, "Slow back electron transfer in surface-modified TiO₂ nanoparticles sensitized by alizarin," *Journal of Physical Chemistry B*, vol. 108, no. 5, pp. 1701–1707, 2004.
- [31] D. J. Norris and M. G. Bawendi, "Measurement and assignment of the size-dependent optical spectrum in CdSe quantum dots," *Physical Review B*, vol. 53, no. 24, pp. 16338–16346, 1996.

-
- [32] B. Alpers, I. Rubinstein, and G. Hodes, "Identification of surface states on individual CdSe quantum dots by room-temperature conductance spectroscopy," *Physical Review B*, vol. 63, no. 8, Article ID 081303, 4 pages, 2001.
- [33] S. Sapra and D. D. Sarma, "Evolution of the electronic structure with size in II-VI semiconductor nanocrystals," *Physical Review B*, vol. 69, Article ID 125304, 7 pages, 2004.
- [34] R. B. Kale, S. D. Sartale, B. K. Chougale, and C. D. Lokhande, "Growth and characterization of nanocrystalline CdSe thin films deposited by the successive ionic layer adsorption and reaction method," *Semiconductor Science and Technology*, vol. 19, pp. 980–986, 2004.
- [35] C. Burda, S. Link, M. B. Mohamed, and M. El-Sayed, "The pump power dependence of the femtosecond relaxation of CdSe nanoparticles observed in the spectral range from visible to infrared," *Journal of Chemical Physics*, vol. 116, no. 9, pp. 3828–3833, 2002.
- [36] S. D. Benjamin, H. S. Loka, A. Othonos, and P. W. E. Smith, "Ultrafast dynamics of nonlinear absorption in low-temperature-grown GaAs," *Applied Physics Letters*, vol. 68, no. 18, pp. 2544–2546, 1996.